



Fakultät für Medizin

Molekulare Kardiologie

I. Medizinische Klinik und Poliklinik

Klinikum rechts der Isar

Human iPSC-derived cardiomyocytes as platforms for cardiac disease modeling, therapeutic discovery and safety pharmacology

Zhifen Chen

Vollständiger Abdruck der von der Fakultät für Medizin der Technischen Universität München zur Erlangung des akademischen Grades eines

Doctor of Philosophy (Ph.D.)

genehmigten Dissertation.

Vorsitzender: Prof. Dr. Stefan Engelhardt

Betreuer: Prof. Dr. Karl-Ludwig Laugwitz

Prüfer der Dissertation:

1. Prof. Dr. Alessandra Moretti, Ph. D.
2. Prof. Dr. Adnan Kastrati
3. Prof. Dr. Thomas Gudermann

Die Dissertation wurde am 14.06.2016 bei der Fakultät für Medizin der Technischen Universität München eingereicht und durch die Fakultät für Medizin am 13.09.2016 angenommen.

Abstract

Human induced pluripotent stem cells (hiPSCs) represent an unlimited source for nearly all types of cell in human body. The generation of hiPSC-lines from patients affected by genetic disorders allows the production of patient-specific cell types affected by the disease-related genetic variants.

Differentiation of hiPSCs into cardiomyocytes (CMs) has been extensively investigated, and healthy as well as diseased hiPSC-derived cardiomyocytes (hiPSC-CMs) are increasingly used in cardiac disease modeling and drug evaluation. Dilated cardiomyopathy (DCM), the most common genetically-caused cardiomyopathy occurring in 1 in 3000 individuals, is characterized by ventricular dilatation, systolic dysfunction and progressive heart failure. Frameshift mutations in the *TTN* gene encoding the sarcomeric protein titin are a main cause for hereditary DCM. So far, there are no causal therapies available. In this work, we show the beneficial effects of reframing titin mRNA transcripts by antisense oligonucleotide (AON)-mediated exon skipping in a hiPSC-based DCM model carrying a previously described autosomal-dominant frameshift mutation causing a premature stop codon in titin exon 326. Correction of the *TTN* reading frame in patient-specific iPSC-CMs rescued defective myofibril assembly and stability and normalized the sarcomeric protein expression. Our results demonstrate that disruption of the titin reading frame can be restored in vitro in patient-specific hiPSC-CMs by exon skipping, suggesting AON-mediated antisense strategies as a potential therapy for inherited DCM.

Although hiPSC-CMs are intensively used in disease modelling and drug evaluation, they are typically a heterogeneous mix of ventricular-, atrial- and nodal-like cells based on action potential characteristics (APs) and gene expression profiles. This heterogeneity and the paucity of methods for high-throughput functional phenotyping hinder the full exploitation of their potential. Therefore, to develop a method for rapid, subtype-specific phenotyping of hiPSC-CMs with respect to AP morphology and single-cell arrhythmias, we used cardiac lineage-specific promoters to drive the expression of a voltage-sensitive fluorescent protein (VSFP-CR), enabling subtype-specific optical AP recordings. In a patient-specific hiPSC model of long-QT syndrome type 1 (LQT1), AP prolongation and frequent early afterdepolarizations were evident in mutant ventricular- and atrial-like, but not in nodal-like hiPSC-CMs compared to their isogenic controls, consistent with the expression pattern of the disease-causing gene. Furthermore, we demonstrate the feasibility of sequentially probing a cell over several days to investigate genetic rescue of the disease phenotype and to discern CM subtype-specific drug effects. Taken

together, by combining a genetically-encoded membrane voltage sensor with promoters that drive expression in the major subtypes of hiPSC-CMs, we developed a convenient system for disease modelling and drug evaluation in the relevant cell type that has the potential to advance the emerging utility of hiPSCs in cardiovascular medicine.

In addition, cardiac toxicity is a major problem in drug development, which has resulted in numerous preventable patient deaths and, consequently, withdrawal of drugs with adverse cardiac side effects from the market. Occurrence of adverse cardiac drug effects is more common in patients with pre-existing cardiac diseases than in the normal population. Here, we used both healthy control and LQT1 patient hiPSC-CMs to investigate effects of the QT interval-prolonging drug cisapride. Using the optical AP recording system, we found that cisapride increased AP duration and promoted early afterdepolarizations (EADs) in all cell lines. The promotion of EADs was most pronounced in the LQT hiPSCs, indicating that healthy and diseased subjects have different susceptibilities to cardiotoxic drugs and thereby the use of disease-specific hiPSC-CMs may predict adverse drug reactions more accurately than the standard hERG assay or methods using healthy control hPSC-CMs.

Zusammenfassung

Humane induzierte pluripotente Stammzellen (hiPS-Zellen) können als unlimitierte Quelle nahezu aller Zelltypen des menschlichen Körpers dienen. Die Generierung von hiPS-Zell-Linien von Patienten, die an genetisch bedingten Erkrankungen leiden, erlaubt die Produktion Patienten-spezifischer Zelltypen, die die Krankheits-assoziierten genetischen Varianten tragen.

Die Differenzierung von hiPS-Zellen zu Kardiomyozyten ist ausgiebig erforscht worden, und sowohl gesunde als auch erkrankte von hiPS-Zellen abgeleitete Kardiomyozyten (hiPSC-CM) werden in zunehmendem Maße in der Modellierung kardialer Erkrankungen sowie in der Evaluation von Medikamenten verwendet. Die Dilatative Kardiomyopathie (DCM), die häufigste genetisch verursachte Kardiomyopathie mit einer Prävalenz von 1:3000, zeichnet sich durch eine Dilatation der Herzhöhlen, eine systolische Dysfunktion und eine progrediente Herzinsuffizienz aus. Leserahmenverschiebende Mutationen des *TTN*-Gens, das das sarkomerische Protein Titin kodiert, sind eine wesentliche Ursache der hereditären DCM. Bislang gibt es keine kausalen Therapieoptionen. In dieser Arbeit zeigen wir günstige Effekte einer Wiederherstellung des Leserahmens der Titin-mRNA mittels durch Antisense-Oligonukleotide (AON) hervorgerufenen Exon-skippings in einem auf hiPS-Zellen basierenden DCM-Krankheitsmodell, hervorgerufen durch eine autosomal-dominante, den Leserahmen verschiebende und ein vorzeitiges Stop-Codon verursachende Mutation im Exon 326 des Titin-Gens. Eine Korrektur des *TTN*-Leserahmens in Patienten-spezifischen hiPSC-CM normalisierte den gestörten Aufbau der Myofibrillen und die Expression sarkomerischer Proteine. Unsere Ergebnisse zeigen, dass eine Verschiebung des Titin-Leserahmens in vitro in Patienten-spezifischen hiPS-CMs mittels Exon-skipping rückgängig gemacht werden kann. Somit könnten AON-vermittelte Antisense-Strategien eine mögliche Therapie der erblichen DCM darstellen.

Wenngleich hiPS-CM intensiv in der Modellierung von Krankheiten und in der Evaluation von Medikamenten genutzt werden, stellen sie sich typischerweise als eine heterogene Mischung von Kardiomyozyten dar, die anhand von Aktionspotential-Charakteristika und Genexpressionsmustern als atrial-, ventrikulär- und nodal-ähnliche Zellen klassifiziert werden können. Diese Heterogenität und der Mangel an Methoden für eine funktionelle Charakterisierung mit hohem Durchsatz sind Hinderungsgründe für eine volle Nutzung des Potentials dieser Zellen. Daher haben wir, um eine Methode zur raschen und subtyp-spezifischen phänotypischen Charakterisierung in Hinblick auf Aktionspotentialmorphologie und Arrhythmien auf Einzelzell-Ebene zu entwickeln, Linien-spezifische Promotoren verwendet, um

Zusammenfassung

die Expression eines spannungsabhängigen fluoreszierenden Proteins (*voltage-sensitive fluorescent protein*, VSFP-CR) in spezifischen Subtypen von hiPS-CMs zu erreichen und subtyp-spezifische optische Aktionspotential-Messungen zu ermöglichen.

In einem Patienten-spezifischen hiPS-Zell-Modell des Long-QT-Syndroms Typ 1 (LQT1) zeigten sich verlängerte Aktionspotentiale und häufige frühe Nachdepolarisationen (*early afterdepolarizations*, EADs) in die krankheitsverursachende Mutation tragenden atrial- und ventrikulär-ähnlichen, aber nicht in nodal-ähnlichen hiPS-Kardiomyozyten, in Übereinstimmung mit dem Expressionsmuster des krankheitsverursachenden Gens.

Darüber hinaus zeigten wir die Möglichkeit, eine Zelle über mehrere Tage sequentiell zu untersuchen, um eine genetische Strategie zur Heilung des Krankheitsphänotyps zu untersuchen und um Kardiomyozyten-Subtyp-spezifische Medikamenteneffekte nachzuweisen. Zusammenfassend haben wir durch die Kombination eines genetisch kodierten Membranpotential-Sensors mit Promotoren, die dessen Expression in den wesentlichen Subtypen von hiPS-Kardiomyozyten antreiben, ein komfortables System zur Modellierung von Krankheiten und zur Untersuchung von Medikamenten-Effekten in den relevanten Zelltypen entwickelt. Dieses System hat das Potential, die Anwendung von hiPS-Zellen in der kardiovaskulären Medizin voranzubringen.

Kardiale Toxizität ist ein wesentliches Problem in der Entwicklung neuer Medikamente und hat in der Vergangenheit zu zahlreichen vermeidbaren Todesfällen und, in Folge, zur Rücknahme von Pharmaka mit bedeutsamen kardiovaskulären Nebenwirkungen vom Markt geführt. Das Auftreten von kardiovaskulären Nebenwirkungen ist bei Patienten mit präexistenten kardialen Erkrankungen häufiger als in der Allgemeinbevölkerung. Hier haben wir hiPS-Kardiomyozyten sowohl von gesunden Kontrollprobanden als auch von einem LQT1-Patienten verwendet, um Effekte des QT-Intervall-verlängernden Medikaments Cisaprid zu untersuchen. Unter Verwendung des optischen Aktionspotential-Aufzeichnungssystems konnten wir zeigen, dass Cisaprid in allen Zelllinien die Aktionspotentialdauer verlängerte und EADs hervorrief. Die Induktion von EADs war in den LQT-hiPS-Zellen am ausgeprägtesten, was dafür spricht, dass gesunde und erkrankte Personen eine unterschiedliche Anfälligkeit für kardiotoxische Medikamente aufweisen und dass daher die Verwendung Krankheits-spezifischer hiPS-Kardiomyozyten unerwünschte Arzneimittelwirkungen akkurater vorhersagen könnte als der herkömmliche hERG-Assay oder Methoden, die auf gesunden Kontroll-hiPS-Zellen basieren.

Table of Contents

Abstract	I
Zusammenfassung	III
Abbreviations	IX
Part 1 Introduction	1
1.1 Stem cells	1
1.1.1 Types of stem cells	1
1.1.2 Human induced pluripotent stem cells and their applications in cardiovascular medicine	1
1.1.2.1 HiPSC reprogramming	1
1.1.2.2 Application of hiPSC in cardiovascular medicine	3
1.2 Cardiac disease modeling with human iPSCs	4
1.2.1 Cardiac differentiation of iPSCs: immaturity and heterogeneity	4
1.2.1.1 Cardiac differentiation and heterogeneity of hiPSC-CMs	4
1.2.1.2 Immaturity of hiPSC-CMs	4
1.2.2 Phenotyping of cardiac channelopathies and cardiomyopathies	6
1.2.2.1 Gene targeting in hiPSC models of cardiac disease	6
1.2.2.2 Modelling cardiac disorders using hiPSC-CMs	9
1.2.2.3 Long QT Syndrome	10
1.2.2.4 Cardiomyopathy	11
1.3 Drug screening/development and safety pharmacology with iPSC-CMs	16
1.3.1 Exon-skipping mediated antisense therapy	16
1.3.2 Optical membrane potential recordings for high-throughput cardiac toxicity testing	18
1.3.2.1 Preclinical evaluation of cardiac toxicology employing hiPSC-CMs	18
1.3.2.2 The cardiac action potential as a crucial readout for cardiac disease phenotypes and drug effects	20
1.3.2.3 Current methods for action potential measurement	23
1.3.2.4 Optical action potential measurement with genetically encoded voltage sensors	25
1.4 Aims of the studies	29
1.4.1 Exploring the mechanism of truncating titin-based DCM and its therapy using patient specific iPSC-CMs	29
1.4.2 Establishing cardiac subtype specific optical AP recordings in hiPSC-CMs	29

Table of Contents

Part 2 Materials and Methods	30
2.1 Individuals involved in the study and cell lines	30
2.2 HiPSC generation and characterization	31
2.3 HiPSC differentiation to the cardiac lineage	32
2.3.1 Differentiation of hiPSC in EBs and Monolayers.....	32
2.3.2 Single cell dissociation and drug treatment of hiPSC-CMs	33
2.4 Transfection of 2OMePS-AON to HL-1 cells and hiPSC-CM	33
2.5 Virus generation and hiPSC-CM infection	33
2.5.1 Generation of the U7snRNA lentiviral vectors encoding AONs.....	33
2.5.2 VSFP-encoding lentivirus constructs.....	34
2.5.3 Generation of AAVs encoding WT KCNQ1 and LacZ.....	34
2.6 Live-cell imaging of sarcomere dynamics in hiPSC-CM	35
2.7 Mass Spectrometry sample preparation and data processing	35
2.8 Reverse transcription PCR, quantitative real-time PCR and direct sequencing .	36
2.9 Immunocytological and alkaline phosphatase activity analysis	37
2.10 Optical membrane potential measurements	37
2.11 Statistics	38
Part 3 Results	39
3.1 Evaluation of Exon-skipping for treating TTN-based DCM	39
3.1.1 Characterization of DCM iPSCs	39
3.1.2 Disease phenotyping of DCM iPSC-CMs carrying the Ser14450fsX4 mutation in <i>TTN</i> exon 326	42
3.1.2.1 Sarcomere remodeling in actin-RFP transfected iPSC-CMs	42
3.1.2.2 Assessment of sarcomere assembly and stability in DCM and CTR1 hiPSC-CMs	44
3.1.2.3 Analysis of titin kinase associated signaling pathways.....	45
3.1.3 Rescue of DCM phenotypes by AON-mediated exon skipping	47
3.1.3.1 AON-mediated skipping of <i>TTN</i> exon 326	47
3.1.3.2 Rescue of sarcomere assembly and stability by skipping of <i>TTN</i> exon 326.....	51
3.1.3.3 Normalization of sarcomeric protein expression and Nbr1/p62/ SQSTM1/MURF2 signalosome by skipping of <i>TTN</i> exon 326.....	53
3.2 Subtype promoter-driven action potential imaging for precise disease modeling and drug testing in hiPSC-CMs	56
3.2.1 Optical AP recording in hiPSC-CMs using a VSFP sensor	56
3.2.1.1 Molecular characterization of hiPSC-CMs after PGK-VSFP lentiviral infection	56

Table of Contents

3.2.1.2	VSFP-based AP imaging in hiPSC-CMs.....	58
3.2.2	Subtype-specific optical AP recording of hiPSC-CMs	60
3.2.2.1	Identification of subtype-specific promoters in hiPSC-CMs	60
3.2.2.2	Marking of the ventricular lineage by MLC2v-VSFP.....	63
3.2.2.3	Marking of the atrial lineage by SLN-VSFP	63
3.2.2.4	Marking of the nodal lineage by SHOX2-VSFP	67
3.2.2.5	Functional validation of CM subtype-specific voltage sensor constructs.....	67
3.2.3	Modelling of Long QT syndrome type 1 using subtype-specific optical AP imaging of patient iPSC- CMs.....	71
3.2.3.1	Modelling of LQT1 syndrome with patient specific- and isogenic hiPSC-CMs	71
3.2.3.2	Discrimination of LQT1 phenotypes in hiPSC-CM subtypes.....	71
3.2.4	Long-term monitoring of AP dynamics in hiPSC-CMs with MLC2v- VSFP sensor	74
3.2.4.1	Probing the genetic rescue of the LQT1 disease phenotype in single patient iPSC-CMs by serial AP recordings.....	74
3.2.5	Investigation of drug effects by CM subtype-specific sensors.....	76
3.2.5.1	Evaluation of cisapride drug effects using the PGK-VSFP sensor.....	76
3.2.5.2	Discrimination of ivabradine bradycardic effects exclusively in nodal CMs using subtype-specific sensors.....	78
Part 4	Discussion	80
4.1	Recapitulation and rescue of DCM and LQT1 phenotypes in hiPSC- CMs	81
4.1.1	RNA-based therapy reversed defects of TTN-based DCM in patient hiPSC-CMs ..	81
4.1.1.1	hiPSC-derived cardiomyocytes as a human model for hereditary DCMs.....	81
4.1.1.2	AONs mediated exon skipping as a therapy for familial DCM.....	82
4.1.2	Genetic modification reversed LQT1 phenotypes	83
4.1.2.1	Successful modeling of LQT1 with patient-derived and isogenic hiPSC-CMs.....	83
4.1.2.2	<i>KCNQ1</i> ^{R190Q} mutation correction and WT <i>KCNQ1</i> overexpression rescued LQT1 phenotypes	86
4.1.3	hiPSC as a testing system for gene therapies in treating hereditary heart diseases	87
4.2	Subtype-specific AP recordings facilitate cardiac disease modelling and pharmacological investigation in healthy and diseased hiPSC-CMs.....	88
4.2.1	Optical AP recordings as a promising tool for large-scale cardiac drug discover and toxicity screening in healthy and diseased hiPSC-CMs	88
4.2.2	Subtype specific AP recordings enabled accurate phenotyping in LQT1 hiPSC-CM subtypes.....	90

Table of Contents

4.2.3	Subtype-specific AP recordings allowed sequential investigation of the same cells over extended time periods	90
4.2.4	Comparison of optical and electrode-based methods in action potential measurement	91
4.2.5	Potential applications of subtype AP recording in vitro and in vivo.....	93
4.3	Future scenarios of personalized medicine.....	93
Conclusion	96
Supplemental Tables	98
References	102
Articles	112
1	Antisense-mediated exon skipping: a therapeutic strategy for titin-based dilated cardiomyopathy. <i>EMBO Mol Med.</i> 2015 Mar 9; 7(5):562-76.	112
2	Subtype-specific promoter-driven action potential imaging for precise disease modeling and drug testing in hiPSC-derived cardiomyocytes. <i>European Heart Journal.</i> <i>in press</i>	112
Acknowledgements	113
EIGENSTÄNDIGKEITSERKLÄRUNG	115

Abbreviations

AAV	Adeno-associated virus
ALS	Amyotrophic lateral sclerosis
AP	Action potential
APD	Action potential duration
AON	Antisense oligonucleotide
APA	Action potential amplitude
ARVC	Arrhythmogenic right ventricular cardiomyopathy
AV node	Atrioventricular node
BMP	Bone morphogenetic protein
CaM	Calmodulin
CHO	Chinese hamster ovary
Chr	Channelrhodopsin
CI	Confidence intervals
Ci-VSP	Voltage-sensing domain of a phosphatase in <i>Ciona intestinalis</i>
cTNT	Cardiac troponin T
CM	Cardiomyocyte
CNM	Centronuclear myopathy
CPVT	Catecholaminergic polymorphic ventricular tachycardia
CR	Clover/mRuby2 FRET pair
Crispr/Cas9	Clustered Regularly Interspaced Short Palindromic Repeats
CTR	Control
CUPID	clinical trial of gene therapy on patients with heart failure
DCM	Dilated cardiomyopathy
DM	Myotonic dystrophy
DMAT	Distal myopathy with anterior tibial onset
DMD	Duchenne muscular dystrophy
DSBs	Double stranded DNA breaks
EAD	Early after depolarization
EB	Embryonic body
EBISC	European Bank for Induced Pluripotent Stem Cells
EC coupling	Excitation-Contraction Coupling
ECG	Electrocardiogram
ER	Endoplasmic reticulum
ESE	Exonic splicing enhancer
FGF	Fibroblast growth factor
FCMD	Fukuyama congenital muscular dystrophy
FDA	Federal drug administration
FNIII motifs	Fibronectin type III motifs.
FP	Fluorescence protein
FRET	Förster Resonance Energy Transfer
GEVI	Genetically encoded voltage sensor or indicator
GFP	Green fluorescent protein

Abbreviations

GSK3 β	Glycogen synthase kinase 3 beta
GWAS	Genome-wide association studies
HA	Human influenza hemagglutinin
HCM	Hypertrophic cardiomyopathy
HCN4	Hyperpolarization activated cyclic nucleotide gated potassium channel 4
HD	Huntington's disease
HEK	Human embryonic kidney cell lines
HERG	Human ether-a-go-go-related gene
hESC	Human embryonic stem cell
HMERF	Hereditary myopathy with early respiratory failure
hiPSC	Human induced pluripotent stem cell
hiPSC-CMs	hiPSC-derived cardiomyocytes
HIPSCI	hiPSCs initiative
hPSC	Human pluripotent stem cell
HSCs	Hematopoietic stem cells
HR	Homologous recombination
ISO	Isoprotenerol
IVF	In-vitro-Fertilization
KSR	Knockout serum replacement
LGMD2B	Limb girdle muscular dystrophy 2B
LGMD2J	Limb girdle muscular dystrophy type 2J
LPL	Lipoprotein lipase
LQTS2	Long QT syndrome type 2
LQTS1	Long QT syndrome type 1
LV	Left ventricle
MDP	Maximum diastolic potential
MEA	Multi-electrode array
MEF	Mouse embryonic fibroblast
MLC2a	Myosin light chain 2a
MLC2v	Myosin light chain 2v
MM	Miyoshi myopathy
MSCs	Mesenchymal stem cells
MURF	E3-ubiquitin ligase muscle ring finger proteins
MyBPC	Myosin-binding protein C
NCE	New chemical entity
NeoR	Neomycin resistance
NYSCF	New York Stem Cell Foundation
2' OMePS	2'-O-methyl phosphorothioate
PAA	Quantum 333 medium
PAM	Proto-spacer adjacent motif
PBMC	Periphery blood mononuclear cells
PEI	Polyethylenimine
PEVK domain	PEVK (Pro-Glu-Val-Lys) domain
PGD	Pre-implantation genetic diagnosis

Abbreviations

PGK	Phosphoglycerate kinase
PMO	Phosphorodiamidate morpholino oligomer
PSC	Pluripotent stem cell
PSF	Primary skin fibroblasts
qRT-PCR	Quantitative RT-PCR
RCM	Restrictive cardiomyopathy
RFP	Red fluorescence protein
rHA	Recombinant human albumin
RMP	Resting membrane potential
SAN	Sinoatrial node
SCs	Stem cells
SHOX2	Short sature homebox2
SLN	Sarcolipin
SMA	Spinal muscular atrophy
SR	Sarcoplasmic reticulum
SRF	Serum response factor
TALEN	Transcription activator-like effector nucleases
TdP	Torsades de pointes
TGF- β	Transforming growth factor beta
TTN	Titin (human)
Ttn	Titin (mouse)
TK	Titin kinase
vPMO	vivo-phosphorodiamidate morpholino oligomer
VSD	Voltage sensitive dye
VSFP	Voltage sensitive fluorescent protein
WNT	Wingless
WT	Wild type
ZFN	Zinc Finger Nucleases

Part 1 Introduction

1.1 Stem cells

1.1.1 Types of stem cells

Stem cells (SCs) have been defined as cells with the potential to proliferate and to differentiate to other cell types¹. Different SCs are involved in the developmental processes that transform a fertilized egg to an adult human being. SC niches also exist in almost all adult human tissues (e.g. mesenchymal stem cells (MSCs) in the bone marrow and adipose tissue²; hematopoietic stem cells (HSCs) in the bone marrow and blood³; neural⁴ and dermal⁵ SCs) and play roles in renewing the aged and damaged organs. These adult SCs⁶ retain only limited ability to proliferate and differentiate, limiting their value for scientific, pharmaceutical and clinical applications (Fig 1). SCs with a powerful potential of self-renewal and differentiation to all cell types of the human body have been defined as pluripotent stem cells (PSC). The prototype of human PSC are embryonic stem cells (hESCs)⁷, which were discovered in 1998 and can be isolated from the inner cell mass of a blastocyst (Fig 1). Due to their origin, the use of hESCs in biomedical research and cell therapy is a matter of ongoing ethical debates and is therefore restricted or even forbidden in many countries.

A novel type of hPSCs, which are generated by reprogramming somatic cells to pluripotency (Fig 1), has overcome the ethical restrictions of hESCs. First described in 2007 by Shinya Yamanaka⁸, these cells are named “human induced pluripotent stem cell” (hiPSCs). The perceived high impact of the hiPSC technology for the scientific community is illustrated by the fact that few years later, in 2012 when Shinya Yamanaka was awarded the Nobel Prize in Physiology or Medicine for such discovery.

1.1.2 Human induced pluripotent stem cells and their applications in cardiovascular medicine

1.1.2.1 HiPSC reprogramming

Shinya Yamanaka and colleagues developed a strategy to dedifferentiate human skin fibroblasts into hiPSCs by overexpressing 4 transcription factors (SOX2, c-MYC, OCT4 and KLF4) by retrovirus-mediated gene transfer⁸ (Fig1). Generation of hiPSCs challenged the

conventional notion that differentiation is an irreversible process, creating a completely novel and readily accessible system for pluripotent stem cell research and therapy. However, the original Yamanaka reprogramming protocol was reported to be lowly efficient (< 0.1%). Moreover, the use of integrating viruses is problematic with respect to future applications in cell therapy, given that random integration of viral genomes might activate endogenous oncogenes. After a decade of evolution, dermal fibroblasts, keratinocytes⁹, peripheral blood mononuclear cells¹⁰ (PBMC) and theoretically any adult cells¹¹ can be reprogrammed into hiPSCs with an improved efficiency of around 4% applying non-integrating Sendai-viruses, episomal plasmid or mRNA in chemically-defined medium on synthetic matrices¹². Thus, hiPSCs can be easily generated in academic and commercial labs. Moreover, large-scale hiPSC banks from healthy and diseased skin biopsy and blood donors are being created around the world, e.g. hiPSCs initiative (HIPSCI), New York Stem Cell Foundation (NYSCF), Innovative Medicines Initiative/STEMBANCC, European Bank for induced pluripotent Stem Cells (EBISC) and California Institute for Regenerative Medicine¹³, with the aim to facilitate the prediction, prevention and treatment of human diseases.

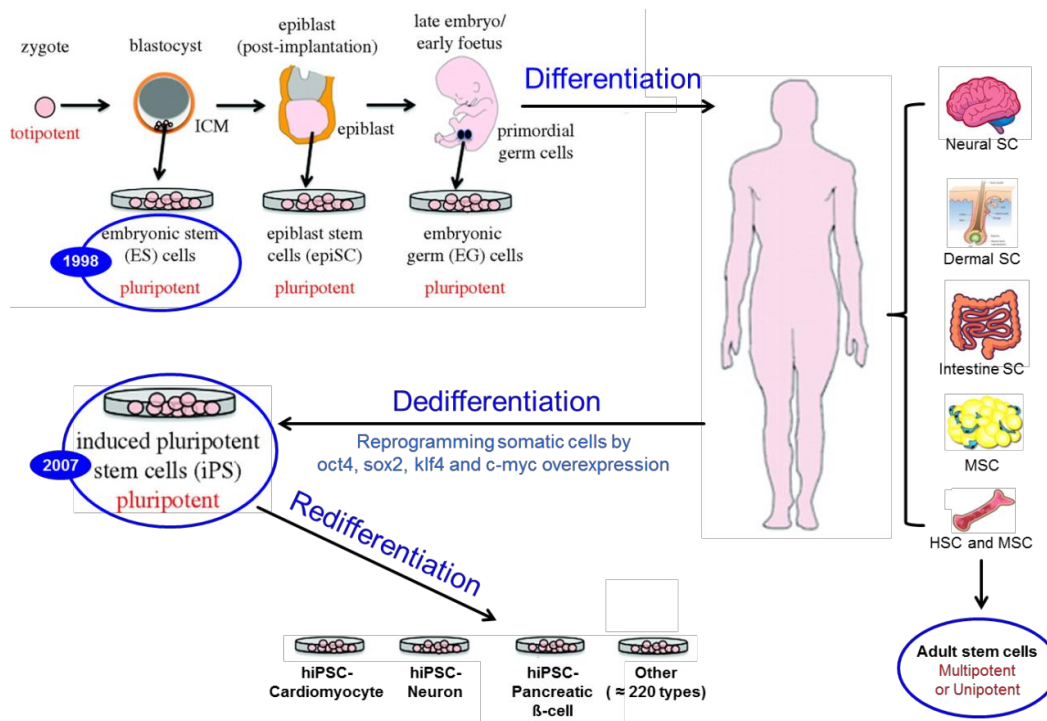


Figure 1: Stem cell definitions and sources. A stem cell is defined as a cell capable of proliferating for many passages and differentiating into function-specialized cells that constitute the tissues and organs of the body. There are three major types of stem cells (indicated in the blue circle): adult stem cells, embryonic stem cells, and induced pluripotent stem cells.

1.1.2.2 Application of hiPSC in cardiovascular medicine

Biological and medical researchers are seeking a better understanding of human diseases and ways to eventually predict, prevent and treat those diseases. To achieve these goals, better human disease models are needed. Many human diseases have been studied in animal models, which may be problematic since human physiology can be quite different from that of common animal models. Most notably, mouse models of human arrhythmias may have severe flaws given that the cardiac action potential of a mouse differs in several aspects (e.g. action potential duration and involved ion channels) from that of a human. Another way to study molecular mechanisms of human diseases is to use human cell lines with target genes overexpressed or downregulated, both of which cannot completely represent actual human physiological condition and therefore jeopardize the clinical translation of the corresponding scientific results. The major cause for the frequent use of these non-optimal models is the limited access to native human tissue and cells for physiological experiments, and the challenges of culturing primary cells in vitro.

Induced pluripotent stem cells (iPSCs) reprogrammed from adult somatic cell, which provide an unlimited source for human differentiated cells, may represent a solution of this problem. These cells, which can be cultured for many passages and differentiated into any human somatic cell type including cardiomyocytes, are proving particularly advantageous in understanding molecular mechanisms underlying cardiac diseases and investigating individual drug sensitivities.

Cardiovascular diseases are still the most prevalent cause of mortality in the Western world¹⁴. Potential applications of hiPSC-derived cardiomyocytes (hiPSC-CMs) range from basic research in the fields of heart development, cardiac disease modelling, drug discovery and safety pharmacology¹⁵ to tissue replacement in heart failure after myocardial infarction. Tissue replacement for the heart, although actively pursued, is still far from being routine clinical practice. By contrast, the use of these cells in safety pharmacology has already emerged¹⁶, with the aim to identify drug candidates that bear the potential of inducing QT interval prolongation and arrhythmia. Recent advances in methods for genetic engineering bear the potential to facilitate the study of patient-specific hiPSC-derived cardiac cells carrying disease related mutations or polymorphisms, broadening insight into disease mechanisms and promoting discovery of new therapies.

1.2 Cardiac disease modeling with human iPSCs

1.2.1 Cardiac differentiation of iPSCs: immaturity and heterogeneity

1.2.1.1 Cardiac differentiation and heterogeneity of hiPSC-CMs

In 2000, Joseph Itskovitz-Eldor's research group reported that contracting foci containing CMs could be generated by spontaneous differentiation of hESCs through three-dimensional floating embryoid bodies (EBs), which can be formed by aggregation of PSCs and comprise cells of the three embryonic germ layers¹⁷. This differentiation method gives rise to low percentages (5-10%) of cardiac cells and to a mixed population containing all three major myocyte subtypes in different proportions (~65%, ~30 and ~5% of ventricular, atrial and nodal myocytes, respectively).

Subsequent efforts aimed at improving the efficiency of cardiac differentiation have come to fruition within the past 3-4 years. Most newly-developed protocols are based on two-dimensional monolayers and involve stage-specific activation and inhibition of different signaling pathways in defined culture conditions, recapitulating key steps in early cardiac development¹⁸. For example, one of the widely used employs chemically-defined media supplemented with CHIR99021 (a GSK3 β inhibitor) for the first 2 days of differentiation, followed by Wnt inhibition through C59, IWR1, IWR4 or XAV939 for other 2 days¹⁸. In general, all the new methods of differentiating hPSCs in a directed manner produce beating sheets with 70 to 90% of CM yield. Other advantages of these protocols are the easier handling, the scalability of CM production, and the improved reproducibility. However, similarly to the spontaneous floating hPSC-EB method, all produce a mixture of CM subtypes containing ventricular-, atrial- and nodal-like cells. Although highly desirable, to date, no subtype-specific differentiation protocols exist and their development is currently a topic of intensive research.

1.2.1.2 Immaturity of hiPSC-CMs

A typical feature of hiPSC-CMs is that they remain immature and resemble heart cells at the development stage of mid-gestation human fetuses. At the functional level, they exhibit disarranged sarcomeres, weaker contraction forces and smaller action potential amplitudes as compared to adult working cardiomyocytes¹⁹. At the molecular level, hiPSC-CMs not only display reduced expression of sarcomeric and ion channel genes, but also distinct transcription patterns of lineage-specific genes when compared with their adult counterparts; for example in

adult myocardium, the myosin light chain 2a (MLC2a) gene is restricted to cells of the atria. In hiPSC-CMs, however, MLC2a was reported to be expressed in all three major cardiac subtypes (ventricular, atrial, and nodal)¹⁹. A similar promiscuous expression pattern has been observed for the hyperpolarization activated cyclic nucleotide gated potassium channel 4 (HCN4) gene, which is specifically expressed in the sinus and atrioventricular node regions in adult myocardium¹⁹.

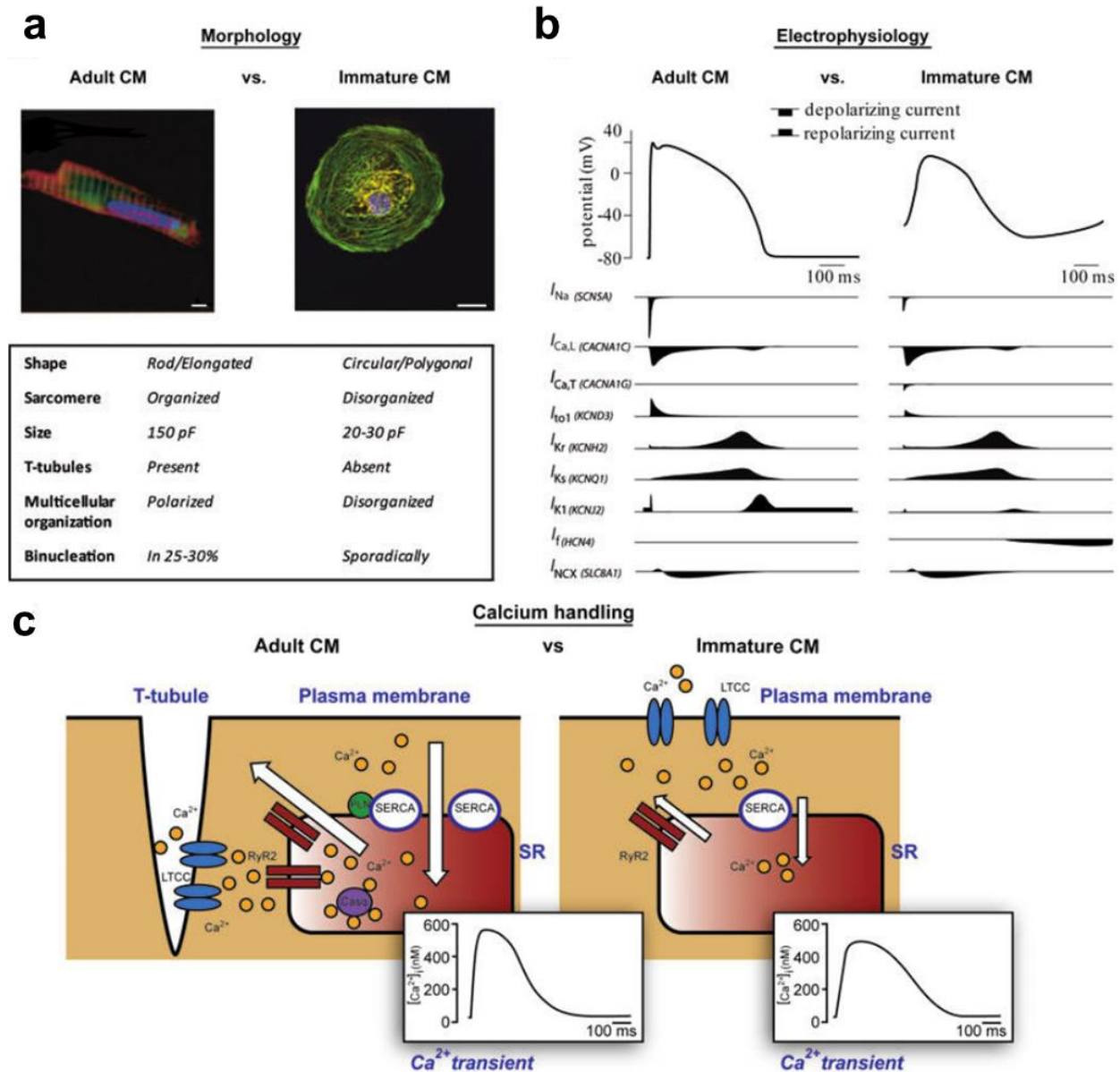


Figure 2: Immaturity of hiPSC-CMs in comparison with their adult counterparts. Comparison of morphological (a), electrophysiological (b) and calcium handling-related (c) properties of adult (mature) and hiPSC-derived (immature) human CMs. (a) Immunofluorescence image of an adult human atrial CM stained with anti-alpha-actinin (green)

and anti-MLC2a (red) and a hiPSC-CM stained with anti-cardiac Troponin I (green) and anti-alpha-actinin (red). Scale bars are 100 μm for the left panel and 25 μm for the right. **(b)** Representative action potential traces of adult ventricular and hiPSC-derived immature CMs and their accompanying ion currents as indicated. Note the slower upstroke, smaller amplitude and less negative resting membrane potential in the immature CMs compared to the adult CMs, which correlates to lower densities of I_{K1} , I_{Na} and I_{to1} . The corresponding genes of the ion currents are stated in parenthesis. **(c)** Illustrative scheme showing Ca^{2+} influx and extrusion in adult and immature CMs. Inset shows the typical Ca^{2+} transients. Figure is adapted from ¹⁹.

Although hiPSC-CMs have been successfully used to model early-onset congenital heart disease (e.g. genetic channelopathies and cardiomyopathies), the immaturity limits their application for studying human adult cardiac physiology and cardiovascular pathology associated with acquired factors. In the context of cardiac tissue regeneration, their immature characteristics such as automaticity, poor excitation-contraction coupling and slow conduction, may cause potentially dangerous arrhythmogenicity after transplantation to the heart²⁰. Therefore, inducing maturation of hiPSC-CMs would significantly promote their application in the laboratory and for possible future clinical applications.

1.2.2 Phenotyping of cardiac channelopathies and cardiomyopathies

1.2.2.1 Gene targeting in hiPSC models of cardiac disease

The key to modeling disease with hiPSCs is to identify a disease-relevant cellular pathology with a robust phenotype. Early-onset diseases with a strong genetic influence and affecting a highly-defined cell or tissue type have been the first choice for hiPSC-based disease modeling. The genetic cause of many cardiac diseases is not completely understood, even though nowadays most are appreciated to stem from genetic variants. Several rare DNA variants, common DNA variants and chromosomal abnormalities have been associated with congenital heart disease²¹, and many mutations in genes encoding sarcomeric proteins and cardiac ion channels have been identified in several cardiomyopathies and channelopathies. Before the advent of hiPSC technology, research has been performed using diseased hESC lines from embryos obtained for pre-implantation genetic diagnosis (PGD)²² or generated by gene editing²³. However, PGD is only available for a limited number of genetic conditions, few research groups have access to these facilities, and the scientific use of human embryos (even those harboring detrimental genetic lesions) is ethically sensitive and restricted in many countries. Similarly, gene editing by homologous recombination (HR) was initially successful in a few cases to generate knockouts (e.g. HPRT1 knockout in patient iPSCs to model Lesch-Nyhan syndrome, a metabolic disorder²³) or create reporter constructs downstream of important early developmental genes, such as

NKX2.5²⁴. In rare cases, generation of isogenic pairs was used to evaluate role of mutations in genes such as *KCNH2*, which encodes a subunit of the I_{Kr} potassium channel and underlies the Long QT syndrome type 2 (LQTS2)²⁵. A problem with this approach is the low recombination frequency (~1 in 100 cells) in most mammalian cells, which makes the generation of isogenic models a challenge because of the required biallelic targeting. Nevertheless, progress in gene editing tools now enables more rapid engineering of the genome in hPSCs.

It has been known for 25 years that an introduction of double strand breaks (DSBs) at a specific locus can improve the efficiency of gene targeting approaches. Complexing the Fok1 endonuclease with a pair of zinc finger nucleases (ZFNs)²³ allowed gene targeting of a model GFP locus in HEK 293 T cells and the endogenous *PIG-A* locus in hPSCs resulting in a 200- to 2000-fold improvement of gene targeting efficiency. However, each ZFN construct has to be specifically designed, resulting in costs as high as USD \$25,000.

The transcription activator-like effector nucleases (TALENs) share the same principles with ZFNs, relying on a dimeric protein-based DNA binding domain fused to an endonuclease. Construction kits, such as FLASH assembly²⁶ and GoldenGate²⁷, allow individual labs to produce their own TALEN vectors, thereby reducing the costs by 20-fold in comparison to ZFNs. In addition, TALENs not only showed greater specificity in hPSCs, but also less off-target activity and toxicity compared to ZFNs²⁸.

The next breakthrough in gene targeting came with the advent of the Clustered Regularly Interspaced Short Palindromic Repeat (Cas9/ CRISPR) system²⁹ (Fig 3). This system was developed based on a nuclease involved in the immune defense of various strains of bacteria against bacteriophages. It relies on 100 bp site-specific guide RNA (gRNA) directing the Cas9 endonuclease to a specific target site, eliminating the time-consuming production of a fused endonuclease for DNA binding and DSB creation³⁰. This novel targeting approach has been used to perform exon skipping, frameshifting and exon knock-in in hiPSC lines carrying disease causing mutations of Duchenne muscular dystrophy (DMD), underlying severe muscular degenerative disease³¹. The use of the Cas9/CRISPR system has been quickly taken up by the scientific community, with over 20 publications per week in PubMed in 2015. Biotechnology providers are offering constructs to target every gene of human and mouse, and projects in progress in the Wellcome Trust Sanger Institute aim at producing a panel of mESC lines harboring complete knockouts of every gene in the mouse genome.

1.2.2.2 Modelling cardiac disorders using hiPSC-CMs

Patient-specific iPSC-CMs are increasingly used to investigate disease phenotypes and therapeutical approaches to rescue these phenotypes. So far, the most intensively studied are various cardiac channelopathies, including several types of long QT syndromes (LQTS; LQT1³³, LQT2³⁴, LQT3³⁵ and LQT8³⁶), Brugada/LQTS3 overlap syndrome³⁷ and catecholaminergic polymorphic ventricular tachycardia (CPVT)³⁸, followed by disorders affecting myocyte structure, contractility and survival, such as Duchenne muscular dystrophy (DMD)³⁹, hypertrophic cardiomyopathy (HCM)⁴⁰, Barth Syndrome⁴¹, dilated cardiomyopathy⁴², Leopard Syndrome⁴³ and arrhythmogenic right ventricular cardiomyopathy (ARVC)⁴⁴. These patient-specific iPSC models have been employed to understand disease mechanisms and test novel therapeutics. For instance, trichostain A was reported to prevent hypertrophy in a HCM iPSC-CM model, while dantrolene was shown to abolish stress-induced arrhythmias in CPVT1 iPSC-CMs³⁸. Efficacy of genetic interventions were also evaluated, including exon skipping in to rescue DMD⁴⁵ and allele-specific RNAi to reverse LQTS2 in corresponding diseased hiPSC-CMs⁴⁶.

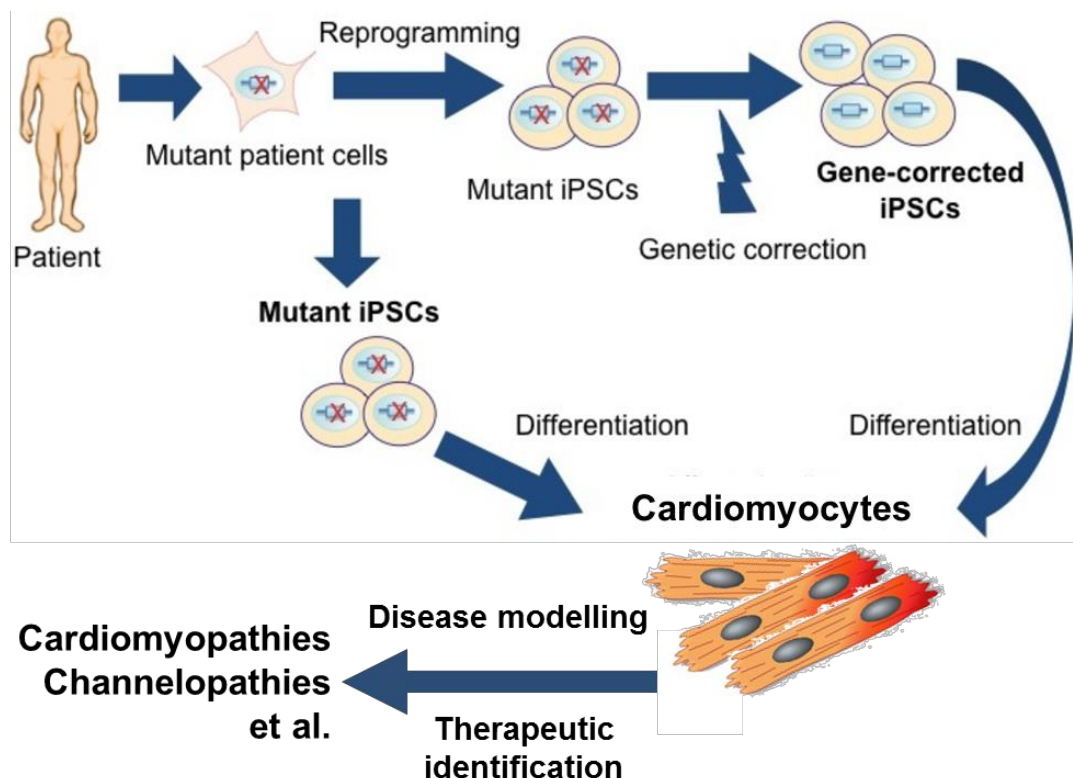


Figure 4: Patient iPSCs represent an unprecedented tool for the generation of in vitro platforms for disease modelling (e.g. cardiomyopathies and channelopathies). The correction of the potential disease-causing mutations may help to understand the molecular and cellular mechanisms driving the disease pathogenesis, and, more importantly, to identify therapeutic targets for the disease. Figure is reproduced based on ⁴⁷.

1.2.2.3 Long QT Syndrome

Phenotype and genotype of Long QT syndromes

Long QT syndromes (LQTS), clinically diagnosed based on a prolongation of the QT interval in the electrocardiogram (ECG) over the normal range of 350 to 440 milliseconds, are inherited or acquired cardiac disorder in which repolarization of the cardiac action potential is delayed. This increases the risk of torsade's de pointes (Tdp) tachycardia, an arrhythmia of the ventricular myocardium, which may lead to ventricular fibrillation and manifests clinically as fainting, palpitations, and sudden death. LQTS has an incidence of 1 in 2500 to 7000 people. In addition to drug-induced LQTS (e.g. caused by cisapride, erythromycin or terfenadine), genetic mutations in 13 genes have been discovered causing familial LQTS, which is classified as LQT1 to LQT13 depending on the mutated gene. All the 13 LQT-related genes may directly or indirectly cause defective transmembrane ion currents during the depolarization or repolarization phase of the cardiac action potential. Moreover, LQT-related mutations may increase the susceptibility to drug induced QT interval prolongation. In addition, patients with other diseases such as type 1 diabetes, type 2 diabetes and rheumatoid arthritis may be predisposed to LQTS. Currently, medical treatment of LQT syndromes is mainly limited to beta blockers, with the option of prophylactic cardioverter-defibrillator implantation in selected cases with high risk of sudden cardiac death. Moreover, LQT patients are susceptible to induction of arrhythmias by various cardiac and non-cardiac drugs.

Disease models based on hiPSCs have been proposed to address the problem of clinical management of patients with LQTS by using patient-derived iPSC-CMs as an in vitro platform to investigate the therapeutic and arrhythmogenic potential of drugs and to find an optimal therapy regime for the specific patient.

Modeling of LQT1 syndrome with patient specific iPSC-CMs

The most common type of LQTS is LQT1, taking up 30 to 35% among all the cases. LQT1 is caused by mutations in the *KCNQ1* gene that encodes the alpha subunit of the ion channel conducting the slow component of the delayed rectifier potassium current (I_{Ks} current). *KCNQ1* mutations cause a defective repolarization phase of the action potential presenting as a prolonged QT interval and an increased incidence of early afterdepolarizations (EADs). In a patient-specific iPSC-CMs model for LQT1 caused by a R190Q point mutation in *KCNQ1*, the patient CMs maintained the disease genotype and recapitulated the phenotypic features of the

disorder³³. In the LQT1 iPSC-CMs, action potential duration was markedly prolonged in ventricular- and atrial- like myocytes but not in nodal-like cells, which was assessed by patch clamp electrophysiology. The disease pathogenesis caused by the KCNQ1^{R190Q} mutation was identified as a dominant negative trafficking defect of the mutated ion channel subunits, concurrent with a 70-80% reduction of I_{ks} current and altered channel activity. In addition, an increased susceptibility to catecholamine-induced arrhythmia was also shown in patient iPSC-CMs, while beta-blockade attenuated the arrhythmogenic phenotype.

Isogenic models of LQT2 syndrome

Incidence of LQT2, while lower than that of LQT1, still reaches 25 to 30% among all LQT cases. The disease-causing mutations of LQT2 locate to the *KCNH2* (also known as hERG) gene encoding the ion channel responsible for the rapid component of the delayed rectifier potassium current (I_{Kr} current). In a study investigating LQT2 associated with a *KCNH2*^{N996I} missense mutation using hiPSC-CMs, the point mutation was both corrected in the LQT2 iPSC line and introduced into disease-free hESCs at the genomic level, generating two isogenic pairs of pluripotent stem cell lines with distinct genetic background²⁵. Genetic correction of the mutation normalized the HERG-mediated I_{Kr} current and the AP prolongation in the patient-derived hiPSC-CMs. Knock-in of the same mutation into healthy hESCs attenuated I_{Kr} current and resulted in AP prolongation in hESC-CMs. The consistent results from the two isogenic pairs robustly confirmed the *KCNH2*^{N996I} mutation as the primary disease-causing mutation.

This is a clear advantage over the use of unrelated hiPSCs as control lines, which may be always result in confounding effects of the distinct genetic background on the genotype-phenotype correlation of the disease-causing mutation. This may be especially relevant in diseases with incomplete penetrance.

1.2.2.4 Cardiomyopathy

Genetic association of Cardiomyopathy

Cardiomyopathy is a heterogeneous group of cardiac disorders in which the myocardium shows structural and functional defects in the absence of hypertension, coronary artery disease, valvular, or congenital heart disease⁴⁸. These disorders include dilated cardiomyopathy (DCM), hypertrophic cardiomyopathy (HCM), arrhythmogenic right-ventricular cardiomyopathy (ARVC)⁴⁹. In the past decade, cardiomyopathy was increasingly associated with a large number of

mutations in genes encoding sarcomeric, desmosomal, and signaling-related proteins (Fig 5). Among them, DCM is the most common type, occurring in 1 of 3000 individuals⁵⁰. The typical age of disease manifestation ranges from 20 to 60 years, and men are more frequently affected than women. The first clinical sign is an enlargement of the left (systemic) ventricle and progressive thinning of the myocardium. A progressive reduction of the left-ventricular ejection fraction is observed. Eventually, the condition of chamber enlargement and myocardial thinning may spread to the right ventricle and the atria, resulting in a deterioration of global cardiac function and terminal heart failure. Up to one third of total DCM cases can be attributed to a familial genetic cause⁵¹.

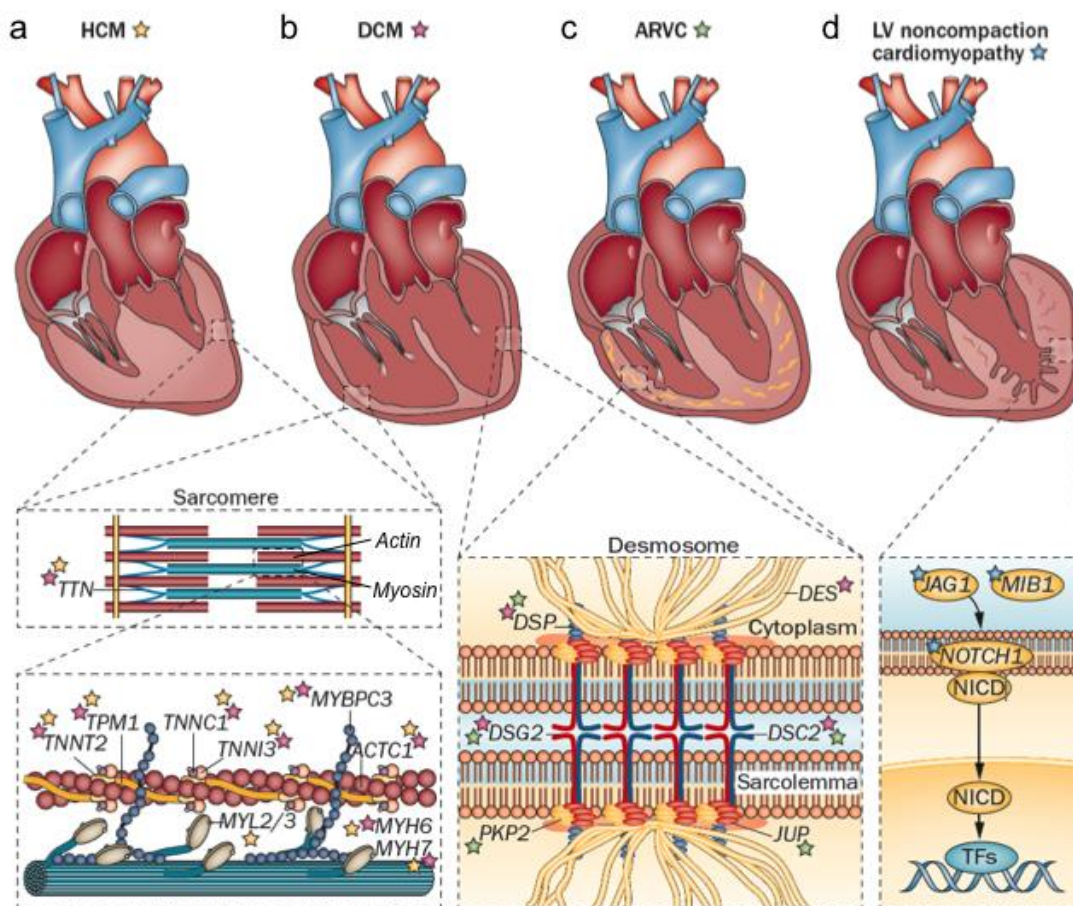


Figure 5: Genetically-caused cardiomyopathies. (a) Mutations in *TTN* and other sarcomeric genes have been linked with hypertrophic cardiomyopathy (HCM) (yellow stars). (b) Similarly, mutations in genes encoding either desmosomal or sarcomeric proteins have been shown to cause dilated cardiomyopathy (DCM) (pink stars). (c) Gene mutations of desmosomal proteins have also been implicated in the pathogenesis of arrhythmogenic right ventricular cardiomyopathy (ARVC) (green stars). (d) Gene mutations involved in NOTCH1 signaling are reported to underlie Left ventricular (LV) noncompaction cardiomyopathy (blue stars).

Abbreviations: NOTCH1 intracellular domain (NICD1); transcription factor (TF). Figure is adapted from ⁵².

Hereditary DCM can be autosomal dominant, X-linked, and autosomal recessive^{53, 54}. The development of large genetic databases that include phenotypically-defined populations from different ethnic origin, such as the 1000 Genomes Project and the Exome Sequencing Project, has allowed researchers to precisely identify the potential disease-causing variants. For example, the largest human gene *TTN*, encoding a protein that is ~1 μm long and spans half of a sarcomere, could be successfully investigated in genetic studies applying next-generation sequencing, demonstrating that *TTN* mutations resulting in a truncated protein could be identified in 14% of DCM patients. This number was even increased to 27% when parallel-capture next-generation sequencing was used. These findings increased the number (up to 70%) of DCM patients who harbor a known genetic mutation in *TTN* and established it as the gene most-commonly associated with DCM^{55, 56}.

Structure of sarcomere and titin

The sarcomere is the basic unit of striated muscle and the molecular engine that powers muscle tissue. It consists of long and fibrous proteins that slide past each other, thereby mediating contraction and relaxation of the muscle. Two of the important fibrous proteins are myosin that forms the thick filament and actin that assembles the thin filament (Fig 6). Myosin has a long, fibrous tail and a globular head, which binds to actin when it is coupled with ATP, which provides energy for muscle movement. For initiation of contraction, myosin binds to actin when the binding sites of actin are exposed by Ca^{2+} binding.

A sarcomere is defined as the segment between two neighbouring Z-lines (or Z bodies, or Z-discs). The Z-line (from German "Zwischenscheibe", meaning "intercalated disc") appears as a series of dark lines between two I bands. I-band represents the zone of the sarcomere where thin filaments are not superimposed by thick filaments. I-bands alternate with A-band, which contain the entire length of a thick filament. A paler region of the A-band, called H-zone, represents an area in the A band without I band coverage. In the middle of the H-zone, a thin M-line cross-connects sarcomeres and the cytoskeleton.

The giant protein titin encoded by the *TTN* gene extends from the Z-line of the sarcomere to the M-band. Titin consists of four structurally and functionally distinct regions: the N-terminal Z-line, the I-band and A-band regions that majorly constitute the protein, and the C-terminal M-line

extremity. The entire *TTN* gene, which consists of 364 exons, is located on chromosome 2q31 and transcribes to an mRNA of over 100 kb length that could hypothetically produce a 38,138 amino acid residues, (4,200 kDa protein)⁵⁷. Titin is the biggest single protein found in nature and the third most abundant type of filament (except actin and myosin filament) in both cardiac and skeletal human muscle⁵⁸. One single titin filament bridges half a sarcomere along its longitudinal axis from the Z-disk to the M-line interacting with numerous protein partners (Fig 6). The M-line region of titin is encoded by the last six exons of *TTN*⁶⁹ and contains a unique serine-threonine kinase domain (TK)⁶⁰ that regulates expression and turnover of sarcomeric protein⁶¹.

Titin plays multiple roles in all striated muscle cells. Its massive size and complex structure suggest that it plays a role as an architectural protein providing docking sites to a plethora of other proteins^{62,63}. Thus, titin acts as a molecular blueprint for assembly and organization of myosin thick filaments during myofibrillogenesis⁶⁴, maintains the sarcomeric proteins in place during contraction⁶⁵, enables force transmission at the Z-line and keeps the resting tension in the I-band^{60,66}, and is also a sensor and signaling mediator, a function for which its TK domain plays an essential role^{67,68}. A-band titin is considered as a protein ruler for thick filament assembly, providing intense interactions with myosin⁵⁷ and a significantly weaker binding with myosin-binding protein C (MyBPC)^{64,65}. The E3-ubiquitin ligase muscle ring finger proteins (MURF) play important functions throughout muscle development⁶⁹ and bind to titin at the end of the A-band. MURF2 binds to titin A164–A169 domains and MURF1 to the A168–A169 repeats close to the periphery of the M-band^{70,71}. The titin TK domain functions as a mechanical strain sensor during muscle contraction and the mechanism seems to involve Ca²⁺-calmodulin binding that unlocks the ATP-binding site^{72,61}. The TK also interacts with the zinc-finger protein nbr1-related zinc finger protein p62, and nbr1 when it has an open or active conformation induced by mechanical stretch⁶¹.

Clinical Relevance of TTN Mutations

Due to the function, size, and structure of titin and its interactions with multiple binding proteins, different *TTN* mutations can have diverse biological effects and different clinical manifestations. The majority of *TTN* mutations have been associated with purely cardiac phenotypes, including DCM, ARVC, HCM, and monogenic restrictive cardiomyopathy (RCM)⁷³. Thirty-five mutations have been reported to lead to purely skeletal muscle phenotypes, including limb girdle muscular dystrophy type 2J (LGMD2J)⁷⁴, late-onset TMD⁷⁵, centronuclear myopathy (CNM)⁷⁶ and hereditary myopathy with early respiratory failure (HMERF)⁷⁷. Nine mutations that affect both

cardiac and skeletal muscle tissues have been characterized in six families presenting with an autosomal-recessive form congenital skeletal myopathy and various forms of heart disease ⁷⁶.

Among the phenotypes associated with *TTN* mutations, DCM is the most widely reported, with 69 mutations identified in DCM subjects ^{78,79,80,81}. In a recent screening for DCM disease variants by sequencing a large cohort of 766 patients, genetic variants in *TTN* were reported in up to 14% of subjects ⁸². Out of the reported DCM-associated *TTN* mutations, 29 were nonsense mutation (three in the I-band and the remaining 26 in the A-band), 17 were frameshift mutations (three occurring in the I-band and 14 in the A-band), seven were missense mutations (three in the Z-line, three in the I-band and one in the M-line) and 18 were predicted to have an impact on *TTN* splicing.

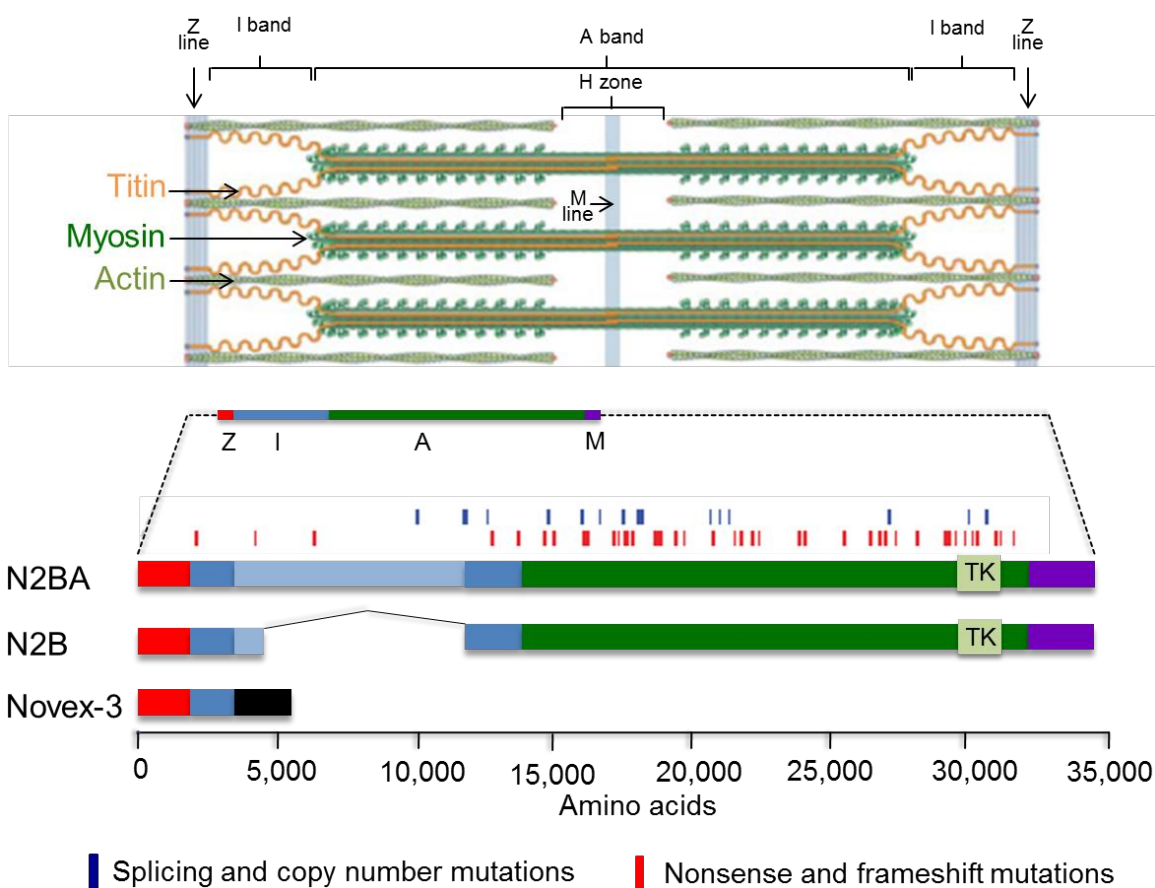


Figure 6: Structure of the cardiac sarcomere and spatial distribution of known *TTN* Mutations. The cardiac sarcomere (top) consists of the thick filaments (green rods with globular heads), thin filaments (coiled ovals in light green) and titin filaments (orange). The distinct regions of the sarcomere are indicated on the top. The regions of titin corresponding to these regions are color-coded as Z-disk (red), I-band (blue), A-band (green), and M-band (purple). *TTN* mutations are displayed as thin vertical bars (middle) and overlapping mutations appear as thicker bars. Splicing and copy-number mutations (blue) and nonsense and frameshift mutations

(red) identified in patients with dilated cardiomyopathy are shown. The different Titin isoforms are shown (bottom). Titin isoforms N2BA and N2B span half of the sarcomere, while novex-3 titin is shorter and less abundant (a black bar indicates the exon specific to novex-3 isoform). Figure is reproduced based on ⁵⁵.

Little is known about the precise biological and pathophysiological mechanisms of the different forms of DCM caused by the distinct *TTN* mutations, due to the rare availability of patients' myocardial tissue and the technical challenges in studying such a huge and complex protein. However, the biological effects on titin binding partners can be more easily investigated. Thus, two DCM missense mutations (c.2228C>T, p.Ala743Val and c.160G>A, p.Val54Met) in Z-line titin have been reported to reduce the binding of T-cap and α -actinin, respectively, in yeast-two-hybrid assays ⁸³.

1.3 Drug screening/development and safety pharmacology with iPSC-CMs

1.3.1 Exon-skipping mediated antisense therapy

Antisense therapy is an approach to treating genetic diseases using short RNA-like molecules called antisense oligonucleotides (AONs), which rely on the function of splice machinery, specifically anneal to the pre-mRNA target and modify the gene expression at pre-mRNA level. Chemically modified oligonucleotides, e.g. methylphosphonate and morpholino, are frequently used in order to limit nuclease sensitivity in an effort to enhance their stability as antisense agents.

Recently, antisense therapy has emerged as an exciting and promising strategy for the treatment of various degenerative muscular disorders. Previous and ongoing pre-clinical and clinical trials have provided encouraging early results. Duchenne muscular dystrophy (DMD), spinal muscular atrophy (SMA), Huntington's disease (HD), amyotrophic lateral sclerosis (ALS), Fukuyama congenital muscular dystrophy (FCMD), dysferlinopathy (including limb-girdle muscular dystrophy 2B; LGMD2B, Miyoshi myopathy; MM, and distal myopathy with anterior tibial onset; DMAT), and myotonic dystrophy (DM) are all reported to be promising targets for antisense therapy ⁸⁴. However, therapeutic antisense strategies for these disorders are quite different. For example, to target DMD, antisense-mediated exon skipping can remove nonsense mutations or frame-shifting mutations from mRNA ⁸⁵⁻⁸⁷. To treat the mutation in the *FCMD* gene, a cocktail of vivo-morpholino AONs targeting splice enhancer sites and splice silencer sites led

to correction of the aberrant splicing pattern in cellular and mouse models⁸⁸. RNase H1-mediated degradation of toxic RNA with 2'-MOE antisense for myotonic dystrophy type 1 showed very promising results in the mouse model⁸⁹. A unique “knock up” approach (exon inclusion) targeting the *SMN2* gene with 2'-methoxyethoxy (2'-MOE) antisense or the phosphorodiamidate morpholino oligomer (PMO, morpholino) has been used to treat SMA^{90,91}.

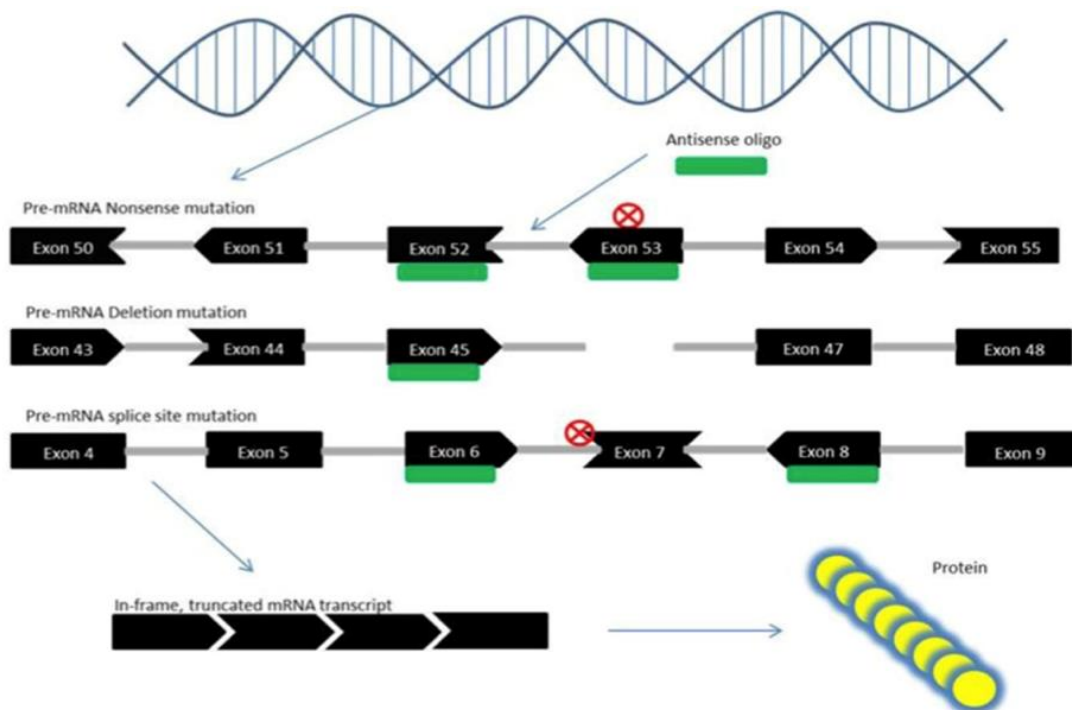


Figure 7: Scheme of exon skipping therapy for Duchenne muscular dystrophy (DMD). Nonsense mutations (indicated by a red cross in a circle) in the DMD gene create a STOP codon resulting in the loss of DMD protein (depicted in the upper pre-mRNA sequence). Exon skipping corrects these errors when antisense oligos (green) are bound to the targeted exons (black) that will be spliced out of the pre-mRNA, resulting in an in-frame mRNA. Out-of-frame mutations caused by the loss of exons (depicted in the middle pre-mRNA sequence) and splice site mutations (depicted in the lower pre-mRNA sequence) can also be corrected by removing exons adjacent to the mutated locus so that the remaining exons are in-frame. The exon skipping will result in an internally-truncated yet partly functional protein. Figure is adapted from⁸⁴.

The most widely investigated therapeutic approach so far is the antisense therapy for DMD, which is an X-linked recessive muscular dystrophy caused by mutations in dystrophin gene⁹², affecting roughly one in 3,500 boys worldwide and leading to muscular degeneration and eventual death⁹². Recently, exon skipping has been intensively explored as the therapy of DMD^{93, 94}. Exon skipping uses AONs designed in order to prevent the incorporation of the exon carrying the mutation into the mRNA. Ideally, in case of frameshift mutations, this leads to a

restoration of the reading frame of the protein (Fig 7)⁹⁵. It is noteworthy that skipping of mutated exons occurs in DMD patients and animal models spontaneously to some extent^{96, 97}. The efficacy of AON-mediated exon skipping was evaluated in several animal and cellular models including dystrophic *mdx* mice, dystrophic dogs and human DMD cells^{98–107}. Recently, clinical trials are being performed targeting exon 51 of the DMD gene with PMOs and 2'-O-methylphosphorothioate-modified (2'OMePS) AONs, presenting very promising results^{108–111}. In addition, the first clinical trial targeting DMD exon 53 skipping has been started in Japan in 2013 by Nippon Shinyaku Co. Ltd. and the Japanese National Center of Neurology (UMIN-CTR Clinical Trial number UMIN000010964).

Remaining challenges in therapeutic application of AON-mediated exon skipping include: 1) the limited targeting efficiency of AONs, especially in the heart, 2) unpredictable long-term safety, 3) limited applicability (only ~10% of DMD patients can be treated with a skipping therapy targeting exon 51 or exon 53). Previously, efficacy tests of preclinical antisense therapy have been conducted in animal models and engineered human cells. Patient iPSC-derived cell types (e.g. skeleton and cardiac myocytes) might represent a more specific model system to develop and investigate specific antisense therapies for particular patients.

1.3.2 Optical membrane potential recordings for high-throughput cardiac toxicity testing

1.3.2.1 Preclinical evaluation of cardiac toxicology employing hiPSC-CMs

Cardiac toxicity is an important liability of novel drug candidates and may manifest as electrophysiological dysfunction or cardiac muscle damage, potentially leading to cardiac arrest or heart failure. Suspected cardiotoxicity is a major reason for discontinuation of the preclinical development of particular candidate drugs in the pharmaceutical industry. Of leading concern is the potential side effect of new chemical entities (NCEs) to prolong the QT interval in the ECG, which may result in life-threatening ventricular arrhythmias. In order to minimize such risks, regulatory bodies such as the U.S. Food and Drug Administration have mandated cardiotoxicity tests in the early stage of NCE development including *in vitro* assays for electrophysiology, Ca²⁺ dynamics, and contractility¹¹².

Currently, early cardiac toxicity screening is performed in genetically modified human embryonic kidney cell lines (HEK) and Chinese hamster ovary line (CHO) artificially overexpressing single channels such as the hERG channel. These tests are compromised by their inability to assess

the combined action of the candidate drug on the large set of ion channels present in a human cardiomyocyte, and the overall effect of these actions on single channels on action potential morphology and arrhythmogenicity¹¹³. In addition, the validity of experiments performed in immortalized cell lines is impaired by their accumulation of genetic aberrations and failed ectopic expression of channels, which challenges the accuracy of modelling the corresponding channels in human primary cardiomyocytes. Consequently, NCEs tested with HEK and CHO cells could generate false-positive (e.g. verapamil) or false-negative (e.g. alfuzosin) test results, which may result either in progression of dangerous drugs to clinical trials or in withdrawal of effective and safe drugs from the further evaluation process^{114–117}.

Preclinical cardiotoxicity assays are further conducted in animal models (e.g. murine, canine and primate models), which may be hampered by the electrophysiological differences between human and non-human hearts. Thus, ideally, preclinical cardiac toxicity test should be performed on human cardiomyocytes. Unfortunately, this has been infeasible for early stage drug screening due to restricted accesses to patients' cardiac tissue and inability to culture and passage isolated primary cardiomyocytes for extended time periods. Even in the late stage of cardiotoxicity screening, very limited amounts of patient primary cardiomyocytes could be applied, and the reliability of the result derived from these few cases might be questionable.

Generation of human CMs from PSCs (hESC-CMs and hiPSC-CMs) may represent a way to circumvent the above-mentioned hurdles, because they provide an unlimited source of cells for differentiation to CMs^{118,119}. Moreover, the PSC-derived CMs resemble electrical properties of primary human CMs. Reprogramming somatic cells (e.g. dermal fibroblasts or blood PBMCs) to hiPSC provides a unique opportunity to obtain patient-specific iPSC-derived CMs that maintain patient specific genotypes and disease phenotypes. Toxicity screening in patient-derived iPSC-CMs might additionally benefit from the fact that cardiac drug side effects are particularly frequent in individuals with pre-existing cardiac abnormalities. For instance, the well-known withdrawing of the gastromotility drug cisapride in 2008 was due to its inducing episodes of TdP and sudden cardiac death in individuals with pre-existing cardiac disorders (i.e. long QT syndrome and heart failure)¹²⁰. Therefore, iPSC-CMs derived from individuals with genetic cardiac disorders might turn out as particularly sensitive to drug-induced cardiotoxicity. Patient iPSC-CMs have been generated from patients with long QT syndrome, CPVT, DCM, ARVC, hypertrophic cardiomyopathy (HCM) and LEOPARD syndrome^{34,121,43,42,38,122}. These patient iPSC-CMs, which successfully recapitulated the major disease phenotypes, might offer an

unprecedentedly vulnerable cell base for cardiac toxicity assays including torsadogenic responses, Ca^{2+} dynamics, contractility and other cardiac phenotypes.

1.3.2.2 The cardiac action potential as a crucial readout for cardiac disease phenotypes and drug effects

The cardiac action potential

Excitable cells, such as neurons and myocytes, are able to generate a rapid electrical signal characterized by a rapid depolarization followed by a repolarization of the membrane potential, named action potential (AP). In the heart, APs mediate the conduction of the signal across the functional syncytium of cardiomyocytes and initiate the systolic Ca^{2+} influx that promotes further Ca^{2+} release from the sarcoplasmic reticulum (SR), which binds to muscle filaments and thereby triggers the myocardial contraction¹²³. The AP is shaped by the concerted opening and closure of several ion channels in the plasma membrane, resulting in ionic (Na^+ , K^+ , Ca^{2+} and Cl^-) currents driven by their electrochemical gradients¹²³.

The membrane potential of a cardiomyocyte can be measured by the patch clamp technique. A typical human cardiac AP consists of 5 phases (Phase 0 to 4), with a total AP duration of more than 200 milliseconds¹²⁴. Phase 4, termed resting membrane potential (maximum diastolic potential, terminology specific for cardiomyocytes) describes the state when a cardiomyocyte is not stimulated. The absolute transmembrane voltage during phase 4 varies between -85 to -95 mV depending on recording conditions (temperature, cell culture medium, recording solution, etc.). The AP starts with phase 0, the depolarization phase, during which transmembrane potential rapidly rises towards positive values. The upstroke velocity, expressed as dV/dt_{max} , differs between working myocytes (ventricular and atrial myocytes) and pacemaker myocytes of the sinoatrial or atrioventricular node (nodal myocytes) (Fig 8). Nodal myocytes are characterized by a markedly slower upstroke velocity¹²⁵. Phase 1 is characterized by a small downward deflection or notch, while phase 2, the plateau phase, is particularly prominent in ventricular working myocardium. Phase 3 is characterized by a gradual repolarization towards the resting transmembrane potential of the following phase 4.

Different parts of the heart display distinct AP properties, which enable their functional specialization¹²⁶. The human heart consists of an excitatory and conduction system (sinoatrial (SA) node, atrioventricular (AV) node, His bundle and Purkinje fibers) that is characterized by the ability to initiate action potentials, and a contractile system consisting of cardiomyocytes that

generate contractile force and depend on depolarization of neighbouring cells to generate action potentials. In each heartbeat, action potentials are initiated in the part of the excitatory system with the fastest spontaneous rate of action potential initiation (normally the SA node) and then propagate across the atria and the specific conduction system to the ventricles. This orderly patterned action potential progression across the myocardium results in potential differences that can be recorded noninvasively from the body surface as the ECG. An ECG trace exhibits typical entities called the P wave, the QRS complex and the T wave, which represent atrial depolarization, ventricular depolarization, and ventricular repolarization, respectively. The ECG is one of the most important diagnostic methods for cardiac diseases and conveys enormous amounts of information regarding both structure and function of the heart.

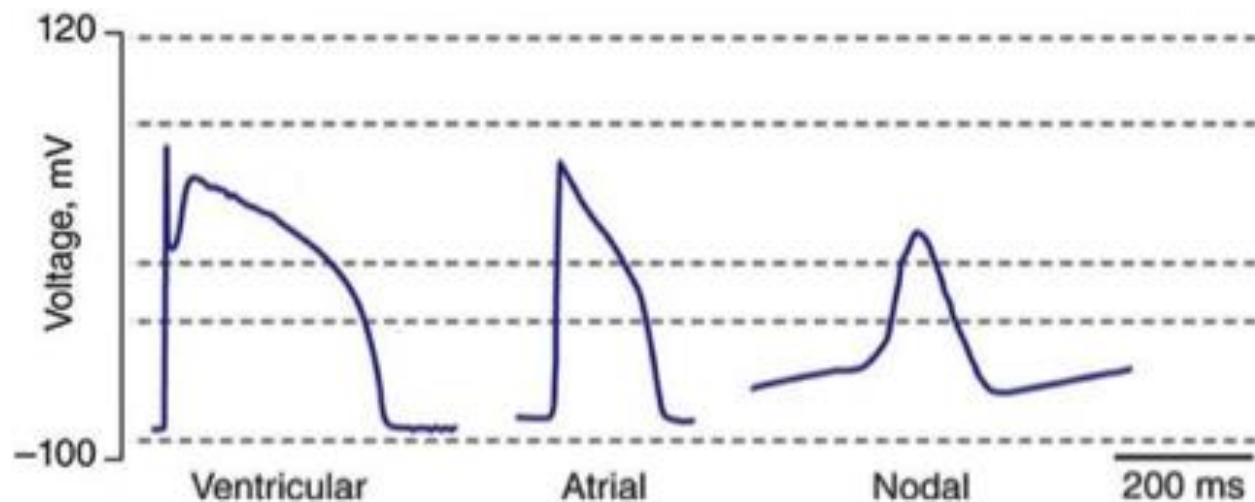


Figure 8: Cardiac action potential of ventricular, atrial and nodal myocytes. Action potential traces recorded in cells isolated from ventricular and atrial myocardium as well as sinoatrial node (as indicated). Figure was reproduced based on the website (<http://clinicalgate.com/heart-failure-pathophysiology-and-diagnosis/>).

For example, the interval from the beginning of the QRS complex until the end of the T wave (the so-called QT interval) reflects the time necessary from the first depolarization of ventricular cardiomyocytes until repolarization is finished in all ventricular myocytes. A prolonged QT interval, which indicates prolonged action potential durations at least in some regions of the myocardium, is associated with an increased risk of ventricular tachycardias and sudden cardiac death. Certain medications, as well as certain genetic variants, result in a prolonged QT interval, as in acquired and inherited LQT syndromes. Since 2005, both FDA and European regulators require a Thorough QT evaluation of every new drug as part of the safety pharmacology investigations. A prolonged action potential exposes a cell to the risk of

arrhythmias, such as early EADs. Rate and rhythm of heartbeats are also parameters for evaluation of cardiac function. The normal human heart rate varies from 60 to 100 beats per minute (bpm). Beating rates lower than 60 bpm are regarded as bradycardia, while beating rates higher than 100 bpm are considered tachycardia. Both can result from abnormalities in physiologic rhythm generation. Normal heart rhythm (sinus rhythm) is initiated in the SA node. Arrhythmias may result from impaired sinus node function or ectopic rhythm generation in other parts of the heart, as in atrial fibrillation or ventricular tachycardia.

Typical action potential characteristics distinguish three major subtypes of hiPSC-CMs

It is known that CMs derived from hiPSCs show immature and embryonic-like characteristics, including their electrophysiological properties. First of all, the resting membrane potential is less negative in hiPSC-CMs in comparison to adult CMs (-50–60 mV vs -85 mV)^{127–131}. Moreover, due to the more depolarized state of hiPSC-CMs, functional availability of Na⁺ channels is reduced¹³², which results in a slower upstroke of the AP^{128–131}, while low expression of Na⁺ channels (encoded by *SCN5A*) in young hiPSC-CMs might also contribute to this¹³³. Moreover, the I_{To1} current is inactivated at more positive membrane potentials, which leads to a less pronounced phase 1 repolarization¹³⁴, although similar channel expression and current density levels in hiPSC-CMs and adult CMs have been reported¹³⁴. The other two main repolarizing currents, I_{Kr} and I_{Ks} , are observed at similar levels in hiPSC-CMs and adult CMs^{129,33}. Two types of Ca²⁺ channels are present in the human heart: T-type and L-type channels. The presence of the T-type calcium current ($I_{Ca,T}$) is typical of fetal CMs¹³⁵, while atrial and ventricular CMs of the adult heart do not exhibit $I_{Ca,T}$, which is restricted to the conduction system¹³⁶. For hiPSC-CMs, the presence of $I_{Ca,T}$ has been debated: the current was not detected in one study¹²⁹, while in another, $I_{Ca,T}$ was reported in a subset of hiPSC-CMs¹³⁷. By contrast, $I_{Ca,L}$ was demonstrated to be present at similar densities in hiPSC-CMs and adult CMs, although exact values have been found varying among hiPSC-CMs^{129,128,138}.

Nevertheless, when action potentials were recorded by patch clamp measurements from single cardiomyocytes dissociated from beating cardiac EBs differentiated from hiPSCs, distinct subtypes of CMs with ventricular, atrial and nodal AP properties were obvious^{139,33}. According to the literature, hiPSC-derived ventricular myocytes display a marked plateau phase that results in the longest AP duration among the 3 subtypes (normally 380 to 450ms). Moreover, they have a fast upstroke velocity, a negative maximum diastolic voltage and a APD_{50}/APD_{90} ratio ranging from 1.1 to 1.3 (APD_{50} and APD_{90} represent the duration between AP starting point to 50 or 90%

of repolarization phase, respectively)³³. Atrial myocytes can be distinguished by a lack of plateau phase that causes a triangular shape of the AP trace and by exhibiting the shortest AP duration (usually 300 to 350ms)³³. A rapid upstroke velocity and a less negative maximum diastolic voltage are also detected in hiPSC-atrial myocytes. APD₅₀/APD₉₀ ratios of them range from 1.3 to 1.6. HiPSC-nodal myocytes are characterized by a slow upstroke velocity³³. These cells also exhibit a less negative maximum diastolic voltage, a lack of plateau phase, and AP durations around 350 to 380ms³³.

1.3.2.3 Current methods for action potential measurement

Conventional patch clamp electrophysiology

Accessing the cell membrane through conventional patch clamp electrophysiology is considered as the gold-standard for investigating ion channel activity. No other technique is able to provide more insight into the kinetics, gating properties, functionality and pharmacology of ion channels. However, the complexity, low throughput and labor-intensive characteristics of this approach allows one researcher to perform only 10–15 measurements a day, which is far from enough to meet the demands of academic and industrial labs. This has encouraged the development of various platforms for measurement of electrophysiology and/or calcium fluxes in a direct or indirect manner, which is also being applied to hiPSC-CMs.

Planar patch clamp electrophysiology

To overcome the low throughput of conventional patch clamp, several 'planar' patch clamp platforms have been developed, which can process parallel recordings from 16 to 384 cells. While these systems differ in their level of automation and technical specifications, they increase the throughput 10- to 100-fold depending on the platform used and the ion channel under investigation¹⁴⁰. They also make cellular electrophysiology accessible to more users by simplifying the process¹⁴¹. The available platforms including IonWorks Quattro¹⁴², Opatch¹⁴³, PatchXpress¹⁴⁴, Patchliner¹⁴⁵ and SynchroPatch¹⁴⁶, have been mainly applied for the analysis of recombinant cell lines overexpressing single ion channels. However, they are now being trailed for measurements on more complex systems such as hiPSC-CMs^{147,129}.

Multi-electrode arrays and nanopillars

The invasive nature of conventional and planar patch clamp allows only short-term (minutes to hours) recordings from single cells. However, some applications, such as acute and chronic

toxicity, might benefit from long-term recordings (days to weeks) of multi-cell clusters. Multi-electrode arrays (MEAs) are composed of glass slides photo-etched with micro-electrode arrays, which can record field potentials from cell clusters for hours to days. Most analysis with MEAs has been performed using low throughput single-well formats for recording from multi-cellular clusters of hiPSC-CMs in 2D monolayers or 3D structures, including evaluation of cardiotoxicity and drug effects in hiPSC-CMs carrying *KCNH2* (I_{Kr}) mutations associated with LQTS2¹⁴⁸. Moreover, new generations of 96-well MEAs equipped with electrical pacing are developed, satisfying the reduced plate cost, light transmission, improved level of user-friendly software interface and automated data analysis.

Recent technologies have allowed the merger of substrate-integrated extracellular MEAs with intracellular electrodes, which permits switching between extra- and intracellular recordings by employing vertical nanopillar electrodes allowing nano-scale electroporation and re-sealing events. Although such systems enable detecting action potential waves of hiPSC-CMs¹⁴⁹, the intracellular recordings limits their use for pharmaceutical screening on single cell level and probing the electrical alternation of subcellular organelles.

Optical recordings

The challenges in direct recordings of electrophysiology have inspired the development of optical action potential mapping using voltage-sensitive dyes (VSDs) (e.g. the ANEPPS dyes)¹⁵⁰ or genetically encoded voltage sensors or indicators (GEVIs)¹⁵¹. These techniques permit action potential detection in a high spatial and temporal resolution, and are amenable to scalable recordings. The raw fluorescence data can be rapidly obtained simultaneously from several cells in a single field of view of the microscope, enabling the analysis of over 440 single hESC-CMs per day¹⁵².

However, VSDs are inherently phototoxic, which can cause temporal degradation of samples and varying signal quality over time¹⁵¹. This can be overcome by the introduction of genetically encoded voltage sensors, like ArcLight¹⁵², which has been recently used to image action potentials from healthy and diseased hiPSC-CM¹⁵². In this study, ArcLight enabled the accurate evaluation of drug-induced arrhythmic effects in hiPSC-CMs, which was comparable to patch clamp recordings¹⁵². Unlike VSDs, GEVIs also provide homogenous signal intensities independent of cell uptake¹⁵². Even more importantly, it is theoretically possible to express them in specific cell populations using cell type-specific promoters. Furthermore, the nature of

genetically encoded sensors allows carrying out sequential measurements, permitting each cell to be used as its own control, overcoming the inherent heterogeneity of hPSC-CMs preparations.

1.3.2.4 Optical action potential measurement with genetically encoded voltage sensors

Engineering genetically encoded fluorescence sensor

Genetically encoded fluorescent sensors have been invented to image a range of intracellular events including the concentration of many chemicals, membrane potential, pH, enzyme activities, and others^{153–155}. As protein-based sensors, they are easily targeted to subcellular locations by appending a localization tag. Their use is less invasive in comparison to other interrogation techniques such as patch clamping and microinjection, since their expression simply requires delivery of their encoding DNA into target cells. The reporting domains of these sensors typically employ Green Fluorescent Protein (GFP) or its genetic variants. Genetically encoded fluorescent sensors can be categorized into two types: those that display the fluorescence intensity of a single FP and those that visualize changes in Förster Resonance Energy Transfer (FRET) between a donor and an acceptor FP.

The single FP sensors rely on the exposure of the FP chromophore to the cellular condition such pH¹⁵⁶ and redox state¹⁵⁷, which has a large influence on its fluorescent properties. With the invention of circularly permuted GFP, it allows to engraft protein domains onto β -barrel of the GFP¹⁵⁸, resulting in that solvent-induced conformation changes of the engraft directly trigger changes in the chromophore's properties. For instance, calmodulin and M13, which show a Ca^{2+} -dependent interaction, were fused to the N- and C-termini of circularly permuted GFP, respectively, to generate the GCaMP probe¹⁵⁹, whose fluorescence is quenched in absence of Ca^{2+} . Other useful single FP sensors developed include the membrane potential sensor ArcLight^{160,161}, the dual pH and Cl^- sensor ClopHensorN¹⁶², the H_2O_2 sensor HyPer¹⁶³, the glutamate sensor iGluSnFR¹⁶⁴ and the ATP to ADP ratio sensor Percival^{165,166}. Most of single FP-based sensors are intensimetric, which makes them susceptible to fluctuations in sensor concentration as well as cell movement artifacts. However, a few ratiometric single FP-based sensors have been developed, which change their relative excitation at two different wavelengths as a function response of ligand concentration^{167,168}. For the single FP sensors, the necessity for allosteric coupling of ligand binding to modulate the chromophore microenvironment posts a series of sensor engineering challenges. Nevertheless, several single FP sensors have shown excellent signal to noise ratios^{169,164}.

FRET-based sensors consist of two FP domains flanking a recognition domain, forming a single polypeptide chain. Ligand-induced conformation change of the recognition domain results in a relative orientation change of the FP-FP geometry, and thus changes of the FRET efficiency. FRET is defined as radiationless energy transfer between two chromophores derived from long-range dipole-dipole interactions¹⁷⁰. It takes place between two chromophores when two conditions are satisfied: 1) the emission wavelength of one chromophore (donor chromophore) overlap with the excitation wavelength of the other chromophore (acceptor chromophore), 2) the distance between the donor and acceptor chromophore ranges from 1 to 10nm. When both chromophores are fluorescent, FRET also manifests as fluorescence resonance energy transfer. By absorbing external light, a donor chromophore adopts an electronic excited state with higher energy that may be transferred in a radiationless way to the neighboring acceptor chromophore, which may then exhibit fluorescence. The efficiency of FRET is inverse proportional to the sixth power of the donor-acceptor distance. Therefore, FRET activity is highly sensitive to even a small shift in distance. Moreover, changes in the spatial orientation of the two fluorochromes result in changes of FRET efficiency.

GFP, which was discovered in the jellyfish *Aequorea victoria* in the 1960s, emits green fluorescence when excited by ultraviolet to blue light. In the past decades, several genetic variants (YFP, CFP, RFP, Clover, mRuby2 and others) with distinct spectral properties and other advantages (such as lack of dimerization, faster maturation, mammalian-optimized codon usage) were engineered since then¹⁷¹. Genetically encoded FRET pairs are constructed by connecting encoding fragments of two selected fluorescent variants that match the requirement of FRET mechanism. For example, excitation and emission peak wavelength of Clover are 505 nm and 515 nm respectively, which makes it a well-suited FRET pair with mRuby2, with excitation and emission peaks at 559 nm and 600 nm¹⁷².

A variety of genetically encoded reporters or sensors harness changes in FRET signal to report biochemical processes in living cells. Cameleon, a FRET sensor for Ca^{2+} , was one of the first sensors to be developed using the principle of FRET. This construct consists of a single polypeptide including orderly ECFP, calmodulin (CaM), M13 and EYFP. Binding of Ca^{2+} to CaM increases the affinity of M13 to CaM, resulting in the wrapping of the M13 around CaM and the relative geometry change of the FPs, which leads to an increase in FRET¹⁷³. As Cameleon gave rise to ratiometric emission signal, the measurements were not disturbed by fluctuations in sensor concentration, excitation intensity, and optical path length¹⁷³.

Many FRET sensors have been developed following similar principles as this prototype. However, despite the seemingly modular design, constructing a FRET sensor still involves trial-and-error-based, stepwise improvements. The engineering for FRET sensor can be laborious and time-consuming, which includes the process of screening the optimal FP pair, targets binding domain as well as linker peptides and improving the FRET sensor by repeating expression, purification and analysis. A more efficient method may be to simultaneously screen a large number of variants in proper cell culture for ratiometric response to ligand addition. This has been accomplished now by several innovative and high-throughput strategies, such as reverse transfection of mammalian cells over spotted sensor DNA¹⁷⁴, translocation of sensors to the periplasmic space of bacteria for easier ligand delivery¹⁶⁸ and using engineered cell lines with existing targets¹⁶⁹. In addition, semi-synthetic FRET sensors, based on a distinct mechanism that employs a natural protein domain coupled to small molecule dyes, have also been constructed. Indeed, technologies such as SNAP-tag¹⁷⁵ and FIAsh¹⁷⁶ have enabled site-specific incorporation of synthetic dyes into natural protein domains to achieve a sensor function. This strategy not only allows more sensors to be developed^{177,178}, but also permits monitoring of changes in protein conformation accurately¹⁷⁹.

Genetically encoded voltage sensors and FRET-based voltage-sensitive fluorescent protein

Over the last 15 years, genetically encoded optical voltage sensors have been considerably developed^{180–182}. Initial design strategies exploited voltage-dependent conformational changes of voltage-gated ion channels (FlaSh¹⁸³, SPARC¹⁸⁴) or isolated voltage sensor domains of those channels (VSFP1, voltage-sensitive proteins)¹⁸⁵, which results in modulation of fluorescence intensity of the fused reporter protein. For instance, in VSFP1, the voltage-sensing domain was the fourth transmembrane helix of the potassium channel Kv2.1. These first-generation sensors were reported to image changes of membrane potential, while their application in mammalian settings was unfortunately limited by their poor membrane targeting of transfected cells¹⁸⁵.

More recently, the second generation of voltage sensors (VSFP2s) were developed by replacing the sensing protein in VSFP1¹⁸⁵ with the voltage-sensing domain of voltage sensitive phosphatase (Ci-VSP) from *Ciona intestinalis*, resulting in sensors with increased plasma membrane targeting and more reliable responsiveness to membrane potential changes in living mice, brain slices and isolated cells^{186,187}. This VSD is a homologue of the voltage-sensing domain of voltage-gated potassium channels and, upon expression in mammalian cells, integrates into the plasma membrane as a monomer without forming a channel pore. Lately, a series of monochromatic fluorescent sensors (termed VSFP3s) with spectral variants ranging

from the cyan to the far-red region of the visible light spectrum were constructed^{188,189}. VSFP2s exploited the FRET reporting mechanism for voltage alteration induced by protein conformational rearrangements, whereas VSFP3s rely on a modulation in the fluorescence intensity of a single fluorescent protein, a mechanism that is only partially understood. VSFP3s have the advantages of a broad choice of the color spectrum and fast responsive kinetics, but with smaller signal amplitudes in comparison with VSFP2s. Despite these limitations, VSFP3s were the first sensors to image spontaneous electrical activities in neuronal cultures¹⁸⁹. Finally, two other strategies of VSFP3 design were explored: one that uses circularly permuted fluorescent proteins, albeit with small responsive fluorescence changes¹⁹⁰, and the other one in which the voltage sensing domain is sandwiched between a FRET pair (named VSFP “Butterflies”)¹⁹¹. The rationale underlying the second design was to combine both larger dynamic range of VSFP2s and the rapid kinetics of VSFP3s. The classic genetically encoded FRET pair consists of CFPs and YFPs, but many CFP/YFP reporters suffer from low FRET dynamic range, phototoxicity from the CFP excitation light and complex photokinetic events such as reversible photobleaching and photoconversion. In a recent report, Clover and mRuby2, which are the brightest green and red fluorescent proteins to date and have the highest Förster radius of any ratiometric FRET pair yet described, were employed to construct a VSFP2 (termed VSFP-CR). Replacement of CFP and YFP with these two proteins markedly improved photostability, FRET dynamic range, and emission ratio changes, resulting in an improved responsiveness to fast transmembrane voltage changes in neuronal cultures.

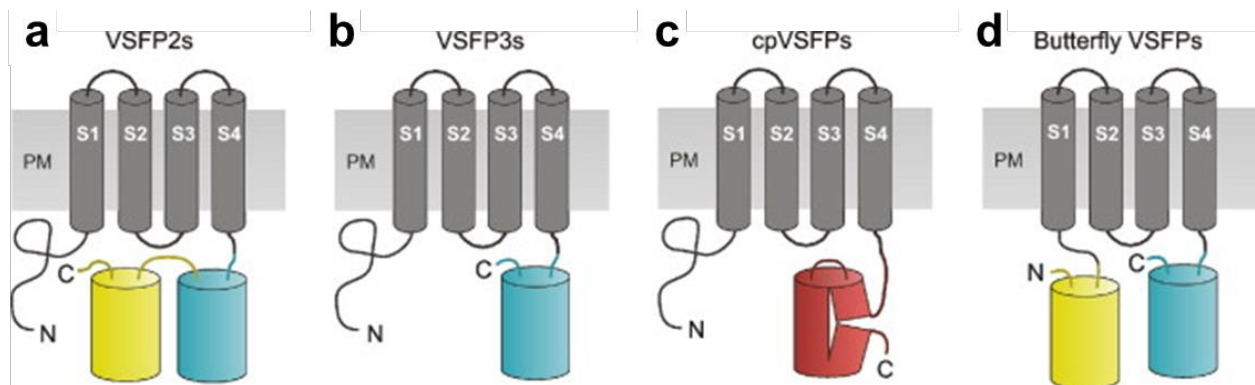


Figure 9: Scheme of VSFP probes engineered by combining fluorescent proteins (single FPs or FRET pairs) with the fourth transmembrane segment (S4) of the voltage-sensing domain of Ci-VSP. (a) VSFP2s are FRET-based voltage sensors consisting of an acceptor (Citrine) and donor (Cerulean) fluorophore. (b) VSFP3s contains a single FP. (c) cpVSFPs contain a circularly-permuted fluorescent protein (mKate). (d) In the Butterfly VSFPs, the voltage-sensing domain of Ci-VSP is sandwiched between a fluorescent FRET pair. PM: plasma membrane. Figure is adapted from¹⁹².

1.4 Aims of the studies

1.4.1 Exploring the mechanism of truncating titin-based DCM and its therapy using patient specific iPSC-CMs

We aimed at establishing an iPSC-based human model of DCM caused by a truncating *TTN* mutation and at investigating the suitability of this model to investigate therapeutic approaches employing AON-based exon skipping. Previous work from our collaborator's group had identified the first human *TTN* mutation as molecular basis for DCM in a large Australian family¹⁹³. A 2-bp insertion located at exon 326 (c.43628insAT, p.Ser14450fsX4) causes a frame shift leading to a premature stop codon resulting in expression of a truncated protein¹⁹³. Knock-in of this mutation in the mouse *Ttn* gene caused embryonic lethality in homozygous animals due to the defective myofibril development, while heterozygous mice were viable but developed a DCM phenotype when exposed to cardiac stress¹⁹⁴.

We aimed at generating patient-specific iPSCs from an affected member of the Australian DCM family and to characterize the DCM phenotype in the patient-specific iPSC-CMs. Moreover, we aimed at reframing the titin transcripts by an AON-mediated exon skipping approach and to evaluate whether this strategy can reverse the DCM phenotype in the patient-specific iPSC-CMs.

1.4.2 Establishing cardiac subtype specific optical AP recordings in hiPSC-CMs

We aimed at establishing a system allowing optical action potential recordings from hiPSC-CMs in a subtype-specific manner. First, we aimed at establishing optical action potential recordings from hiPSC-CMs using VSFP-CR expressed by a lentiviral system. To add subtype-specificity to our assay, we aimed at identifying promoter elements that specifically drive expression in nodal, atrial, and ventricular hiPSC-CMs. Using these promoter elements, expression constructs should be generated allowing a subtype-specific expression of VSFP-CR in the above-mentioned iPSC-CM subtypes.

We aimed at validating the system of subtype-specific AP measurements in a patient-specific disease model of LQT1. Furthermore, we aimed at investigating whether this system allows repeated AP recordings in the same cells over extended time periods and whether it can be used to investigate subtype-specific drug effects.

Part 2 Materials and Methods

2.1 Individuals involved in the study and cell lines

For the generation of diseased TTN hiPSCs and control CTR1 hiPSCs, we recruited a 62-year-old female patient carrying a TTN truncating mutation, who was a member of the DCM family described previously⁷⁸, and an unrelated gender- and age-matched healthy volunteer without a history of cardiac disease or cardiovascular risk factors. The patient's primary skin fibroblasts (PSFs) were obtained from her skin biopsy at the Royal Brisbane and Women's Hospital, Brisbane, Australia, while the control PSFs were harvested from the donor's skin biopsy at the Klinikum rechts der Isar, Technical University of Munich. Dermal biopsies were minced into 2 mm pieces, plated on petri dishes, and cultured in Quantum 333 medium (PAA). Cells migrating out of the biopsies were passaged in DMEM containing 10% FBS. The PSFs at passage 3 were used for generation of corresponding hiPSC lines by Sendai virus-mediated reprogramming (see below).

The generation of the LQT1 patient line (LQT1 hiPSCs) from an individual suffering from long-QT syndrome type 1 caused by a R190Q missense mutation of the *KCNQ1* gene and the unrelated control line (CTR2 hiPSCs) have been described previously³³. Both LQT1 hiPSCs and CTR2 hiPSCs were produced by retrovirus-mediated reprogramming of dermal fibroblasts. An isogenic control line (LQT^{corr} hiPSCs) of LQT1 hiPSCs was generated by one of our collaborators (Milena Bellin, Leiden, The Netherlands) by homologous recombination to correct the single nucleotide heterozygous c.569G>A *KCNQ1* mutation in LQT1^{R190Q} hiPSCs. Briefly, a targeting vector containing a long homology arm including the wild type G nucleotide and a short homology arm, separated by a loxP-flanked Neomycin resistance (*NeoR*) cassette, was constructed (Fig 30a). The construct was electroporated into hiPSCs and screening of targeted cells was performed by PCR over the short homology arm (Fig 30b, left). Among the targeted clones, the corrected ones were identified by PCR followed by Sanger sequencing (Fig 30b, right). The *NeoR* cassette was then excised by Cre recombinase overexpression. FACS single-cell deposition was used to clonally isolate the LQT1 corrected hiPSC clone (LQT1^{corr}), which showed wild-type *KCNQ1* sequence (Fig 30c) and maintained a normal karyotype (Fig 30d).

Two additional unrelated control lines (CTR3 and CTR4 hiPSCs) were reprogrammed from dermal fibroblasts and keratinocytes, respectively, by retrovirus-mediated expression of the

reprogramming factors. All the cell lines were tested to be free of mycoplasma contamination before performing experiments.

Both studies followed a human research subject guideline approved by the Ethic Committee and Institutional Review Board of the Klinikum Rechts der Isar, Technical University of Munich. Written agreement was obtained from all cell donors and experiments were conducted according to the principles described in the WMA Declaration of Helsinki and the Belmont Report of the National Commission for the Protection of Human Subjects of Biomedical and Behavioral Research.

2.2 HiPSC generation and characterization

For iPSC generation, CTR1 control and DCM patient PSF (passage 3) were infected with Sendai viruses encoding c-MYC, OCT4, SOX2, and KLF4 (3 MOI each, Life Technologies), trypsinized after 4 days of infection and seeded on irradiated mouse embryonic fibroblasts (MEFs) in hESC culture medium (DMEM/F12 supplemented with 20% knockout serum replacement (KSR, Invitrogen), 2mM L-glutamine, 0.1mM nonessential amino acids, 0.1mM β -mercaptoethanol, 50U/ml penicillin, 50mg/ml streptomycin and 10ng/ml human b-FGF 6 (R&D))³³. After reprogramming, hiPSCs were grown on matrigel (BD) in MEF-conditioned hESC culture medium and enzymatically passaged by applying 1 mg/ml dispase (Stem Cell Technologies). Karyotypes of the hiPSC lines were tested at the Institute of Human Genetics of the Technical University of Munich. The presence or absence of the TTN-c.43628insAT mutation was confirmed in DCM patient and CTR1 control PSFs and hiPSCs, respectively, by Sanger sequencing using 50 ng of genomic DNA isolated by Genomic DNA Purification Kit (Genra Systems). Pluripotency was assessed by both immunostaining for pluripotency markers (NANOG and TRA1-81) and quantitative real-time PCR (qRT-PCR) of reactivated endogenous pluripotency genes (*NANOG*, *OCT3/4*, *REX1*, *SOX2* and *CRIPTO1/TDGF1*). Primer sequences are listed in Supplementary Table 3. The iPSCs were further characterized by a bioinformatics assay for pluripotency (PluriTest) based on global functional genomic data. For this purpose, RNA was isolated from undifferentiated hiPSC, amplified with the Illumina TotalPrep RNA Amplification Kit (Life Technologies) and hybridized to the Human HT-12 v4 Expression BeadChip Kit (Illumina). Raw microarray data were analysed using the online PluriTest algorithm (<http://www.pluritest.org>)²⁵. For the quantification of the DNA methylation levels of pluripotency-associated genes (*RAB25*, *NANOG*, *PTPN6*, *MGMT*, *GBP3*, and *LYST*), genomic

DNA was harvested from CTR1 control and DCM patient PSFs and iPSCs and the DNA methylation level was evaluated by qRT-PCR with the OneStep qMethyl Human Pluripotent Stem Cell Panel (Zymo Research) according to the manufacturer's protocols.

2.3 HiPSC differentiation to the cardiac lineage

2.3.1 Differentiation of hiPSC in EBs and Monolayers

The hiPSCs were cultured and differentiated into CMs using either the EB protocol or a chemically-defined monolayer method depending on the experimental requirements^{17,149}. For the EB differentiation method, hiPSCs were differentiated as EBs by detaching iPSC colonies with dispase and culturing them in low-attachment plates coated with 5% (w/vol) poly-HEMA (Sigma-Aldrich) for 3 days in MEF-conditioned hESC medium. For inducing spontaneous differentiation, medium was then exchanged with EB20 (DMEM/F12 supplemented with 20% FBS, 0.1mM nonessential amino acids, 2mM L-glutamine, 50U/ml penicillin, 50mg/ml streptomycin and 0.1mM β -mercaptoethanol). To improve cardiac differentiation, 50mg/ml ascorbic acid was added to the EB20 medium and floating EBs were seeded on gelatin-coated dishes at day 7 after differentiation for better detection of beating foci. At day 21-23 of EB differentiation, contracting areas were micro-dissected manually and plated on fibronectin-coated plates. These myocytic explants were maintained in EB2 medium (DMEM/F12 supplemented with 20% FBS, 0.1mM nonessential amino acids, 2mM L-glutamine, 50U/ml penicillin, 50mg/ml streptomycin and 0.1mM β -mercaptoethanol). For monolayer differentiation, single hiPSCs were passaged every three to four days with 0.5 mM EDTA and routinely maintained in E8 medium on Matrigel (9 $\mu\text{g}/\text{cm}^2$) supplemented with 10 μm rock inhibitor Y-27632 (Sigma-Aldrich) for the first 24 hours after passaging. For differentiation, 0.3 million cells were seeded in a 3.5cm diameter petri dish until 90-100% confluence was reached. Then, hiPSCs were coaxed to the cardiac lineage by CDM3 (RPM1 1640 medium containing 500 $\mu\text{g}/\text{ml}$ human albumin and 213 $\mu\text{g}/\text{ml}$ L-Ascorbic Acid 2 Phosphate) supplemented with 6 μM CHIR99021 at day 0 of differentiation and 2 μM Wnt-C59 (Fi 29) at day 2. Around day 8 to 10 of differentiation, monolayers of beating cardiomyocytes formed, which were kept in culture until day 16 when mechanical explanting was performed and the beating regions were transferred to fibronectin-coated plates using EB2 for long-term preservation and maturation. Before conducting experiments, all the cell lines were tested to be free of mycoplasma contamination.

2.3.2 Single cell dissociation and drug treatment of hiPSC-CMs

For single-cell analysis, three-month-old myocytic explants were dissociated with 4-6 rounds of 30 min incubation with 480U/ml collagenase type II (Worthington) under 850 r/min of shaking at 37 °C. Dissociated cells were reseeded on fibronectin-coated plastic plates or glass bottom microwell dishes (35/14mm, MatTek) for AP imaging, and maintained in EB2. Virus infection was conducted at day 2 after dissociation and experiments were performed at day 9-12.

For chronic isoproterenol treatment, 10 μ M Isoproterenol (ISO, Sigma-Aldrich) was added to EB2 every time medium was changed. Medium was refreshed every other day and cells were processed for molecular and immunocytochemical analyses after one week of ISO administration. Both 100 nm cisapride (Sigma-Aldrich) and 9 μ m Ivabradine (Sigma-Aldrich) were applied for 10 min to the single CMs in the EB2 medium and AP imaging was conducted both before and after drug treatment.

2.4 Transfection of 2OMePS-AON to HL-1 cells and hiPSC-CM

Transfection of 2OMePS-AONs (200 nM) into single HL-1 and hiPSC-CMs was carried out using the PEI (Fermentas) and the TransIT-LT1 (Mirus) transfection reagents, respectively, following the manufacturer's protocols. Successful skipping of titin exon 326 was confirmed by reverse transcription PCR (RT-PCR) and Sanger sequencing as described in section 2.8.

2.5 Virus generation and hiPSC-CM infection

2.5.1 Generation of the U7snRNA lentiviral vectors encoding AONs

To generate the lentiviral construct, we used a previously described lentiviral plasmid that encodes a AON designed to target exon 51 of the dystrophin gene embedded in a modified U7 small nuclear RNA sequence¹⁹⁵. Using PCR mutagenesis, we exchanged the AON sequence targeting exon 51 with antisense sequences specifically annealing to two Exonic Splicing Enhancer regions in exon 326 of human TTN to create U7snRNA-*TTNAONs*-IRES-GFP vector. As negative controls, scrambled sequences corresponding to the human and mouse titin AONs were also replaced by PCR mutagenesis, resulting in the constructs U7snRNA-*ScrAONs*-IRES-GFP. The two modified U7snRNA fragments were separately cloned into the lentiviral transfer plasmid pRRLsin18.PPT.PGK.IRES.GFP. Primers used for generating the lentiviral constructs are listed in the Supplementary Table 3.

Lentiviruses were produced by cotransfection of the VGV.G envelope plasmid, the pCMV delta R8.74 packaging plasmid and one of the U7snRNA-AONs-IRES-GFP lentiviral transferring plasmids into HEK293T cells using FuGENE HD (Promega). Virus-containing supernatants were harvested after 48 h of incubation, filtered through a low-protein-binding cellulose acetate filter (0.45 μm) and used directly to infect dissociated hiPSC-CMs in the presence of 8 $\mu\text{g}/\text{ml}$ polybrene. Infected cells were harvested either after 1 day of infection for detecting the skipping of TTN exon 326 by RT-PCR and sequencing analyses or after 5 days for immunofluorescence and qRT-PCR analysis.

2.5.2 VSFP-encoding lentivirus constructs

A plasmid (pcDNA3.1/Puro-CAG-VSFP-CR) containing the membrane voltage sensor VSFP-CR was obtained from Addgene (plasmid #40257)¹⁷². All voltage sensor constructs (PGK-VSFP, MLC2v-VSFP, SLN-VSFP and SHOX2-VSFP) were generated using a second-generation lentiviral system. The VSFP-coding sequence was first subcloned into the lentiviral transfer plasmid pRRL.sin18.PPT.PGK.MCS to generate the plasmid pRRL.sin18.PPT.PGK-VSFP. Subsequently, the PGK promoter was exchanged either with the *hMLC2v* enhancer¹⁹⁶ or a SLN-promoter fragment (-3.529kb upstream to the transcriptional starting site) or a SHOX2-promoter element (-3.461kb upstream to the transcriptional starting site). To generate lentivirus, the viral expression constructs were co-transfected with the envelope-encoding plasmid pMD2.VSVG and the packaging plasmid pCMV Δ R8.74 into HEK293T cells using Fugene HD (Promega). Virus particles were harvested by collecting the culture medium after 72 hours of incubation at 37 °C at 5% CO₂ and centrifugation at 296 \times g for 15 min.

HiPSC-CMs were infected at day 2 after dissociation. Virus-containing supernatant was added in a 1:1 ratio to CM culture medium (DMEM/F12 supplemented with 2% FBS, 2 mM L-glutamine, 0.1 mM nonessential amino acids, 0.1 mM β -mercaptoethanol, 50 U/ml penicillin, and 50 $\mu\text{g}/\text{ml}$ streptomycin) containing 8 $\mu\text{g}/\text{ml}$ polybrene. Medium was exchanged after 24 hours. Imaging was performed at 7 days after infection.

2.5.3 Generation of AAVs encoding WT KCNQ1 and LacZ

To generate AAV6 virus encoding wt *KCNQ1*-HA, the HA sequence (TACCCATACGATGTTCCAGATTACGCT) was added to the N terminus of a *KCNQ1* expression plasmid described previously³³ by PCR. The PCR products were subcloned into the

multiple cloning site of pAAV_CMV_GOI plasmid. The plasmids pAAV_CMV_KCNQ1_HA, AAV2/6 (providing Rep2/Cap6) and delta-F6 were co-transfected into HEK293T cells using PEI reagent. Cells were harvested 3 days post transfection and pelleted with $462 \times g$ at $4^\circ C$ for 10 min. After one round of freeze-thaw, the cell pellet was resuspended in a 20 mM Tris buffer (with 1 mM $MgCl_2$) and disrupted by sonication (3 x 30 sec, output 5 at 30%). Upon benzonase and deoxycholic acid treatment, the cell lysate was centrifuged at $3291 \times g$ at $4^\circ C$ for 15 min. After 3 rounds of CsCl gradient ultracentrifugation, fractions were collected based on refractive index measurements, and buffer exchange to PBS was performed using centrifugal filter units (Amicon Ultra-15, Millipore). Titration of genome copies (cg) was done by qPCR. For AAV6 infection, virus was directly added to culture medium at a concentration of 1×10^6 gc/cell and medium was changed 24 hours post infection.

2.6 Live-cell imaging of sarcomere dynamics in hiPSC-CM

CTR1 myocytic explants were dissociated, seeded on fibronectin-coated 384-well plates and infected with the CellLight® Actin-RFP baculovirus (Life Technologies, 10 MOI) two days after seeding. The medium was exchanged after 24 hours and then every other day. The live imaging was performed using a DMI6000-AF6000 Leica epifluorescence microscope. The same cells were imaged every day for two weeks. Images are presented with a pseudo-colour scale.

2.7 Mass Spectrometry sample preparation and data processing

HiPSC-CMs were resuspended in a lysis buffer containing 6M guanidinium chloride and alkylated prior to overnight digestion with Trypsin and LysC as previously described¹⁹⁷. Mass spectrometry (MS) experiments were performed with technical triplicates on a nanoflow HPLC system (Proxeon/Thermo Fisher Scientific) coupled via a nanoelectrospray ion source (Thermo Fischer Scientific) to a Q Exactive mass spectrometer (Thermo Fisher Scientific)¹⁹⁸, which was performed by our collaborator (Dr. Marta Murgia, Max Planck Institute of Biochemistry). Raw MS data were processed with MaxQuant software (version. 1.4.3.19, <http://www.maxquant.org>)¹⁹⁹. Peak list files were searched by the Andromeda search engine incorporated into the MaxQuant framework²⁰⁰ against the UniProt database containing forward and reverse sequences. The 'match between runs' option in MaxQuant enabled matching peptide identifications across different replicates in a time window of two minutes. Processed data were uploaded into the MaxQB database²⁰¹ and identified titin peptides were matched to the sequence of human

isoform Q8WZ42 (34350 amino acids). 298 peptides were annotated as mapping to the exon 326 in human samples (corresponding to amino acids 21598-27300). All peptides matching the downstream of the exon 326 were annotated as C-terminal. Bioinformatic analysis was conducted with the Perseus software (www.perseusframework.org). Before hierarchical clustering, peptide intensity was logarithmized and normalized by subtracting the median value. Data were filtered for at least 50% valid values.

2.8 Reverse transcription PCR, quantitative real-time PCR and direct sequencing

Total mRNA of PSFs, iPSCs, EBs, and cardiomyocytes was isolated using the Stratagene Absolutely RNA kit, and 1 µg of mRNA was used to synthesize cDNA with the High-Capacity cDNA Reverse Transcription kit (Applied Biosystems). Gene expression levels were evaluated by quantitative real-time PCR (qRT-PCR) using 1 µl of the reverse transcription reaction, target-specific primers and the Power SYBR Green PCR Master Mix (Applied Biosystems). Gene expression was normalized to *GAPDH*. For confirming successful skipping of Titin exon 326, 1 µg of total mRNA was used for cDNA synthesis (Transcriptor first strand cDNA synthesis kit, Roche Applied Science) with a specific reverse primer for titin exon 328 (ex238r). A nested PCR was performed with two external (ex324f and ex328r) and four internal primers (ex325f and ex326r for amplification of the unskipped allele, and ex325f and ex327r for detection of the skipped allele) employing the Expand Long Template PCR System (Roche Applied Science). Sanger sequencing of the transition zones between exon 325 and 326 was performed with primer ex325f for the human TTN gene at Eurofins MWG Operon (Munich, Germany). Primer sequences are listed in Supplementary Table 2.

For single cell expression analysis, the cells were sucked into the patch pipette performing whole-cell patch clamp experiments and total RNA was isolated. cDNA was synthesized using High-Capacity cDNA Reverse Transcription Kit (Applied Biosystems). For the qRT-PCR analysis, 1 µl of cDNA of the RT reaction together with the Power SYBR Green PCR Master Mix (Applied Biosystems) were used for the subsequent qPCR. Primer sequences are provided in Supplementary Table 3. qRT-PCR products were visualized after electrophoresis on 2% agarose gels.

2.9 Immunocytological and alkaline phosphatase activity analysis

For immunofluorescence analyses, CMs were fixed with 4% paraformaldehyde and subjected to specific immunostaining using the following primary antibodies: TRA1-81-Alexa-Fluor-488-conjugated (BD Pharmingen), human Nanog (Abcam), α -actinin (Sigma-Aldrich), cardiac troponin T (Lab Vision), Z-disc Titin (kindly provided by Prof. Labeit), SRF (Santa Cruz), MURF2 (kindly provided by Prof. Labeit), Nbr1 (Cell Signaling), SQSTM1/p62 (Cell signalling), hMLC2v, hMLC2a, HCN4, SHOX2 (1:500, Abcam), SLN (1:100, Santa Cruz Biotechnology), Podoplanin (1:200, Abcam), NKX2.5 (1:100, Santa Cruz Biotechnology), HA tag (1:200, Abcam), β -Gal (1:500, Abcam). Phalloidin-AlexaFluor-594-conjugate (1:100; Life Technologies) was used to stain F-actin. AlexaFluor-488-, AlexaFluor-594-, AlexaFluor-647- (1:500; Life Technologies) secondary antibodies specific to the appropriate species were used. Nuclear DNA was stained by Hoechst 33258 dye (1:500; Sigma-Aldrich). Alkaline phosphatase activity was evaluated using the NBT/BCIP alkaline phosphatase blue substrate (Roche), following the manufacturer's guidelines. Images were captured using a DMI6000-AF6000 Leica epifluorescence microscope. Cell morphology was assessed by investigators blinded to the genotype.

2.10 Optical membrane potential measurements

CMs on glass bottom microwell dishes were imaged in a Tyrode solution consisting of 135 mM NaCl, 5.4 mM KCl, 1 mM MgCl₂, 10 mM glucose, 1.8 mM CaCl₂ and 10 mM HEPES, pH 7.35. Imaging of the VSFP-CR-expressing cells was performed with an oil immersion 40x objective of a TE2000 microscope (NIKON, Germany). VSFP-CR was excited at 480 nm and the emitted fluorescence was separated into GFP and RFP channels using an image splitter (OptoSplit II, Cairn Research, UK) equipped with CAIRN HQ535.50 566DCXR E570LP filters, projecting GFP and RFP fluorescence onto separate regions of the chip of an sCMOS camera (Flash 4, Hamamatsu, Japan). For high-speed imaging at 500 Hz, acquisition was performed with an image size of 512x88 pixels for a total duration of 8 s. The entire experiment was controlled with FEI LifeAcquisition 2.4.1.1.9 software (FEI, Germany). CMs were stimulated at 1Hz with locally-placed platinum wires (distance: 500 μ m, alternating electrical pulses, duration 5 ms, amplitude 5 V). At the end of each experiment, a 8 s background time series was acquired on parts of the glass bottom microwell dishes containing no cells. All experiments were performed at 35°C. In a typical recording session, signals from more than 100 cells could be recorded within two hours.

Image analysis was performed post-hoc using custom-written macros in ImageJ (National Institutes of Health, Bethesda, Maryland, USA), Matlab (version 2014-a, MathWorks, USA), and R (R Foundation for Statistical Computing, Vienna, Austria). Raw fluorescence over time traces were obtained from manually-chosen region of interests (ROIs) and background corrected fluorescence ratios (red channel over green channel) were calculated to obtain a membrane potential signal. The resulting signals were denoised by utilizing a generalized cross valuation based algorithm with a fixed smoothness parameter $s = 2.0$.

The beginning of each AP was manually identified. To correct for signal rundown due to uneven photobleaching of the two fluorescent proteins, a polynome was fitted to the baseline fluorescence values preceding each AP and the resulting baseline function was subtracted from the membrane potential signal.

For calculation of AP durations at 50% and 90% of repolarization (APD_{50} and APD_{90}), six to twelve subsequent APs were normalized to the maximum depolarization and averaged. APD_{50} and APD_{90} were calculated as the time intervals ranging from the beginning of the AP until the time point at which the signal had returned to 50% or 10% of the AP amplitude (Fig 21).

2.11 Statistics

Statistical calculations were performed with SPSS Statistics 22.0 (IBM SPSS, Inc.). Data are presented as means and standard error or 95% confidence intervals as indicated. When not otherwise specified, error bars indicate standard deviations. Differences between groups were analysed using Wilcoxon's signed ranks test for paired and Mann-Whitney's U test for unpaired comparisons. Continuous variables in distinct groups were compared either with Student's t-test when they passed evaluation for normality and equal variance, or otherwise by nonparametric Mann-Whitney U-test. Categorical data were evaluated with Fisher's exact test or chi-squared test. Two-tailed P-values less than 0.05 were considered statistically significant.

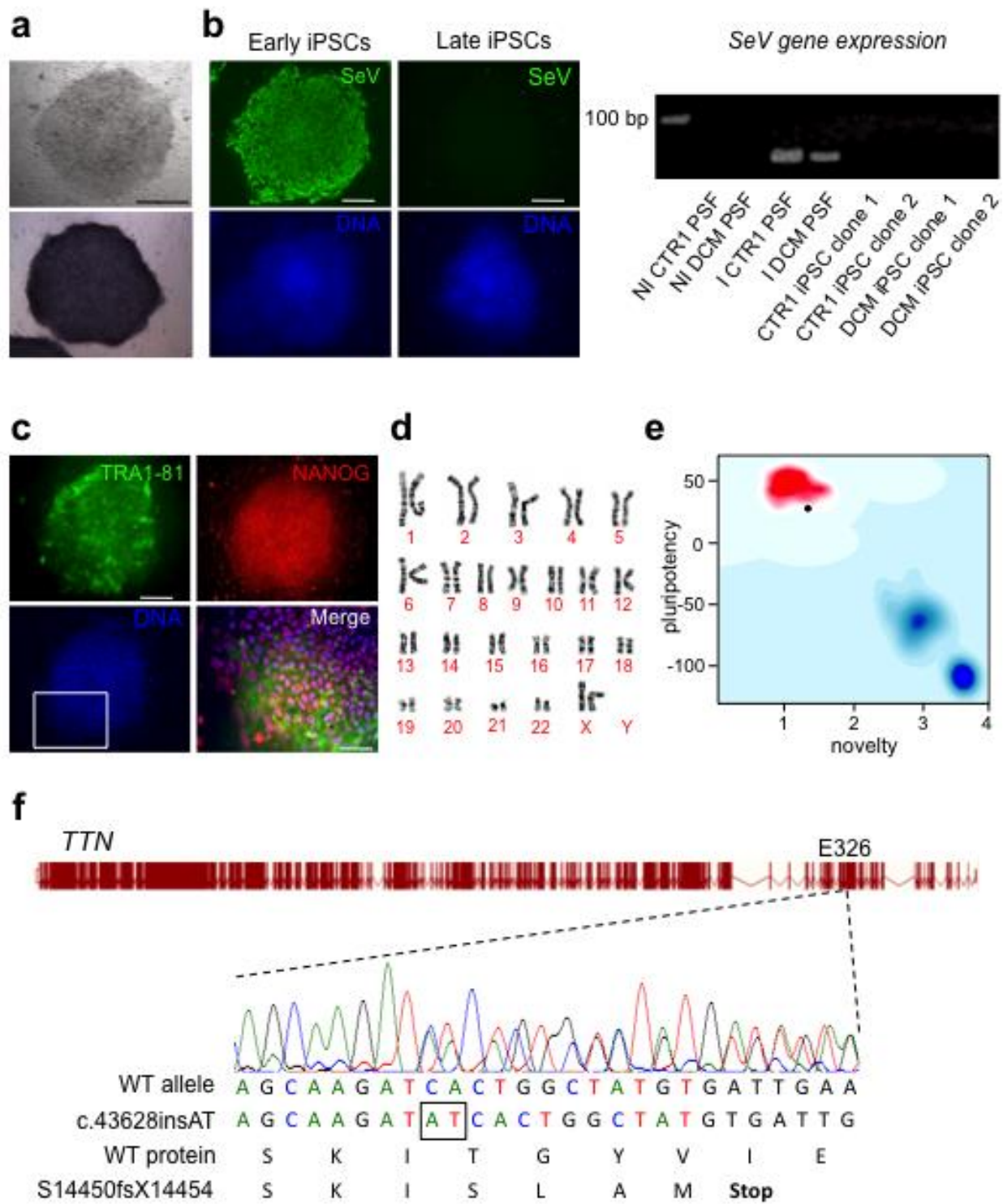
Part 3 Results

3.1 Evaluation of Exon-skipping for treating TTN-based DCM

3.1.1 Characterization of DCM iPSCs

After pluripotency characterization, we chose two iPSC clones from a 62-year-old female patient suffering the familial DCM and carrying the heterozygous TTN Ser14450fsX4 mutation (DCM-1 and DCM-2) and two clones from an unrelated healthy female individual (CTR1-1 and CTR1-2) for further studies (Fig 10, 11). We confirmed the presence of the 2-bp AT insertion in the TTN exon 326 of the patient's iPSC lines by genomic sequencing (Fig 10f). All four iPSC lines showed human embryonic stem cell morphology, were free of Sendai viral transgenes (Fig 10b), exhibited alkaline phosphatase activity (Fig 10a), NANOG and TRA1-81 immunoreactivity (two pluripotent stem-cell markers) (Fig 10c) and had normal karyotypes (Fig 10d); in addition, they passed the PluriTest with a low “novelty score” and a high “pluripotency score”, indicating typical properties of human pluripotent stem cells (Fig 10e). The four iPSC lines eventually exhibited reactivation of endogenous pluripotency genes (*SOX2*, *NANOG*, *OCT4*, *TDGF1* and *REX1*, Fig 11a) and displayed lower DNA methylation activities of *PTPN6*, *NANOG* and *RAB25* compared to their respective primary skin fibroblasts (PSFs) of origin^{202,203}; methylation levels of *LYST*, *GBP3* and *MGMT* were higher in hiPSCs than in PSFs, as expected for reprogrammed pluripotent stem cell lines²⁰⁴ (Fig 11b). Pluripotency of all 4 hiPSC lines was further confirmed by upregulation of genes representing all three germ layers in EBs formed by in vitro spontaneous differentiation of hiPSCs (Fig 11c).

Figure 10: Generation and characterization of the DCM iPSC line. (a) Representative images of colonies from a DCM iPSC clone in bright field microscopy (top) and after staining for alkaline phosphatase activity (bottom). Scale bar, 500µm. **(b)** On the left, Sendai virus (SeV) immunostaining of the same DCM iPSC clone at early and later culture passages as indicated. Scale bars, 200µm. On the right, RT-PCR detection for SeV transgene expression in two control (CTR1) and two DCM iPSC clones at passage 6, NI= uninfected; I= infected. **(c)** Immunofluorescence images of pluripotency markers NANOG (red) and TRA1-81 (green) in the DCM iPSC clone. Scale bar, 200µm. Merged image magnifies the framed area indicated the adjacent panel. Scale bar, 50µm. **(d)** Karyotyping of the DCM iPSC clone is normal. **(e)** PluriTest analysis of DCM iPSCs (black circle), indicating a high “pluripotency score” and a low “novelty score”, which suggests that they resemble normal human pluripotent stem cells (in red). **(f)** Sanger sequencing of the human *Titin* (*TTN*) gene in the DCM iPSC clone, confirming an heterozygous AT insertion mutation (c.43428insAT) in exon 326. This mutation causes a frameshift and subsequently a premature stop codon in this exon, resulting a truncating TTN after adding four novel amino acid residues (S14450fsX14454)²⁰⁵.



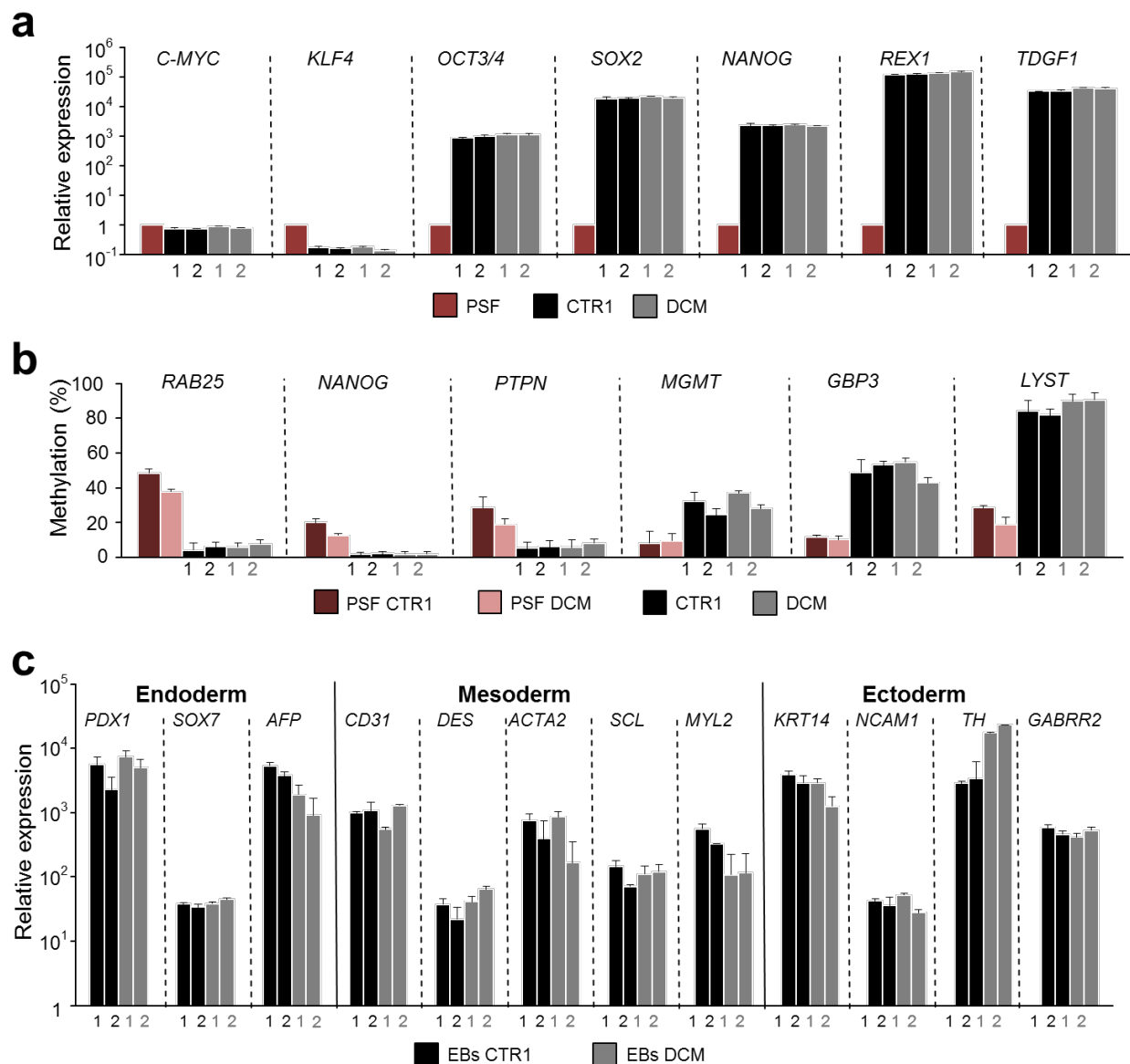


Figure 11: Reactivation of endogenous pluripotency genes in control and DCM iPSC clones and up-regulation of specific markers for the three embryonic germ layers in both clone-derived embryoid bodies. (a) Quantitative RT-PCR (qRT-PCR) analysis of endogenous pluripotency genes (*c-MYC*, *KLF4*, *OCT3/4*, *SOX2*, *NANOG*, *REX1*, and *TDGF1*) in two control (CTR1-1 and -2, black bars) and two DCM iPSC clones (DCM-1 and -2, grey bars). Expression levels are relative to corresponding primary skin fibroblasts (PSF, red bars), normalized to *GAPDH*, and shown as mean \pm s.e.m., $n=3$. (b) qRT-PCR analysis of methylation levels of *RAB25*, *NANOG*, *PTPN6*, *MGMT*, *GBP3* and *LYST* in CTR1-1 and -2 (black bars), DCM-1 and -2 (grey bars) and their corresponding PSFs (dark red and pink bars). Values are presented as mean \pm s.e.m., $n=3$. (c) qRT-PCR analysis of specific gene expression of the three germ layers, endoderm (*PDX1*, *SOX7*, and *AFP*), mesoderm (*CD31*, *DES*, *ACTA2*, *SCL*, *MYL2*, and *CDH5*), and ectoderm (*KRT14*, *NCAM1*, *TH*, and *GABRR2*) in embryoid bodies (EBs) at day 21 of differentiation from CTR1-1 and -2 (black bars) and DCM-1 and -2 (grey bars). Expression values are relative to corresponding undifferentiated iPSCs, normalized to *GAPDH*, and presented as mean \pm s.e.m., $n=3$.

3.1.2 Disease phenotyping of DCM iPSC-CMs carrying the Ser14450fsX4 mutation in *TTN* exon 326

3.1.2.1 Sarcomere remodeling in actin-RFP transfected iPSC-CMs

Due to the central role of titin as a scaffold protein with binding sites for various muscle proteins, we speculated that *TTN* truncating mutations could affect cardiac sarcomere assembly and stability. Therefore, we investigated the process of sarcomere assembly in hiPSC-CMs.

After enzymatic dissociation of cardiac explants into single hiPSC-CMs, these cells undergo a disintegration of their myofibrils and become rounded. When they attach to the culture dish, their myofibrils start to assemble again, giving the cells in this stage a resemblance of neonatal cardiomyocytes²⁰⁶.

In order to gain a better understanding of the sarcomere remodeling that takes place in hiPSC-CM during and after this dissociation process, we overexpressed a fusion protein of actin and red fluorescent protein (RFP) in dissociated single CMs using a modified baculovirus transgene delivery system (Fig 12a) that has been successfully applied to mammalian cells²⁰⁷. In these virus-transduced cells, live-cell imaging was performed repetitively over time (Fig 12b). The incorporation of the fluorescent actin-RFP fusion protein into the myofibrils allowed us to track myofibril dynamics in living cells.

Control hiPSC-CMs were infected with the actin-RFP baculovirus after two days of dissociation. At day one after infection, red-fluorescent cross-striated myofibrils could be observed in the center of the cell around the nucleus (Fig 12b). In the following days, the area occupied by well-organized RFP+ myofibrils grew more and more towards the periphery of the cell, and, within 4-5 days, encompassed the whole cell (Fig 12b). At this time point, rhythmic contractions of the cells were frequently observed. This pattern of sarcomere assembly was consistent with previously-reported data regarding sarcomerogenesis in rodent embryonic CMs^{208,209}. For our further analyses, we decided to use the term “fully organized” to describe the pattern of sarcomere structure in cells of this stage.

When we monitored the CMs further, we observed that the cross-striated sarcomeric structure started to disassemble in few CMs at 7-12 days of single cell culture, beginning in the perinuclear area (Fig 12b). The area of disassembled sarcomere structure eventually spreaded to the cell periphery (Fig 12b), similar to the sarcomere disassembly process observed in dividing mammalian CMs²¹⁰. We consistently observed this phenomenon in hundreds of CMs

from several independent experiments. Based on these observations, we hypothesized that, after dissociation, hiPSC-derived CMs undergo a radially-oriented, centrifugal sarcomere remodeling process resembling a corresponding mechanism earlier observed in neonatal CMs²⁰⁶. Thus, we assumed that CMs in which an organized sarcomeric pattern is restricted to the perinuclear region are undergoing sarcomere assembly, while CMs with striated myofibrils only in the cell periphery are experiencing sarcomere disassembly. These different patterns of sarcomere organization were thus all considered in the following experiments investigating sarcomere remodeling in DCM-CMs.

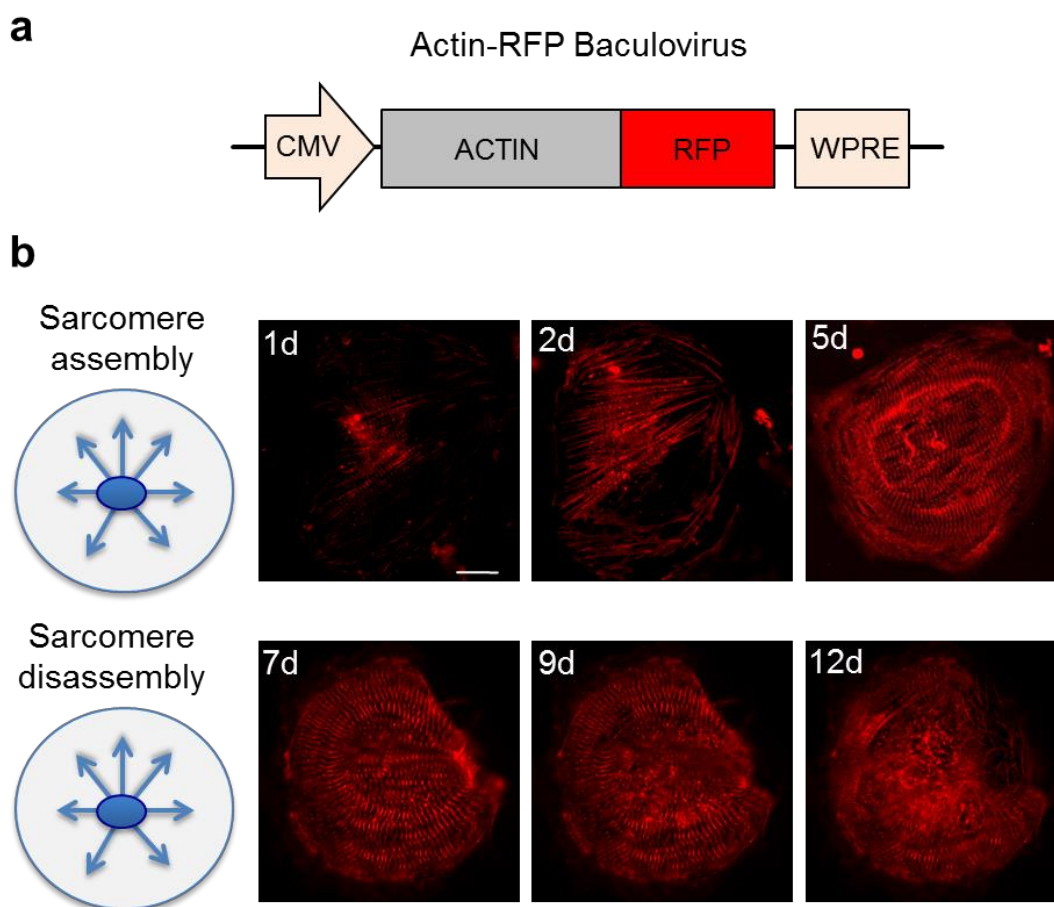


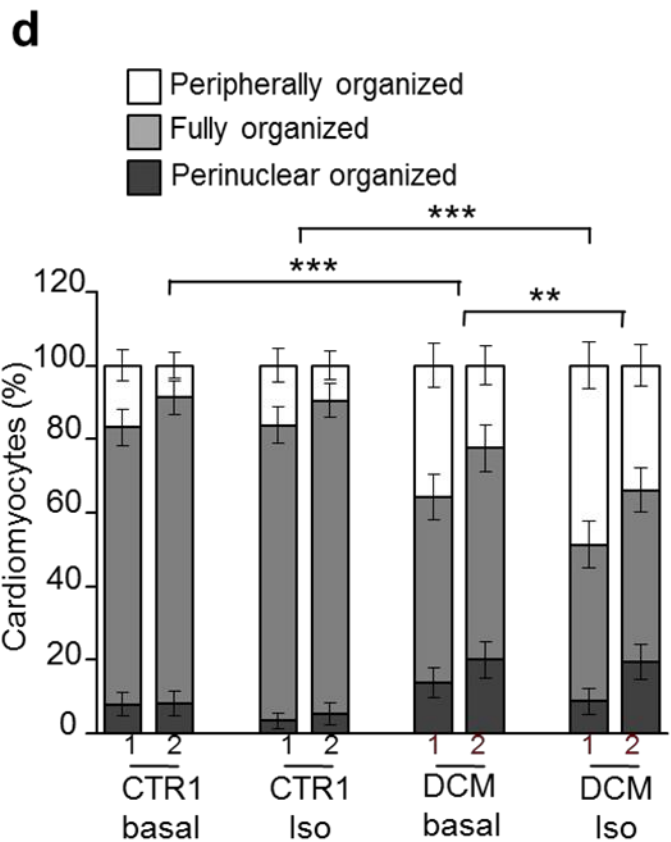
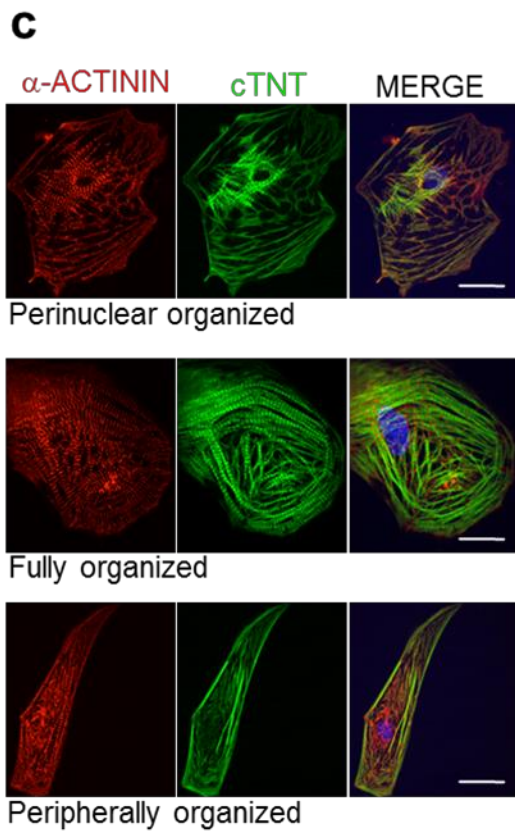
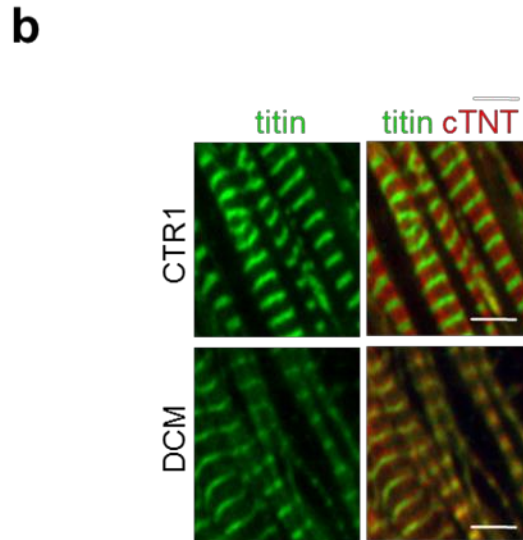
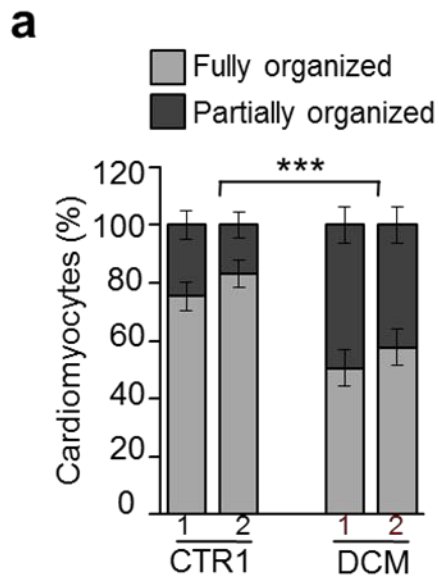
Figure 12: Live cell imaging of control hiPSC-derived cardiomyocytes overexpressing an exogenous actin-RFP protein. (a) Scheme of the modified insect viral (baculovirus) vector encoding an actin-red fluorescent fusion protein. **(b)** Images from an infected single control hiPSC-CM in the process of sarcomere assembly (top) and disassembly (bottom), respectively. Two days after infection of the baculovirus, the cell exhibits mature myofibrils with regular cross-striations only in the perinuclear region. At the day 5, striated sarcomeres occupy the whole cytoplasm. The myofibril organization is progressively lost by time in culture, with sarcomere disassembly starting around the nucleus and proceeding towards the periphery of the cell. Scale bar, 25 μm ²⁰⁵.

3.1.2.2 Assessment of sarcomere assembly and stability in DCM and CTR1 hiPSC-CMs

We then investigated the impact of the A-band truncating TTN mutation on sarcomeric assembly and stability in DCM hiPSC-CMs. Experimental analyses were performed 7 days after dissociation of cardiac explants and seeding as single CMs to provide sufficient time for sarcomeric reorganization. In these experiments, we did not use the fluorescent baculovirus, but assessed sarcomere organization by conducting immunocytochemical analysis for titin and other muscle proteins marking distinct portions of the sarcomere: myosin heavy chain (MHC, M-line), cardiac troponin T (cTNT, A-band), and α -actinin (Z-disk). In the DCM group, we observed a higher percentage of cardiomyocytes in which organized myofibrils only occupied half of the cytoplasm or less (Fig 13a). In addition, compared to CTR1 CMs, the immunofluorescence signal of Z-disk titin appeared more diffuse in the patient CMs (Fig 13b).

Based on the above-described spatio-temporal pattern of sarcomere remodeling, we analyzed in detail the immunocytochemistry results and discovered that over 80% of CTR1 but only 50% of DCM CMs had well organized myofibrils covering the entire cytoplasm under basal conditions (Fig 13c, d). Conversely, the percentages of cells with structured sarcomeres occupying merely the perinuclear or peripheral regions were significantly increased in the DCM group (Fig 13c, d), indicating defects in both myofibril reassembly and sarcomere stability in the patient-specific hiPSC-CMs. Moreover, isoproterenol (Iso) administration exacerbated the structural phenotype of DCM CM but had no significant effect on the CTR1 counterparts (Fig 13c, d), suggesting susceptibility of patient CMs to catecholamine-induced stress. Taken together, these results indicate that titin truncation mutants alter assembly and/or stability of the sarcomere structure in human cardiomyocytes.

Figure 13: Sarcomeric defects in *TTN Ser14450fsX4* iPSC-derived cardiomyocytes. (a) Percentage of iPSC-CMs with cross-striated myofibrils occupying less than a half (partially organized, dark gray) or the whole cytoplasm (fully organized, light gray) from two control and two patient clones. Statistical difference was tested using the two-sided chi-squared test (CTR1-1 basal: n = 283, CTR1-2 basal: n = 250, DCM-1 basal: n = 255, DCM-2 basal: n = 236; ***P = 1.93×10^{-16}). **(b)** Immunofluorescence images of titin (Z-disk portion) and cardiac troponin T (cTNT, A-band) in well-organized sarcomeres from CTR and DCM single cardiomyocytes under basal conditions. Scale bars, 5 μ m. **(c)** Immunofluorescence images (left) of α -actinin and cTNT in CTR1 and DCM single cardiomyocytes, illustrating 3 different levels of sarcomeric organization (perinuclear, fully and peripherally organized). Percentage of cells with different levels of sarcomeric organization (right) under basal and stress conditions. **(d)** Statistical difference was tested using the chi-squared test (CTR1-1 basal: n = 283, CTR1-2 basal: n = 250, DCM-1 basal: n = 255, DCM-2 basal: n = 236, CTR1-1 Iso: n = 245, CTR1-2 Iso: n = 230; DCM-1 Iso: n = 242 and DCM-2 Iso: n = 269; ***P = 1.93×10^{-16} , CTR basal versus DCM basal; ***P = 9.61×10^{-34} , CTR Iso versus DCM Iso; **P = 0.001, DCM basal versus DCM Iso). No significant differences were observed comparing CTR1 basal and CTR1 Iso groups. Scale bars, 25 μ m²⁰⁵.



3.1.2.3 Analysis of titin kinase associated signaling pathways

Titin does not only function as a molecular scaffold in sarcomerogenesis and myofibrillar assembly, but also as a hot spot for protein interactions and as a putative mechanotransduction

mediator²¹¹. So far, about 20 interaction partners have been identified, linking titin to multiple stress-sensing signaling pathways that modulate gene expression and protein turnover in cardiac muscle^{212,213}.

One of the most-extensively studied titin-related mechanotransduction pathways is the signaling complex of Nbr1/p62/SQSTM1/MURF2 that resides at the titin kinase (TK) domain and regulates the activity of the serum response factor (SRF) in response to mechanical stimuli⁶¹. Mutations of the titin TK domain result in the dissociation of the Nbr1/p62/SQSTM1/MURF2 complex and subsequent translocation of MURF2 into the nucleus where it binds to SRF and suppresses SRF-dependent muscle gene transcription⁶¹.

To investigate whether the truncating titin mutation present in our patient hiPSC line also affects the titin-dependent SRF pathway, we evaluated expression levels of SRF target genes, cardiac α -actin (*ACTC1*) and myosin heavy chain α and β (*MYH6* and *MYH7*)^{214,215} in both control and patient CMs. Quantitative RT-PCR analysis of 2-month-old hiPSC-CMs revealed a significant down-regulation of *ACTC1*, *MYH6*, and *MYH7* transcripts in the DCM CMs compared to control CMs (Fig 14), suggesting that the truncating mutation indeed results in abnormalities in the titin-TK-associated signaling pathway. Taken together, these findings demonstrate that defects in sarcomere assembly and stability of DCM CMs may partially derive from reduced expression level of sarcomeric proteins caused by disruption of the Nbr1/p62/SQSTM1/MURF2 signalosome.

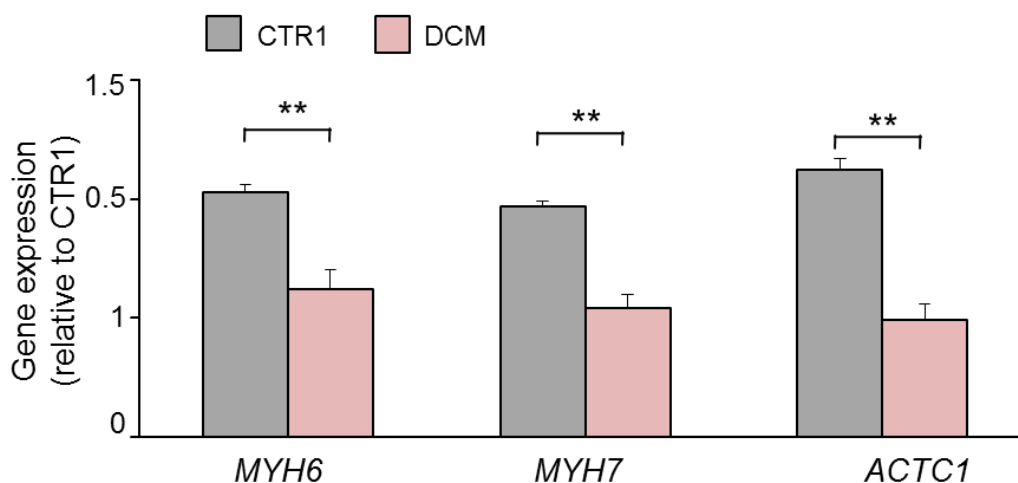


Figure 14: Abnormalities of SRF target gene expression in TTN Ser14450fsX4 iPSC-derived cardiomyocytes. qRT-PCR analysis of SRF target genes (*MYH6*, *MYH7* and *ACTC1*) in CTR1 and DCM single cardiomyocytes under basal conditions. Statistical difference was

tested using the two-sided Student's t-test (**P = 0.009, CTR1 versus DCM. Expression values were relative to CTR1, normalized to GAPDH, and presented as mean \pm S.E.M., n = 3²⁰⁵).

3.1.3 Rescue of DCM phenotypes by AON-mediated exon skipping

3.1.3.1 AON-mediated skipping of TTN exon 326

In order to rescue the disease phenotypes in patient CMs, we aimed at interfering with pre-mRNA splicing of the *TTN* gene in such a way that the mutated exon is skipped, which would result in synthesis of a shorter, internally-truncated, but still functional TTN protein, which would also contain the c-terminal TK domain. To this end, we designed four different AON sequences to mask exonic splicing enhancer (ESE) motifs in *TTN* exon 326 (Fig 15, Supplementary Table 1). To increase stability of the AONs, a phosphorothioate backbone was used in combination with a 2'-O-methyl phosphorothioate modification of the ribose (2OMePS). AONs were designed by our collaborators (details can be found in²¹⁶) and synthesized and purified by GeneTools, LLC (Philomath, OR, USA). As part of the design process, the efficacy of exome skipping was evaluated in the mouse atrial myocyte tumor cell line HL-1, demonstrating that only 2OMePS-AON1 and the combination of 2OMePS-AON1 and 3 specifically blocked the integration of exon 326 into the final titin mRNA transcript, restoring the open reading frame²¹⁶.

We validated the efficacy of AON1 and AON3 to induce skipping of the mutated *TTN* exon 326 in hiPSC-CMs generated from the DCM patient line. RT-PCR using primers amplifying a region encompassing exon 326 in combination with agarose gel electrophoresis was used to detect successful exon skipping.

When we transiently transfected DCM hiPSC-CMs with varying doses and combinations of 2OMePS-AONs 1 and 3 (Supplemental Table 1), we observed incomplete and nonspecific skipping of exon 326 at all tested concentrations, with the highest amount of correctly-skipped transcript in cells treated with the combination of 2OMePS-AON1 and AON3 at the highest tested concentration (200nM, Fig 16a). The marked concentration dependence was likely due to a low transduction efficiency of AONs, which we confirmed by transducing the cells with a 5'-fluorescein-labeled 2OMePS AON that resulted in a fluorescence signal in less than 10 percent of the cells (Fig 16b).

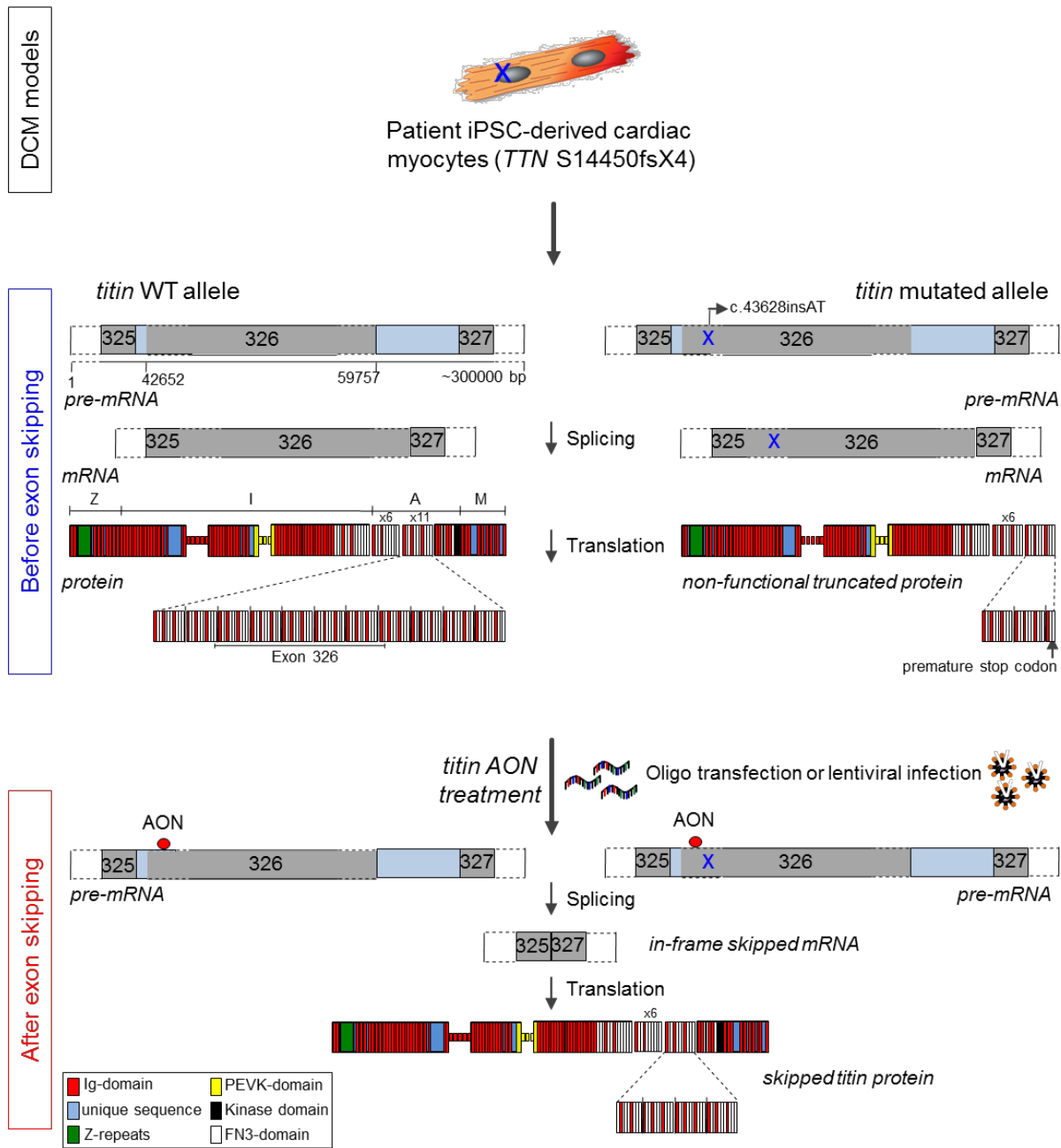


Figure 15: Scheme of exon skipping strategy for excision of *TTN* exon 326 in CTR1 and DCM hiPSC-CMs. In the patient specific hiPSC-CMs carrying heterozygous autosomal mutation of *TTN* S14450fsX4 in titin exon 326, both the wild type (WT) and mutated allele transcribe full length of titin pre-mRNA and mRNA, while the premature stop codon caused by the mutation results in a truncating titin, missing expression of the partial exon 326 and following exons. After AON treatment targeting titin exon 326, excision of this exon occurs during post transcription modification and results in a shorter but reversed expression of important domains including A-band titin and kinase domain²⁰⁵.

Results

In order to improve the efficiency of nuclear AON delivery to hiPSC-CM, we pursued an alternative strategy relying on lentiviral gene transfer. To this end, we constructed a lentiviral vector in which the AON1 and AON3 fragments were embedded in a modified U7 small-nuclear RNA (U7snRNA). U7snRNA, which is physiologically involved in processing of histone pre-mRNAs, can be modified to be directed to the spliceosome²¹⁷ and then used as a shuttle for antisense RNA sequences. Following the modified U7snRNA, the vector contained an IRES-GFP cassette to allow identification of transduced cells. The complete vector was termed U7snRNA-*TTNAONs*-IRES-GFP (Fig 17a).

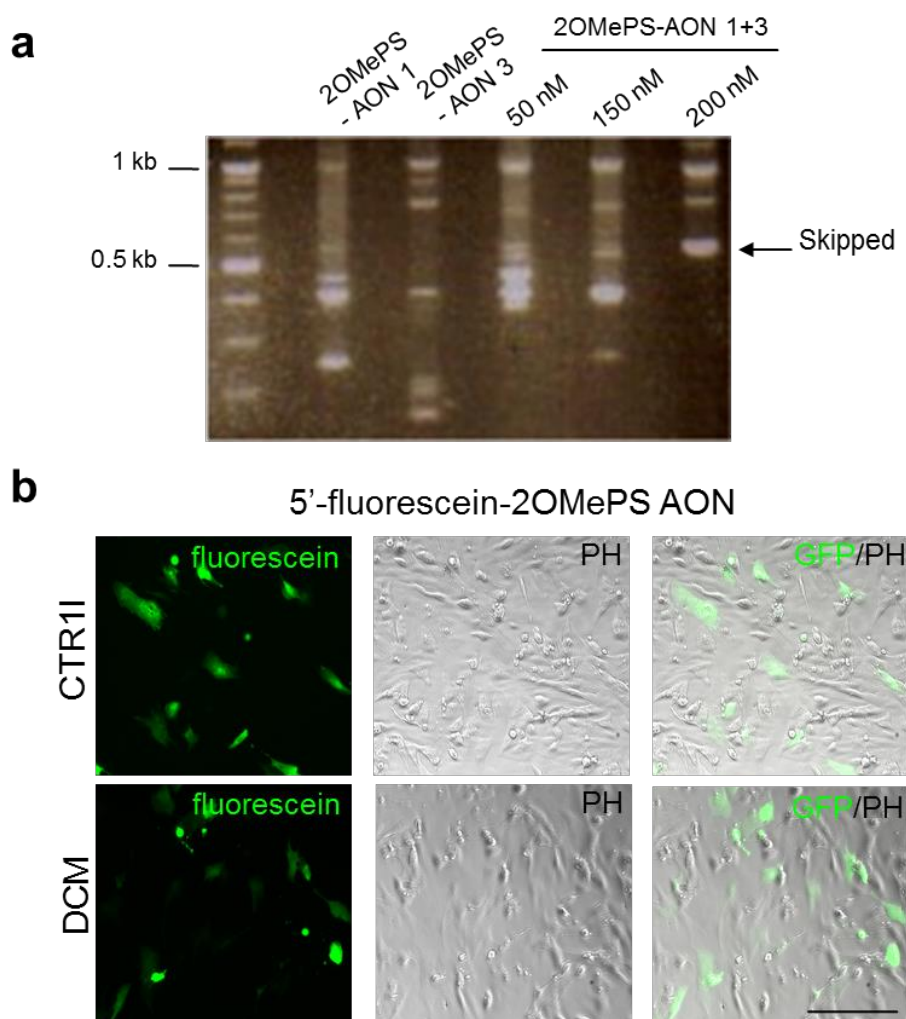


Figure 16: 2OMePS AON-mediated skipping of exon 326 in *TTN* Ser14450fsX4 iPSC-derived cardiomyocytes. (a) RT-PCR analysis of *TTN* exon 326 transcripts from DCM cardiomyocytes transiently transfected with 2OMePS-AON1, 2OMePS-AON3, and 2OMePS-AON1 + 3. **(b)** CTR1 and DCM iPSC-CMs were transfected with 5'-fluorescein-labeled 2OMePS AON (600 nM final concentration) and imaged after 3 hours of incubation. Scale bar, 200 μ m²⁰⁵.

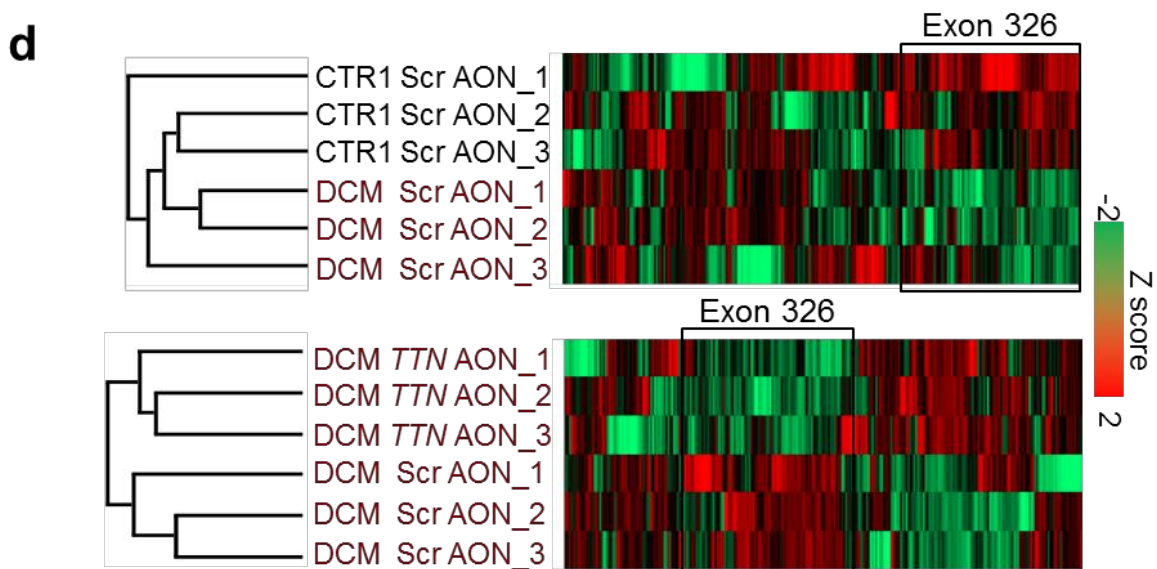
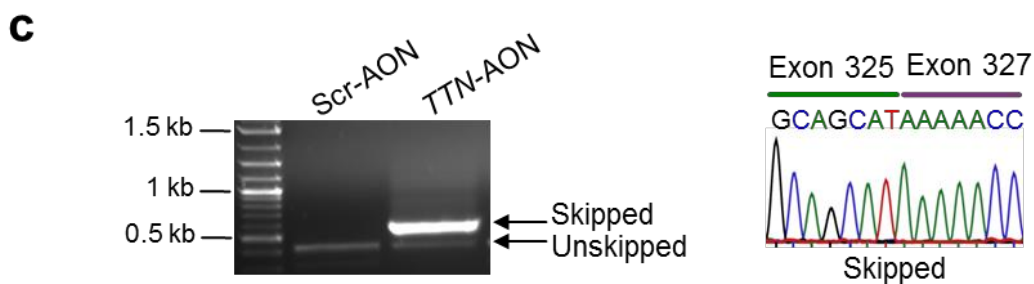
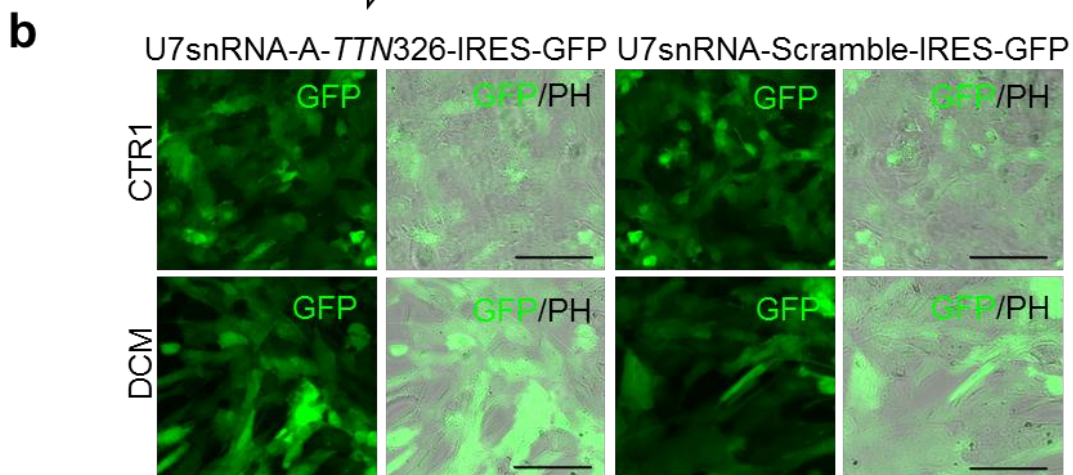
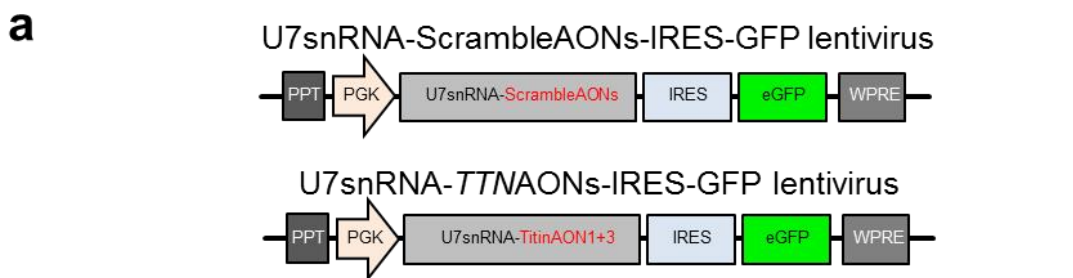


Figure 17: Efficient skipping of exon 326 in *TTN* Ser14450fsX4 iPSC-derived cardiomyocytes by lentivirus mediated AON transfer. (a) Scheme of the U7snRNA-*TTNAONs*-IRES-GFP (*TTN*-AON) and U7snRNA-ScrambleAONs-IRES-GFP (Scr-AON) lentiviral vectors. For the expression of the AON1 and AON3, AONs were inserted into the U7snRNA-IRES-GFP vector, a scrambled control was made in the same way. (b) GFP expression in hiPSC-CMs after lentiviral infection. Images were acquired 24 hours after infection. Scale bar, 100µm. (c) RT-PCR analysis (left) and direct sequencing (right) of *TTN* exon 326 transcripts from DCM iPSC-CMs infected with the U7snRNA-*TTNAONs*-IRES-GFP lentiviral vector carrying the AON1 and 3 sequences (*TTN*-AON) or with a control vector (Scr-AONs). (d) Mass spectrometry-based analysis of titin peptides in cells infected with the Scr-AON and *TTN*-AON vectors. Unsupervised hierarchical clustering identified a cluster significantly enriched in peptides mapping to exon 326 that was down-regulated in DCM Scr-AON cardiomyocytes compared to CTR1 Scr-AON cardiomyocytes (n = 3, P = 9.03x10⁻⁸, Fisher's exact test, FDR = 0.04, top). Down-regulation of exon 326 was also detected in DCM *TTN*-AON cells when compared to DCM Scr-AON cells (n = 3, P = 0.02, Fisher's exact test, bottom)²⁰⁵.

A control vector was constructed that encoded the same construct, but was modified to contain a non-specific scrambled AON fragment instead of the specific AON sequences (U7snRNA-ScrAONs-IRES-GFP, see Fig 17a). Two days after lentiviral infection, ~85% of both CTR and DCM iPSC-CMs were GFP positive (GFP+) (Fig 17b). *TTN* exon 326 was completely and specifically skipped in cells infected with U7snRNA-*TTNAONs*-IRES-GFP, as detected by RT-PCR and Sanger sequencing (Fig 17c). Efficiency of *TTN* exon 326 skipping was further confirmed at the protein level using shotgun proteomics based on mass spectrometry (MS) (Fig 17d). Among ~63,000 peptides detected in total, 1,719 mapped to the human titin protein, and 298 corresponded to the sequence encoded by exon 326. Unsupervised hierarchical clustering of the titin peptides identified from the different cell lines treated with the different lentiviral constructs revealed a cluster of peptides mapping to exon 326 that was down regulated in DCM-CMs as compared to control CMs. In DCM-CMs, this cluster was unregulated upon AON treatment as compared to treatment with scrambled-RNA (Fig 17d).

3.1.3.2 Rescue of sarcomere assembly and stability by skipping of *TTN* exon 326

Next, we investigated the effect of restoring the reading frame of the *TTN* transcript by exon skipping in patient-derived DCM CMs (Fig 18). CMs generated from the CTR1 and DCM hiPSC lines were dissociated and plated as single cells. Two days later, they were infected with U7snRNA-*TTNAONs*-IRES-GFP or U7snRNA-ScrAONs-IRES-GFP lentivirus (Fig 18a). Five days after infection, we analyzed the distribution of striated myofibrils in GFP-positive CMs. We found that lentivirus-mediated skipping of *TTN* exon 326 had no deleterious effects on CTR1 CMs, but reduced the high percentage of CMs with poorly organized myofibrils in the DCM group, indicating a partial rescue of the sarcomeric abnormalities in DCM CMs (Fig 18b). In

addition, lentivirus infection (using the scrambled control virus) had no significant influence on sarcomere remodeling in both healthy and diseased cellular background (Fig. 18c).

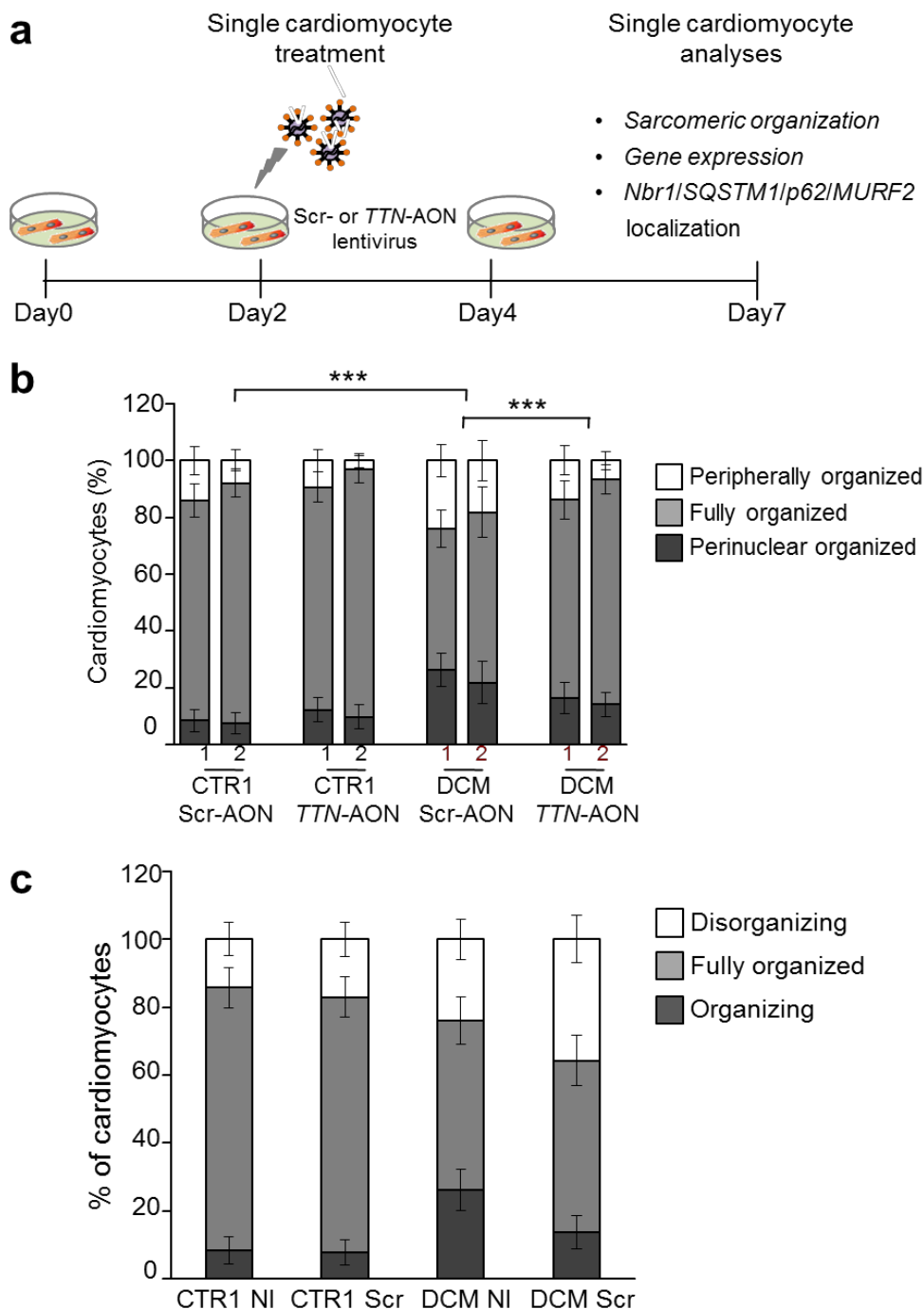


Figure 18: Effect of exon skipping on sarcomere remodeling in CTR1 and DCM iPSC-derived cardiomyocytes. (a) Experimental design. (b) Percentage of perinuclear, fully, and peripherally organized single cardiomyocytes from two CTR1 and two DCM iPSC clones after infection with the U7snRNAScrAONs-IRES-GFP and U7snRNA-*TTN*AONs-IRES-GFP

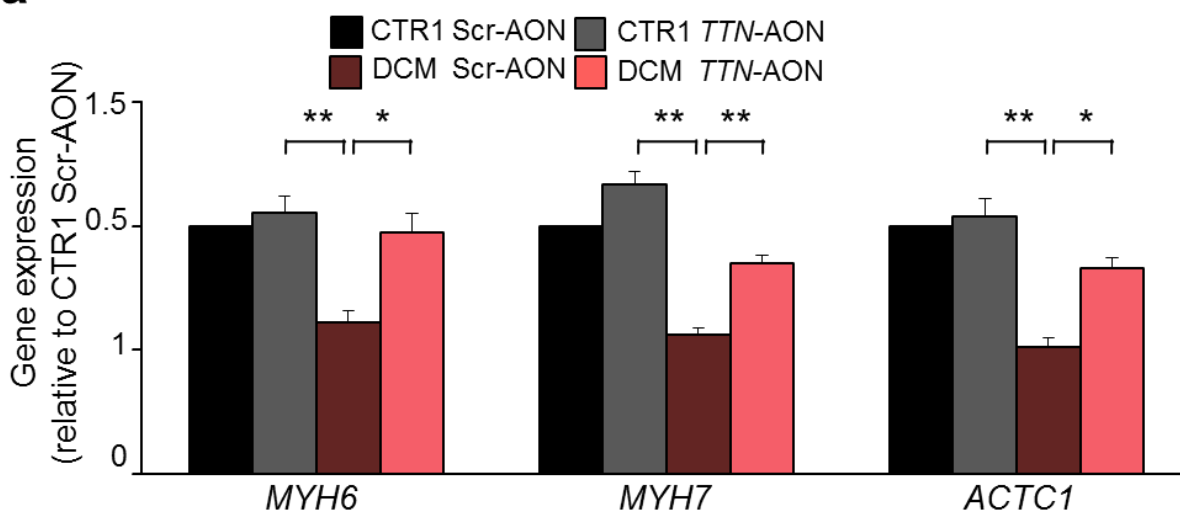
lentiviruses. Statistical difference was tested using the two-sided chi-squared test (CTR1-1 Scr-AON: n = 190, CTR1-2 Scr-AON: n = 200, DCM-1 Scr-AON: n = 221, DCM-2 Scr-AON: n = 115, CTR1-1 *TTN*-AON: n = 223, CTR1-2 *TTN*-AON: n = 187, DCM-1 *TTN*-AON: n = 171, DCM-2 *TTN*-AON: n = 243; ***P = 4.22×10^{-15} , CTR1 Scr-AON versus DCM Scr-AON; ***P = 4.61×10^{-2} , DCM Scr-AON versus DCM *TTN*-AON). No significant differences were observed comparing CTR1 Scr-AON and CTR1 *TTN*-AON groups (c)²⁰⁵.

3.1.3.3 Normalization of sarcomeric protein expression and Nbr1/p62/ SQSTM1/MURF2 signalosome by skipping of *TTN* exon 326

We further evaluated whether expression levels of SRF target genes in patient CMs could be normalized by lentivirus-mediated *TTN* exon 326 skipping. In DCM-CMs infected with the U7snRNATTNAONs-IRES-GFP construct, the pathologically-altered expression levels of SRF targets were partially restored (Fig 19a). No significant effects were seen in DCM CMs infected with the scrambled control virus or in control CMs infected with the AON virus (Fig 19a).

The effect of virus-mediated exon skipping on DCM cells is concordant with results of immunocytochemistry assessment of SRF localization in hiPSC-derived CMs 7 days after dissociation, showing a significantly-higher percentage of cells with extranuclear SRF staining in the DCM than in the control group (Fig 19b). In addition, we observed a disturbance in the intracellular distribution of MURF2, Nbr1, and p62/SQSTM1 in the DCM CMs, with an increased number of cells showing a marked nuclear localization of MURF2 and a diffused cytosolic localization of Nbr1 and p62/SQSTM1 instead of a striated pattern (Fig 19b). U7snRNA-TTNAONs-IRES-GFP lentivirus infection partly normalized the cellular distribution of all these signalosome proteins in the diseased CMs, while no effects were detected in the CTR1 CM (Fig 19b).

a



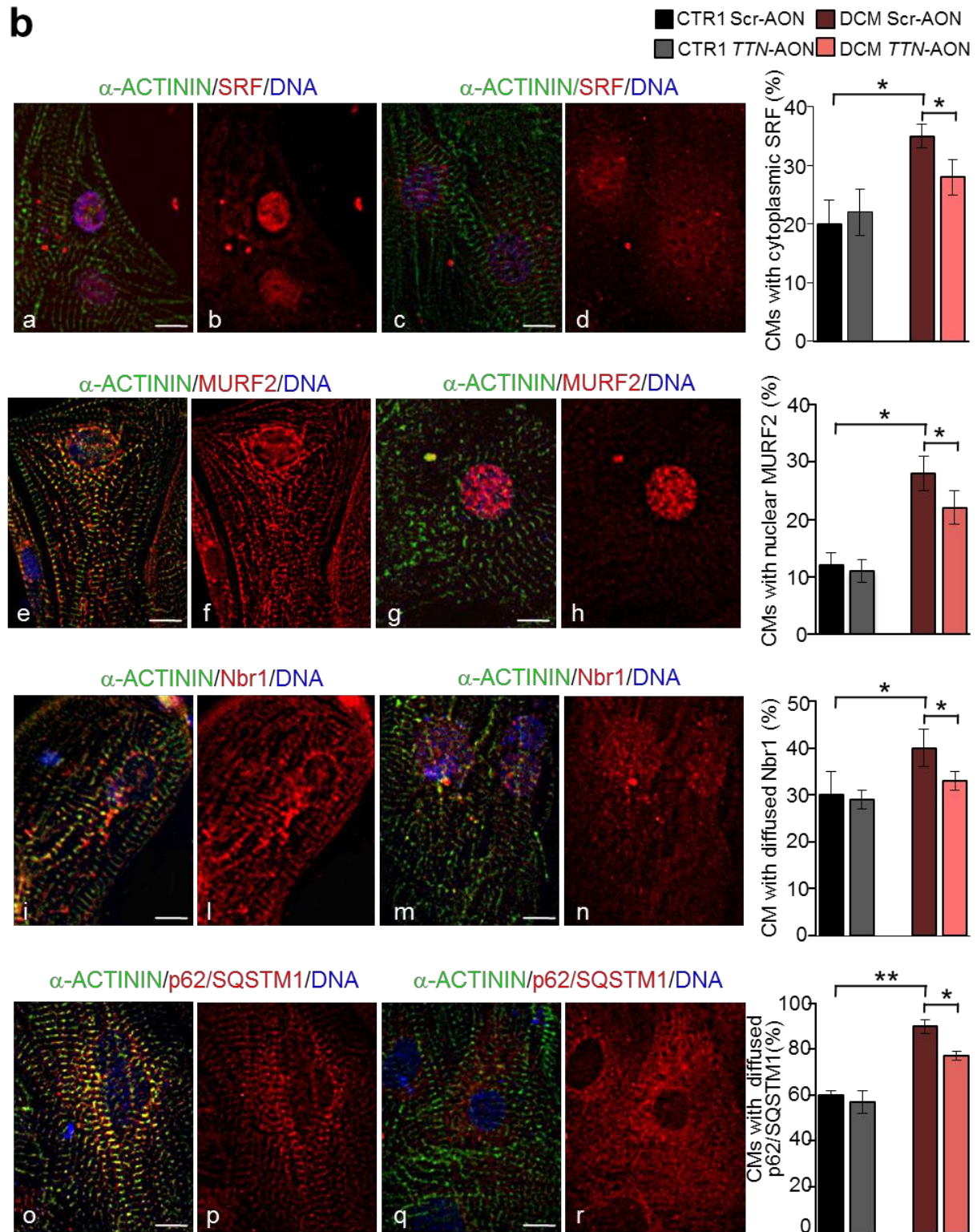


Figure 19: Exon skipping-based rescue of SRF target gene expression and Nbr1/p62/SQSTM1/MURF2 subcellular distribution in TTN Ser14450fsX4 iPSC-derived cardiomyocytes. (a) qRT-PCR analysis of SRF target genes (*MYH6*, *MYH7* and *ACTC1*) in CTR1 and DCM single cardiomyocytes after infection with control U7snRNA-ScrAONs-IRES-GFP (Scr-AON) and the U7snRNA-*TTN*AONs-IRES-GFP (*TTN*-AON) lentiviruses. Statistical difference was tested using the two-sided Student's t-test (**P = 0.009, CTR1 Scr-AON versus DCM Scr-AON; *P = 0.04, DCM Scr-AON versus DCM *TTN*-AON for *MYH6*; **P = 0.002, CTR1 Scr-AON versus DCM Scr-AON; **P = 0.002, DCM Scr-AON versus DCM *TTN*-AON for *MYH7*; **P = 0.004, CTR1 Scr-AON versus DCM Scr-AON; *P = 0.02, DCM Scr-AON versus DCM *TTN*-AON for *ACTC1*). No significant differences were observed comparing the CTR1 Scr-AON and CTR1 *TTN*-AON groups. Expression values were relative to CTR1 Scr-AON, normalized to *GAPDH*, and presented as mean \pm S.E.M., n = 3. (b) Immunofluorescence images showing normal (a, b, e, f, i, l, o, p; indicated in white) and altered (c, d, g, h, m, n, q, r; indicated in white) intracellular distribution of SRF (a and b, nuclear; c and d, cytoplasmic), MURF2 (e and f, sarcomeric; g and h, nuclear), Nbr1 (i and l, sarcomeric; m and n, diffused), and SQSTM1/p62 (o and p, sarcomeric; q and r, diffused) in representative single cardiomyocytes (left). Sarcomeres are marked by α -actinin. On the right, percentage of CTR1 and DCM cardiomyocytes showing cytoplasmic expression of SRF, nuclear accumulation of MURF2, and diffused expression of Nbr1 and of SQSTM1/p62 after infection with the control Scr-AON and the *TTN*-AON lentiviruses (right). Data represent mean values \pm SEM from two control and two DCM clones. Statistical difference was tested using the two-sided chi-squared test (CTR1 Scr-AON: n = 874, n = 874, n = 882 and n = 890, CTR1 *TTN*-AON: n = 880, n = 990, n = 878 and n = 890, DCM Scr-AON: n = 890, n = 887, n = 884 and n = 886, DCM *TTN*-AON: n = 900, n = 875, n = 899 and n = 891 for SRF, MURF2, Nbr1 and SQSTM1/p62, respectively; *P = 0.01, CTR1 Scr-AON versus DCM Scr-AON; *P = 0.04, DCM Scr-AON versus DCM *TTN*-AON for SRF; *P = 0.02, CTR1 Scr-AON versus DCM Scr-AON; *P = 0.04, DCM Scr-AON versus DCM *TTN*-AON for MURF2; *P = 0.03, CTR1 Scr-AON versus DCM Scr-AON; *P = 0.03, DCM Scr-AON versus DCM *TTN*-AON for Nbr1; **P = 0.009, CTR1 Scr-AON versus DCM Scr-AON; *P = 0.01, DCM Scr-AON versus DCM *TTN*-AON for SQSTM1/p62). No significant differences were observed comparing CTR1 Scr-AON and CTR1 *TTN*-AON groups. Scale bars, 50 μ m²⁰⁵.

3.2 Subtype promoter-driven action potential imaging for precise disease modeling and drug testing in hiPSC-CMs

3.2.1 Optical AP recording in hiPSC-CMs using a VSFP sensor

3.2.1.1 Molecular characterization of hiPSC-CMs after PGK-VSFP lentiviral infection

The first step towards development of a system of promoter-driven subtype-specific membrane potential recordings in hiPSC-CMs was the generation of a lentiviral construct to express a genetically-encoded membrane voltage indicator in hiPSC-CMs. Due to the ratiometric imaging principle that reduces susceptibility to artifacts caused by cell movement, we decided to use a Förster resonance energy transfer (FRET)-mediated membrane potential sensor (voltage-sensitive fluorescent protein, VSFP). We used a recently-described VSFP variant called VSFP-CR¹⁷², which is based on FRET between a green and a red color variant of the green fluorescent protein GFP. To establish the technology, we first constructed a lentivirus in which VSFP-CR is expressed under the control of the constitutive PGK promoter (mouse phosphoglycerate kinase 1 promoter), which is widely used in mammalian systems to drive ectopic gene expression²¹⁸.

The sensor consists of a transmembrane voltage-sensing domain fused to a tandem of two fluorescent proteins (in VSFP-CR, the GFP variant clover and the RFP variant mRuby2 are used). The conformational change of the transmembrane domain upon depolarization of the cell results in a FRET increase (Fig 20a).

We first evaluated whether VSFP-CR allows stable and prolonged detection of APs in hiPSC-CMs. To this end, we used 3-month-old CMs generated by EB differentiation of a healthy control hiPSC line (CTR2), which we had previously characterized by patch-clamp electrophysiology³³. CTR2 beating EBs were dissociated into single CMs, reseeded on glass bottom microwell dishes with a density of 1.6×10^5 CMs / cm², and infected by PGK-VSFP lentivirus 2 days after dissociation. Three days after infection, both GFP (Clover) and RFP (mRuby2) signals could be detected and imaged using the epifluorescence microscopy setup (Fig 20b). PGK-VSFP was efficiently expressed in infected CMs, with a fluorescence signal detectable in ~95% of the CMs (Fig 20b).

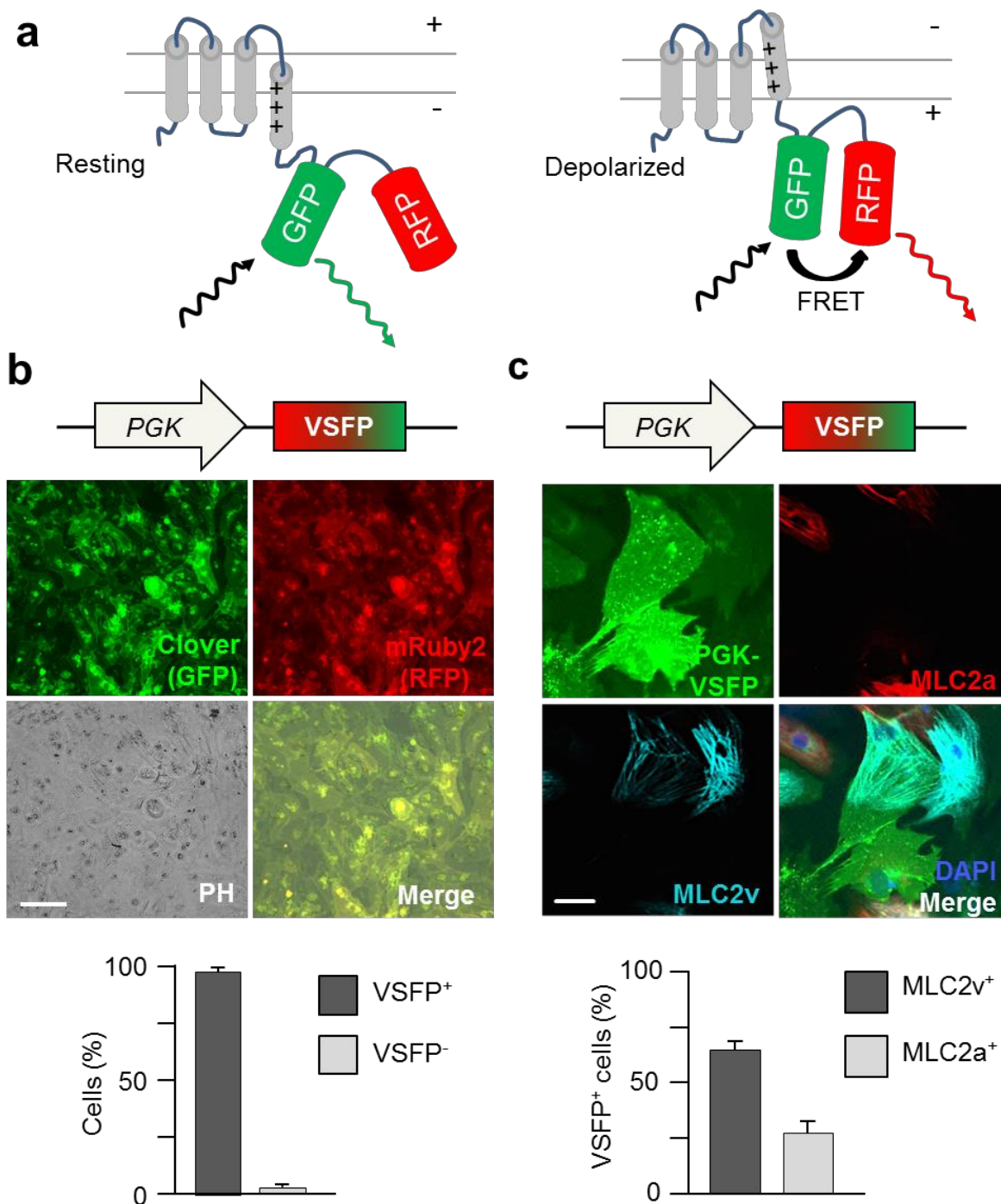


Figure 20: Molecular characterization of hiPSC-CMs expressing PGK-VSFP. (a) Scheme of the mode of action of the membrane potential sensor VSFP-CR. Voltage-sensing transmembrane domain is linked to a pair of a green and a red fluorescent protein (the GFP variant clover and the RFP variant mRuby2). Depolarization of the cell membrane results in a structural rearrangement, bringing GFP and RFP closer together. This increases the efficiency of radiationless excitation energy transfer (FRET) from GFP to RFP, making GFP appears dimmer and RFP appears brighter. (b) Live imaging of hiPSC-derived CMs after 5-day infection

of a PGK-VSFP lentivirus. PGK-VSFP positive CMs showing both GFP (in green) and RFP (in red) signals. Bar graph displaying the percentage of cells expressing VSFP ($n = 857$ cells). Scale bar, $100\mu\text{m}$. **(c)** Pseudocolor images of hiPSC-derived CMs infected with the PGK-VSFP lentivirus and stained for MLC2v (in cyan) and MLC2a (in red). Bar graph showing the percentage of cells expressing MLC2v and MLC2a among the cells expressing VSFP ($n = 325$ cells). Scale bar, $20\mu\text{m}$. Error bars represent 95% confidence intervals²¹⁹.

As expected given the ubiquitous nature of the PGK promoter, PGK-VSFP marked all cell types existing in the cardiac EB explants, including not only the cardiac lineages expressing either myosin light chain 2v (MLC2v, ventricular myocytes) or 2a (MLC2a, atrial myocytes) isoform (Fig 20c), but also non-cardiac lineages, which did not express any MLC2 isoforms (Fig 20c). The percentage of cells expressing MLC2v (ventricular myocytes) was around 66%, while MLC2a-positive cells constituted approximately 27% of the cells (Fig 20c).

3.2.1.2 VSFP-based AP imaging in hiPSC-CMs

When we imaged spontaneously-beating hiPSC-CMs infected with PGK-VSFP, we found the voltage sensor responded to membrane depolarization with an increase of the RFP fluorescence signal and a concomitant decrease of the GFP fluorescence signal, which resulted in an increase of the RFP/GFP ratio in parallel to each AP (Fig 21a, b and c).

For the calculation of AP characteristics, six to eight individual APs from one recording were averaged by aligning them at their respective starting points, and APD_{50} and APD_{90} were calculated from the averaged AP signal as the durations from the AP starting point until the time when repolarization was completed by 50 and 90 percent, respectively (Fig 21d). APD_{50} and APD_{90} are well-accepted parameters for measuring AP durations. Among the PGK-VSFP marked cells, average APD_{50} and APD_{90} were $180\pm 30\text{ms}$ and $375\pm 65\text{ms}$, respectively ($n=102$; Fig 21e). These values were in good agreement with previously-reported current clamp recordings from hiPSC-CMs generated from the same hiPSC line³³.

These results indicate that high-throughput AP recording from hiPSC-CMs is feasible using the PGK-VSFP based optical membrane potential sensor. However, in these measurements, the hiPSC-CMs likely represent a mixture of different cardiomyocyte subtypes (e.g., ventricular, atrial and nodal lineages). Since these subtypes might harbor distinct phenotypes, the unspecific imaging might result in a dilution of observed phenotypes. In order to address this problem, we developed VSFP expression constructs driven by subtype-specific promoters to achieve subtype-specific AP recordings.

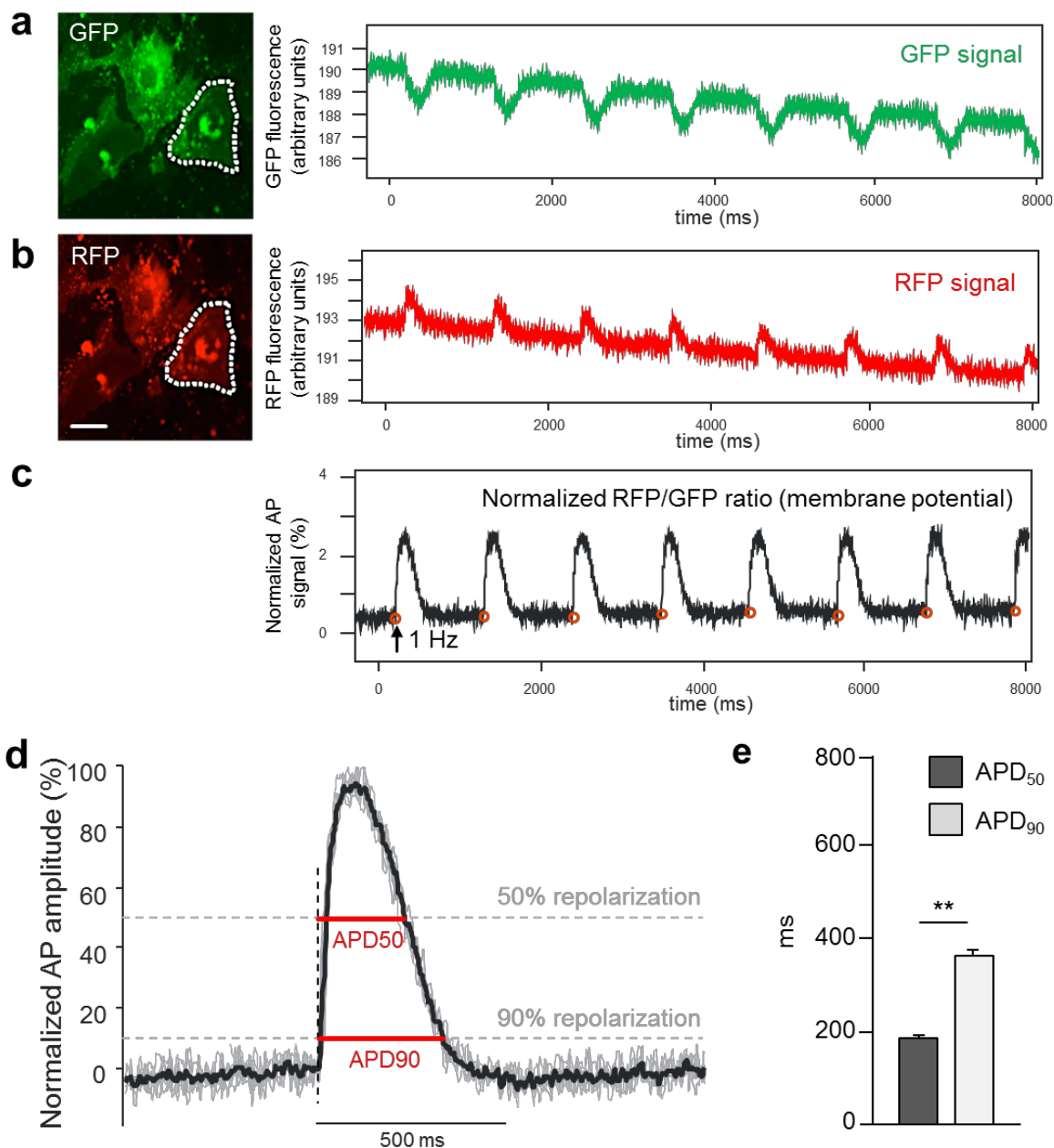


Figure 21: FRET-based optical membrane potential recordings in hiPSC-derived cardiomyocytes. Background-corrected GFP and RFP fluorescence signals are shown in (a) and (b), respectively. The dotted line shows the region of interest from which the fluorescence signal over one cell was quantified. Scale bar, 20 μ m. The signal after correction for baseline drift and normalization to the baseline value is shown in (c). Every AP was normalized to the maximum depolarization. The red circles indicate the manually-set starting points of the APs. In panel (d), all subsequent normalized action potentials aligned at the starting points, are shown as grey lines. An average (shown in black) was calculated. From this averaged AP signal, APD₅₀ and APD₉₀ were calculated as indicated. APD₅₀ or APD₉₀, action potential duration measured at 50% or 90% repolarization. (e) AP duration (APD₅₀ and APD₉₀) in cells expressing PGK-VSFP paced at 1 Hz. Error bars represent 95% confidence intervals, n=92 cells ** p<0.01

3.2.2 Subtype-specific optical AP recording of hiPSC-CMs

3.2.2.1 Identification of subtype-specific promoters in hiPSC-CMs

The paucity of established subtype specific markers for human iPSC-derived CMs represents a problem for studying the typical phenotypes in specific myocyte lineages present within a mixed CM population. Although the *MLC2v* enhancer is well accepted as a specific marker for both embryonic and adult ventricular myocytes^{196, 220}, reliable promoters for atrial and nodal lineages are still an area of ongoing investigations.

To identify promoter elements that would allow driving VSFP expression in either of the 3 major cardiomyocyte subtypes, we performed a screening experiment for lineage-specific markers in hiPSC-CMs. Our screen was based on pool of candidate genes whose expression might be restricted to specific lineages, including *MLC2v*, adult atrial marker *MLC2a* and sarcolipin (*SLN*) as well as potential nodal marker, the hyperpolarization-activated cyclic nucleotide-gated potassium channel 4 (*HCN4*) and short stature homeobox 2 (*SHOX2*) selected from lately literature reports. For the ventricular lineage, *MLC2v* have been reported specifically expressed in ventricular-like human hiPSC-derived CMs²²⁰. *MLC2a* is a marker for atrial myocytes in the adult heart²²¹, while *HCN4* is specifically expressed in the adult conduction system and is required for mature cardiac pacemaker activity^{222, 220, 223}. *SLN* is known to be exclusively expressed in human atria²²⁴ and the feasibility of using the *SLN* promoter to mark atrial-like CMs has been recently suggested by using a BAC reporter construct encompassing the genomic region ranging from 144 kb upstream to 45 kb downstream of the *SLN* locus²²⁵. For *SHOX2*, which is expressed only in the sinoatrial node region of the developing and adult heart^{226, 227}, a previous study in mouse embryonic stem cell-derived CMs demonstrated that a 3.8 kb promoter fragment is sufficient to allow antibiotic selection of nodal-like cells²²⁸.

Starting from a typical mixture of hiPSC-CMs generated by EB differentiation, we applied patch clamp electrophysiology to record APs and classify the cells as ventricular, atrial, or nodal based on the AP characteristics³³. Subsequently, the single cells were harvested by sucking into the patch pipette, and single-cell RT-PCR was applied to verify the presence or absence of transcripts from the panel of candidate genes (Fig 22a). Our screening revealed that *MLC2v* was indeed expressed specifically in the cells with ventricular AP properties (i.e., a slow beating rate, a negative maximum diastolic potential (MDP), a rapid upstroke velocity, a large AP amplitude and long AP durations) (Fig 22b). *SLN* was found to be transcribed restrictively in

cells with atrial-like AP characteristics (i.e., a slow beating rate, a fast upstroke velocity and short AP durations), while *SHOX2* was identified as specific marker for nodal-like hiPSC-CMs (Fig. 22b).

Encouraged by these results, we generated lentiviruses in which VSFP is driven by either the *MLC2v* enhancer or ~3.5 kb of promoter region preceding the transcript starting sites of the *SLN* or *SHOX2* genes, respectively. Transduction efficiency, as assessed by quantitative PCR on genomic DNA for VSFP transgene integration, was high for all lentiviral constructs and comparable to that of PGK-VSFP (Fig 23).

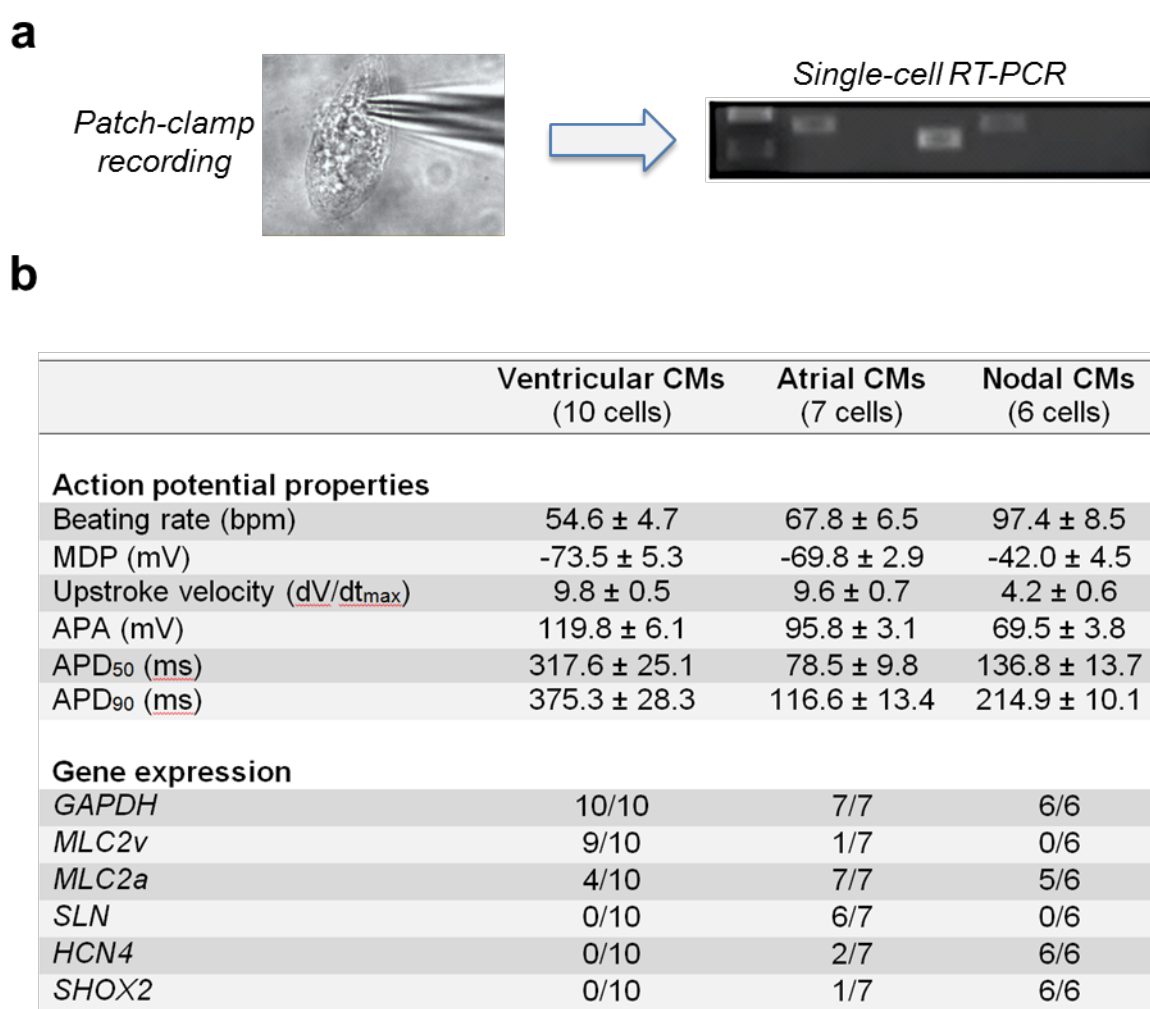


Figure 22: Electrophysiological and molecular properties of human iPSC-CM subtypes. (a) Experimental design. **(b)** Characteristics of hiPSC derived myocytes and corresponding expression profile are listed. Red circle indicates specific gene for each CM subtypes. MDP, maximum diastolic potential; APA, action potential amplitude²¹⁹.

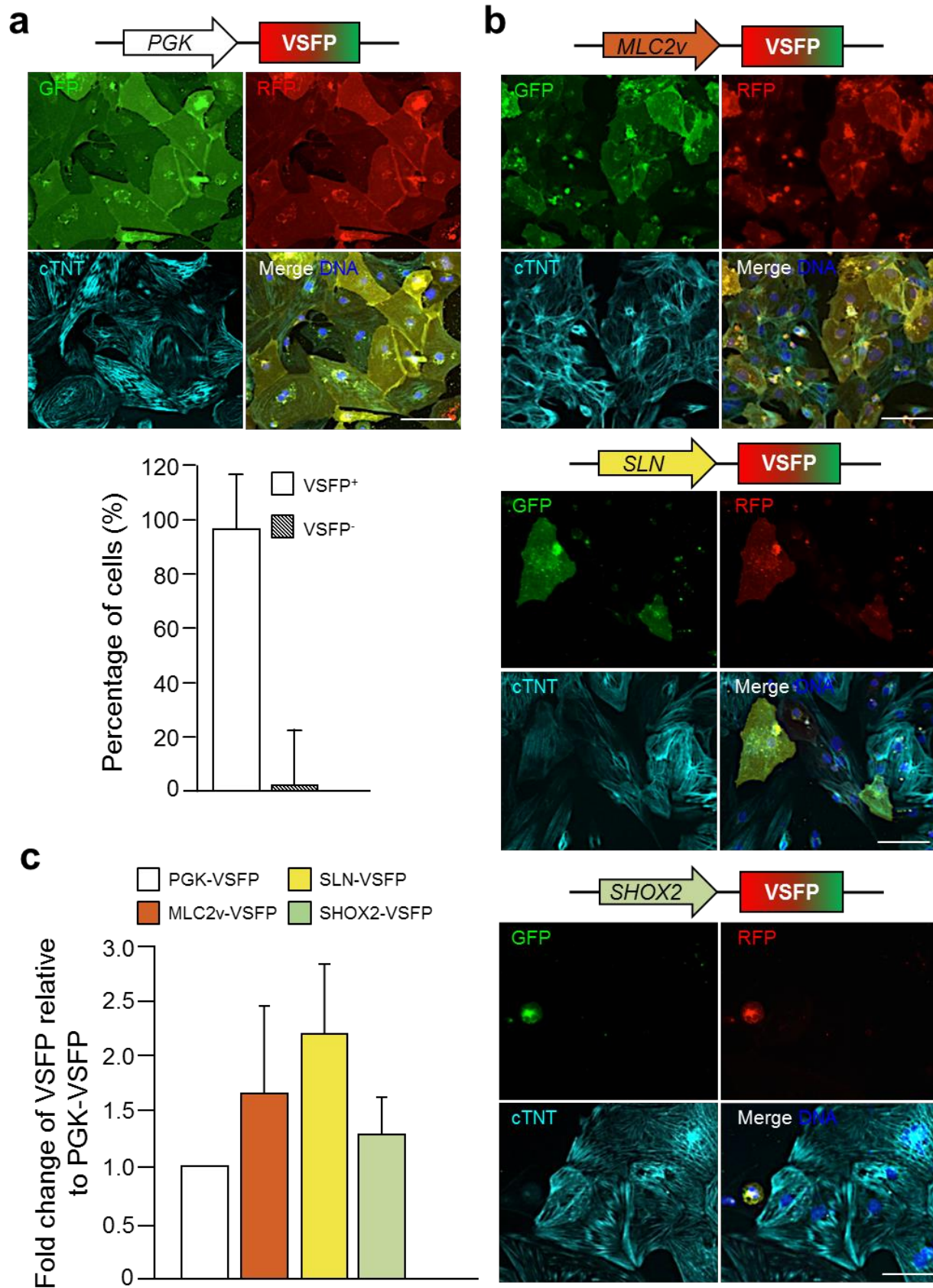


Figure 23: Comparison of transduction efficiency of PGK-VSFP, MLC2v-VSFP, SLN-VSFP and SHOX2-VSFP lentiviruses. (a) Representative images of CMs after 7 days infection with PGK-VSFP lentivirus (top) and quantification of VSFP⁺ and VSFP⁻ cells (bottom). Averaged values \pm 95% confidence intervals of 3 independent experiments are shown. (b) Representative images of CMs after 7 days infection with the different CM subtype-specific lentiviruses, as indicated. GFP (green) and RFP (red) mark cells expressing the VSFP. CMs are labeled by antibody against human cardiac troponin T (cTNT, Abcam). Nuclei are stained by Hoechst dye. Scale bars indicate a length of 50 μ m. (c) Quantitative PCR analysis of the genome-integrated VSFP transgene in CMs after 7 day infection with the different lentiviruses. Values are normalized to GAPDH and relative to PGK-VSFP. Averages \pm 95% confidence intervals of 3 independent experiments are shown²¹⁹.

3.2.2.2 Marking of the ventricular lineage by MLC2v-VSFP

The subtype-specificity of lentivirus-mediated MLC2v-VSFP transgene overexpression was investigated both at the molecular level using immunofluorescence microscopy and at the functional level by patch-clamp AP recordings from VSFP positive cells. The immunocytochemistry results showed that most of MLC2v-VSFP positive CMs expressed MLC2v, the myocardium specific transcriptional factor NKX2.5, and, to a lesser extent, MLC2a. In contrast, neither the atrial-specific sarcoplasmic reticulum (SR) protein sarcolipin, nor the nodal-CM markers SHOX2, HCN4, or podoplanin were found in VSFP-positive cells (Fig 24a, b).

To further evaluate the fidelity of the ventricular voltage sensor, we performed AP measurements using patch clamp in cells exhibiting VSFP fluorescence after infection with MLC2v-VSFP. MLC2v-VSFP positive CMs exhibited ventricular electrophysiological characteristics with fast up-stroke velocity, negative maximum diastolic voltage, as well as a prolonged plateau phase. Subsequent single-cell RT-PCR on the patched cells confirmed ventricular identity at the transcript level by demonstrating the presence of *MLC2v* transcript (Fig 24b).

3.2.2.3 Marking of the atrial lineage by SLN-VSFP

We applied the same procedures to validate the specificity of the atrial hiPSC-CM marking by the SLN-VSFP lentivirus. In addition to MLC2a expression, VSFP-marked CMs were also positive for NKX2.5 and Sarcolipin. However, expression of MLC2v, SHOX2, HCN4 and podoplanin were rarely observed (Fig 25a, b). This was corroborated by the single-cell electrophysiological analysis, showing typical atrial AP properties such as rapid upstroke velocity and lack of plateau phase. Correspondingly, both *MLC2a* and *SLN*, but not *MLC2v* transcript could be amplified from these CMs (Fig 25c).

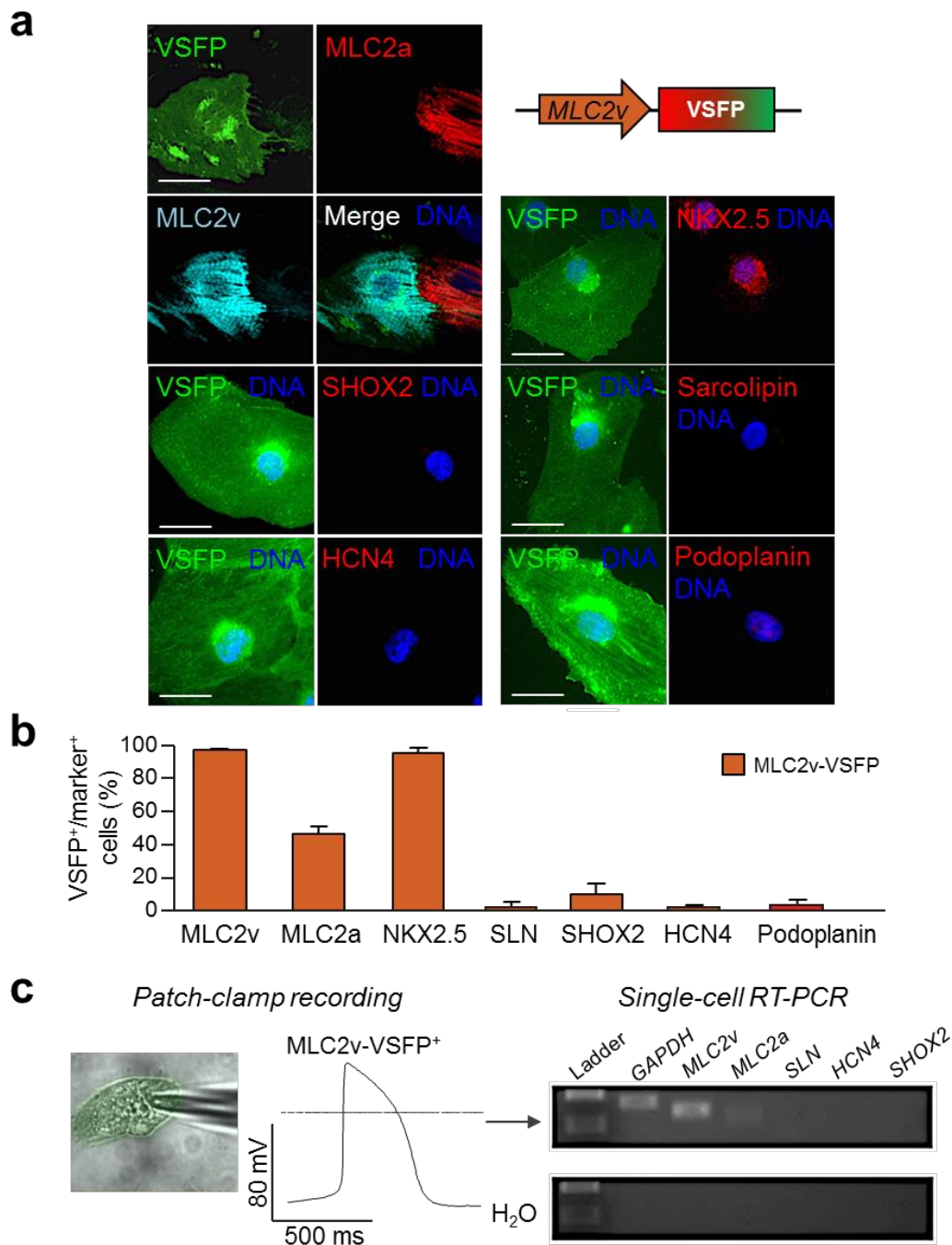


Figure 24: Molecular characterization of cells marked with ventricular membrane potential sensor (MLC2v-VSFP). (a) Cells infected with MLC2v-VSFP lentivirus were stained with antibodies against CM subtype-specific markers as indicated. Typical pseudocolor images are shown. VSFP fluorescence is shown in green, the immunofluorescence signal is shown in red or cyan as indicated, and a DAPI DNA stain is shown in blue. Scale bars indicate a length of 20 μ m. (b) The bar graph shows the percentage of VSFP-positive cells that express the indicated markers. Error bars represent 95% confidence intervals, $n = 169-975$ cells were analysed for each marker. (c) Typical AP recordings from cells marked by MLC2v-VSFP are shown, together with gels illustrating the results of single-cell RT-PCR performed from the same cells²¹⁹.

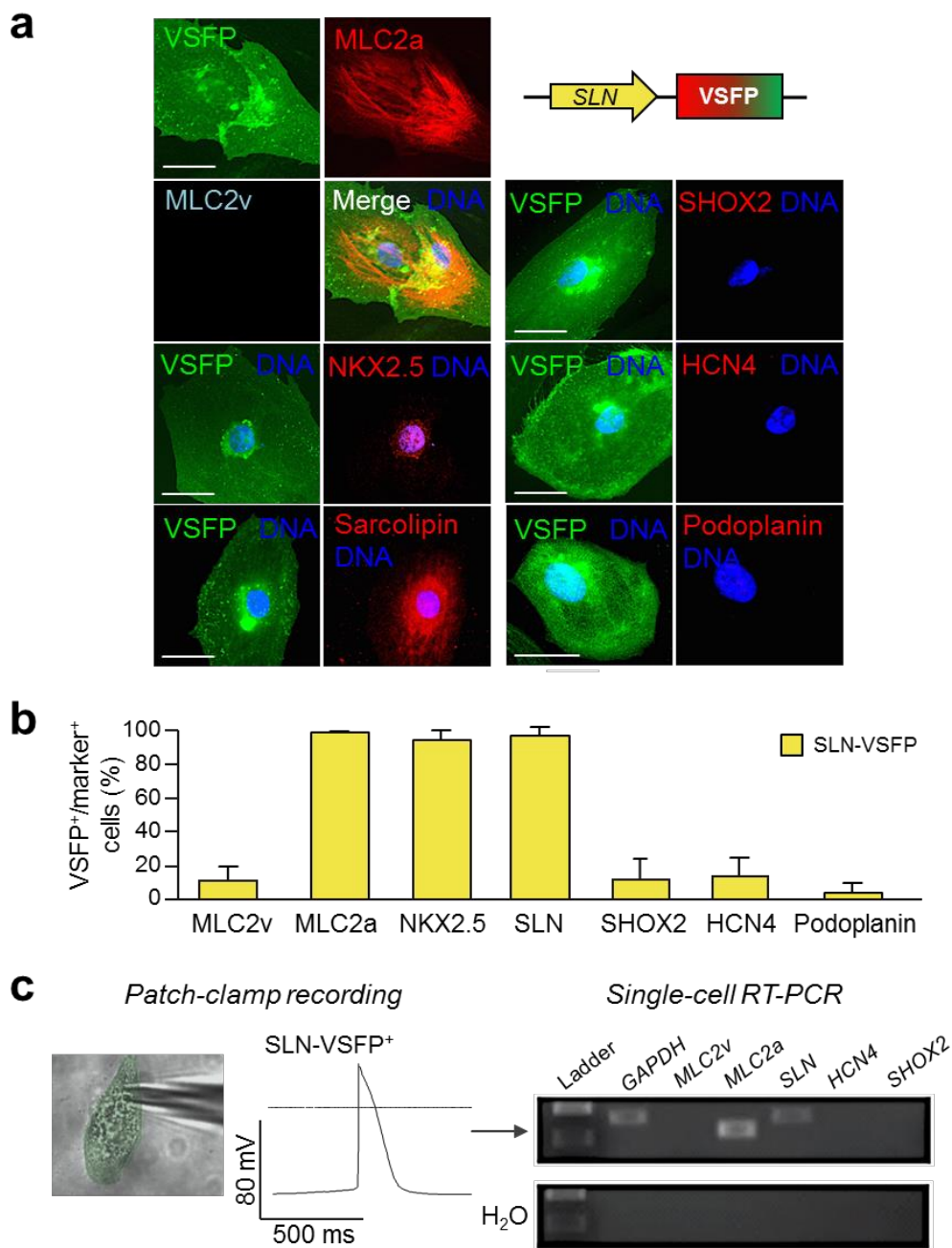


Figure 25: Molecular characterization of cells marked with atrial membrane potential sensor (SLN-VSFP). (a) Cells infected with SLN-VSFP lentivirus were stained with antibodies against CM subtype-specific markers as indicated. Typical pseudocolor images are shown. VSFP fluorescence is shown in green, the immunofluorescence signal is shown in red or cyan as indicated, and a DAPI DNA stain is shown in blue. Scale bars indicate a length of 20 μm . (b) The bar graph shows the percentage of VSFP-positive cells that express the indicated markers. Error bars represent 95% confidence intervals, $n = 169\text{-}975$ cells were analysed for each marker. (c) Typical AP recordings from cells marked by SLN-VSFP are shown, together with gels illustrating the results of single-cell RT-PCR performed from the same cells²¹⁹.

3.2.2.4 Marking of the nodal lineage by SHOX2-VSFP

The confirmation of nodal-specific CMs marking with the SHOX2-VSFP lentivirus was performed in analogy to the other two reporters. In immunostaining, SHOX2-VSFP labeled CMs co-stained for SHOX2, HCN4, podoplanin, and MLC2a, while MLC2v, NKX2.5 and Sarcolipin were absent (Fig 26a, b). Consistently, the cells had a typical nodal-like electrical phenotype (i.e., spontaneous diastolic depolarization and slow upstroke velocity) and expressed HCN4 and SHOX2 at a single-cell level (Fig 26c).

3.2.2.5 Functional validation of CM subtype-specific voltage sensor constructs

To test the function of the three subtype voltage sensors, optical AP recordings were conducted in CTR2 hiPSC-CMs 7 days after infection with the respective subtype-specific lentivirus construct. Measurements were performed both in spontaneously beating cells and under external field stimulation. Optical AP recordings could be made with all subtype-specific sensors under both conditions. Under spontaneous beating, SHOX2-VSFP marked CMs that not only exhibited the fastest beating rate as compare to the other two sensors, but also displayed prominent spontaneous diastolic depolarization (Fig 27a, b, c), which is a typical finding in adult sinus node. Moreover, compared to SLN- and SHOX2-VSFP positive CMs, myocytes labeled by MLC2v-VSFP had larger APD_{50} and APD_{90} values, but a smaller APD_{90} / APD_{50} ratio under pacing at 1Hz, which is in good agreement with previously-reported results measured by both MEA²²⁹ and patch clamp recordings³³ (Fig 27d,e). Similar results were obtained in 3-month-old CMs derived from three additional unrelated healthy control hiPSC lines, which were generated by either retrovirus- or sendai virus-mediated reprogramming of dermal fibroblasts or keratinocytes (Fig 28). Thus, our genetic marking approach seemed effective and independent from genetic background-related variations or reprogramming methods.

Since molecular and electrophysiological maturity as well as subtype distribution of iPSC-derived CMs may vary depending on the cardiac differentiation protocol used, we next validated our subtype-specific membrane potential indicator constructs in hiPSC-CMs obtained with a chemically-defined monolayer differentiation protocol (Fig 29b, c), which has been reported to yield up to 95% cardiac troponin T-positive cells, predominantly with a ventricular phenotype¹⁴⁹. Consistently, more than 90% of CMs generated with such protocol expressed MLC2v-VSFP, only ~4% were positive for SLN-VSFP, and even less (~1%) were labelled by the SHOX2 reporter (Fig 29b). Moreover, APD_{50} and APD_{90} values measured in 3-month-old MLC2v-VSFP+

cells were comparable to those obtained in EB-differentiated MLC2v-VSFP+ CMs from the same iPSC line (Fig 29c). These findings support the specificity of our genetic marking strategy and at the same time indicate a similar level of cellular maturation of the ventricular lineage in CMs generated by the two differentiation protocols.

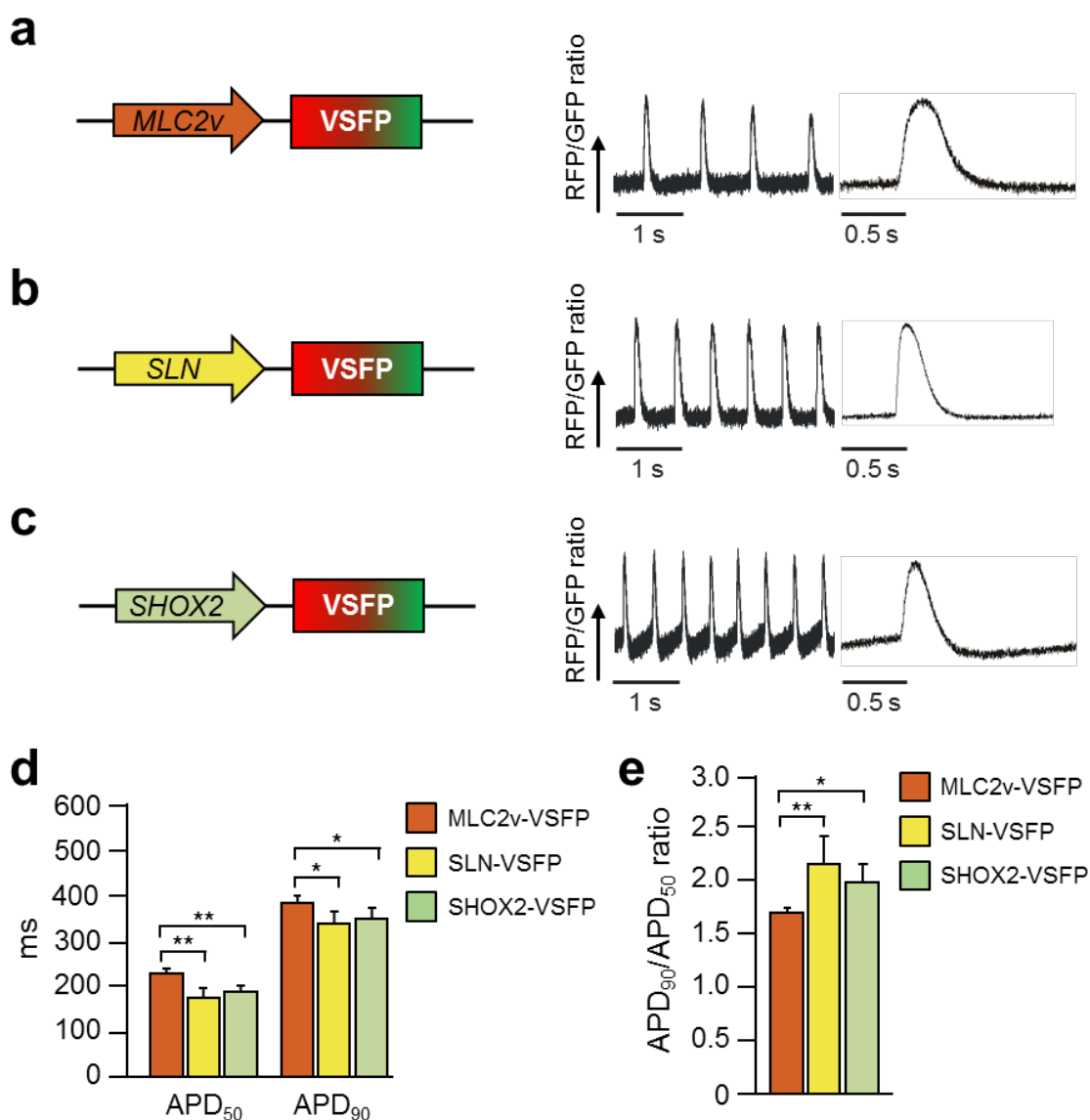


Figure 27: Functional characterization of cells marked with subtype-specific membrane potential sensor constructs. (a-c) Typical optically-recorded trains of APs measured in spontaneously-beating hiPSC-CMs using MLC2v-VSFP (a) SLN-VSFP (b) or SHOX2-VSFP (c) are shown, together with an averaged signal from 6-8 subsequent APs. (d-e) Bar graphs showing AP duration (APD₅₀ and APD₉₀) of repolarization (d) as well as the APD₉₀/APD₅₀ ratio (e). Error bars represent 95% confidence intervals, n=39-57 cells per group; *p<0.05, **p<0.01

Taken together, these results indicate that our system combining FRET-based VSFP and CM subtype-specific promoters allows selective optical AP measurements in ventricular-, atrial- or nodal-like hiPSC-derived CMs.

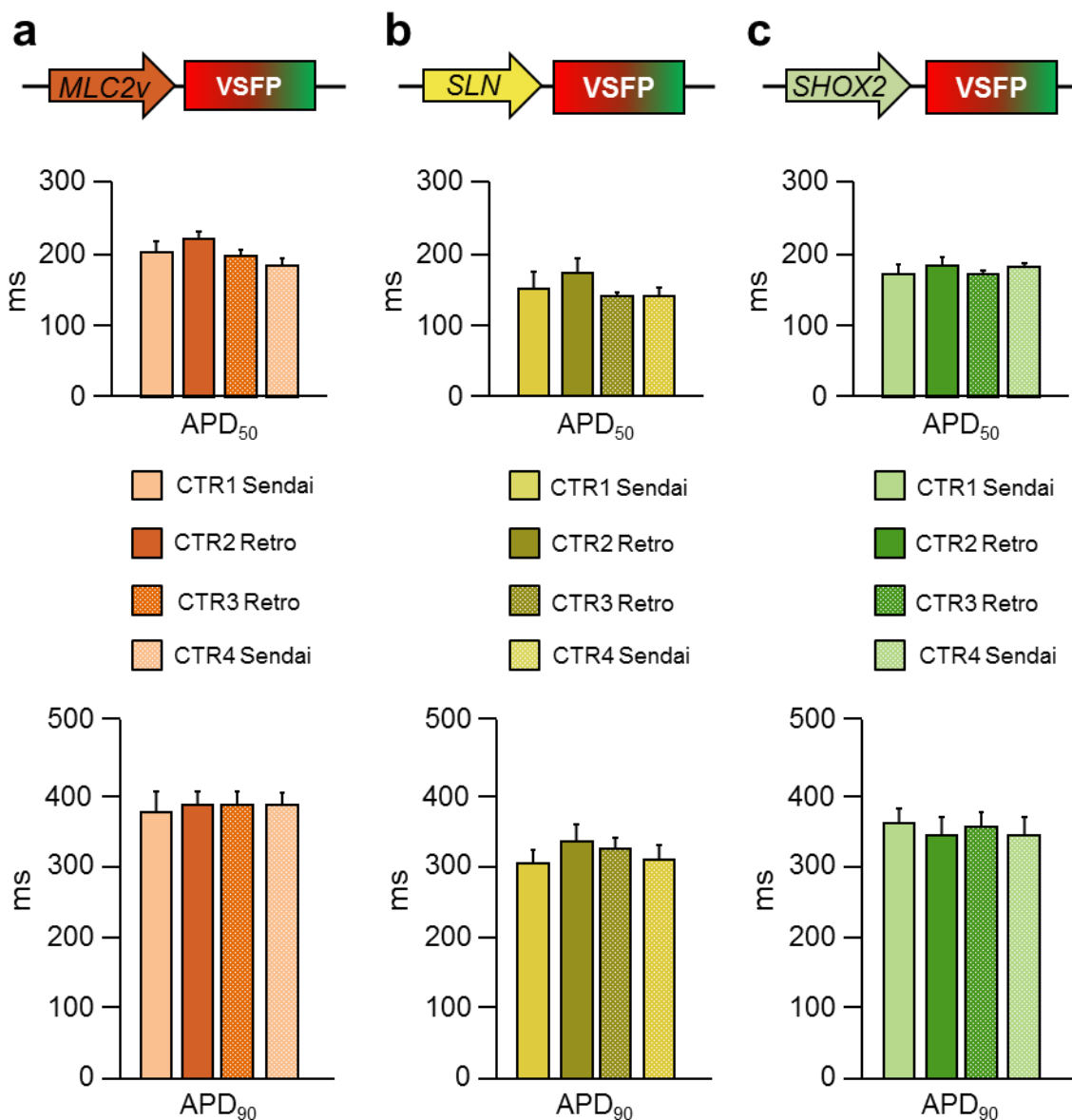


Figure 28: Consistency of VSFP based optical recording among various healthy control iPSC lines obtained with different reprogramming methods. APD₅₀ and APD₉₀ of CMs from 2 lines generated by retrovirus-mediated reprogramming of dermal fibroblasts (CTR2 Retro and CTR3 Retro) and 2 lines generated by sendai virus-mediated reprogramming of dermal fibroblasts (CTR1 Sendai) or keratinocytes (CTR4 Sendai) were compared after infection with MLC2v-VSFP (a), SLN-VSFP (b), and SHOX2-VSFP (c) lentiviruses. CTR2 is the control line majorly used in the study. Error bars represent 95% confidence intervals, n=27-57 cells per group²¹⁹.

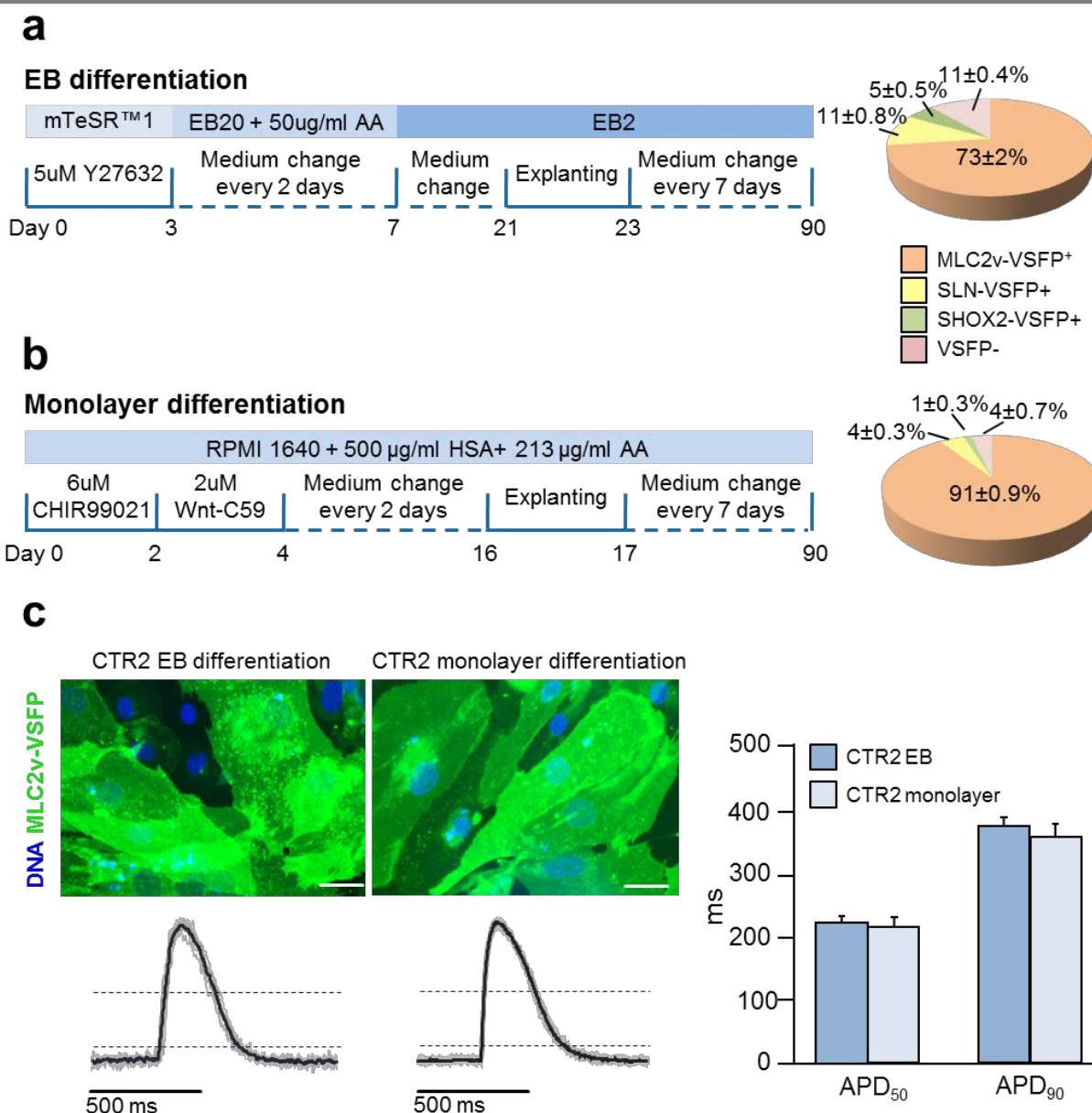


Figure 29: Comparison of CM subtype-specific VSFP-based optical recording in CMs differentiated by EB and monolayer protocols. (a) Scheme of EB differentiation protocol and corresponding average detected percentages of ventricular, atrial and nodal sensor positive CMs from 3 independent differentiation experiments (n=221-325 cells, per group in each experiment). AA, ascorbic acid; EB20, differentiation medium with 20% FBS; EB2, differentiation medium with 2% FBS, as in ³³. (b) Diagram of monolayer differentiation protocol, as reported in ²³, and resulting average percentage of the three cardiac subtypes probed by MLC2v-VSFP, SLN-VSFP and SHOX2-VSFP, respectively (n=302-376 cells, per group in each experiment). rHA, recombinant human albumin. (c) Representative images of CMs obtained with the EB (left) and monolayer (right) differentiation protocols after infection with the MLC2v-VSFP sensor (green). Nuclei are stained by Hoechst dye. Scale bars indicate a length of 20 µm. Below, averaged AP traces from a representative cell from each protocol are shown. The dashed lines at 50% and 10% of AP amplitude indicate where APD₅₀ and APD₉₀ were measured. Bar graph indicates average APD₅₀ and APD₉₀ values detected by the MLC2v-VSFP voltage sensor in CMs generated with both protocols (Error bars represent 95% confidence intervals; n=102 and 98 cells for the EB and monolayer groups, respectively, from 3 independent experiments) ²¹⁹.

3.2.3 Modelling of Long QT syndrome type 1 using subtype-specific optical AP imaging of patient iPSC- CMs

3.2.3.1 Modelling of LQT1 syndrome with patient specific- and isogenic hiPSC-CMs

Congenital LQT syndromes, clinically characterized by QT interval prolongation in ECG, are most frequently caused by mutations in genes encoding cardiac ion channels. The most frequent LQT type 1 is associated with mutations of the *KCNQ1* gene, which encodes the α subunit of the potassium channel responsible for the I_{KS} current. We investigated the suitability of our subtype-specific optical AP recording system to study the electrophysiological effects of a heterozygous missense c.569G>A (p.R190Q) *KCNQ1* mutation in hiPSC-CMs generated from a LQT1 patient. Previous studies using conventional patch clamp electrophysiology had revealed that the patient-derived LQT1 hiPSC-CMs exhibited prolonged APs and an increased frequency of occurrence of early afterdepolarizations (EADs)³³.

In order to explore the potential application of VSFP-based subtype-specific optical AP recording in investigating the phenotype of diseased iPSC-CMs and eventually discriminate subset phenotypes in the 3 major CM subtypes, we used the three subtype-specific sensor constructs to perform optical AP imaging on CMs differentiated from the LQT1 hiPSCs. As control, in addition to the previously-described hiPSC line (CTR2) obtained from an unrelated healthy volunteer without any cardiac disease³³, our cooperation partners generated an isogenic line (LQT1^{corr}) by correcting the *KCNQ1*-R190Q mutation in the patient LQT1 hiPSCs by classical homologous recombination (Fig 30a-d). The use of this additional isogenic control allowed us to eliminate effects of individual genetic background variability²⁵ and test whether the optical VSFP sensors could discern the net contribution of the disease-causing mutation to the LQT1 phenotype.

3.2.3.2 Discrimination of LQT1 phenotypes in hiPSC-CM subtypes

Given the fact that ventricular arrhythmias (e.g. torsade's de pointes) are the most important clinical consequence of LQT1 syndrome, we initially used the ventricular-specific voltage sensor to record APs from the CMs derived from the three iPSC lines. In the LQT1 iPSC-CMs, both prolonged AP durations (APD₅₀ and APD₉₀) and increased incidence of EADs as compare to that of CTR2 iPSC-CMs were visualized (APD₉₀ 616 ± 147 ms vs 382 ± 62 ms; p<0.01; n= 72 vs 57 cells; Fig 31a). Moreover, smaller, but still significant differences in both AP duration and

EAD occurrence were also observed between LQT1 cardiomyocytes and the isogenic controls (APD₉₀ 474 ± 90 ms; p<0.01; n=102 cells; Fig. 31b).

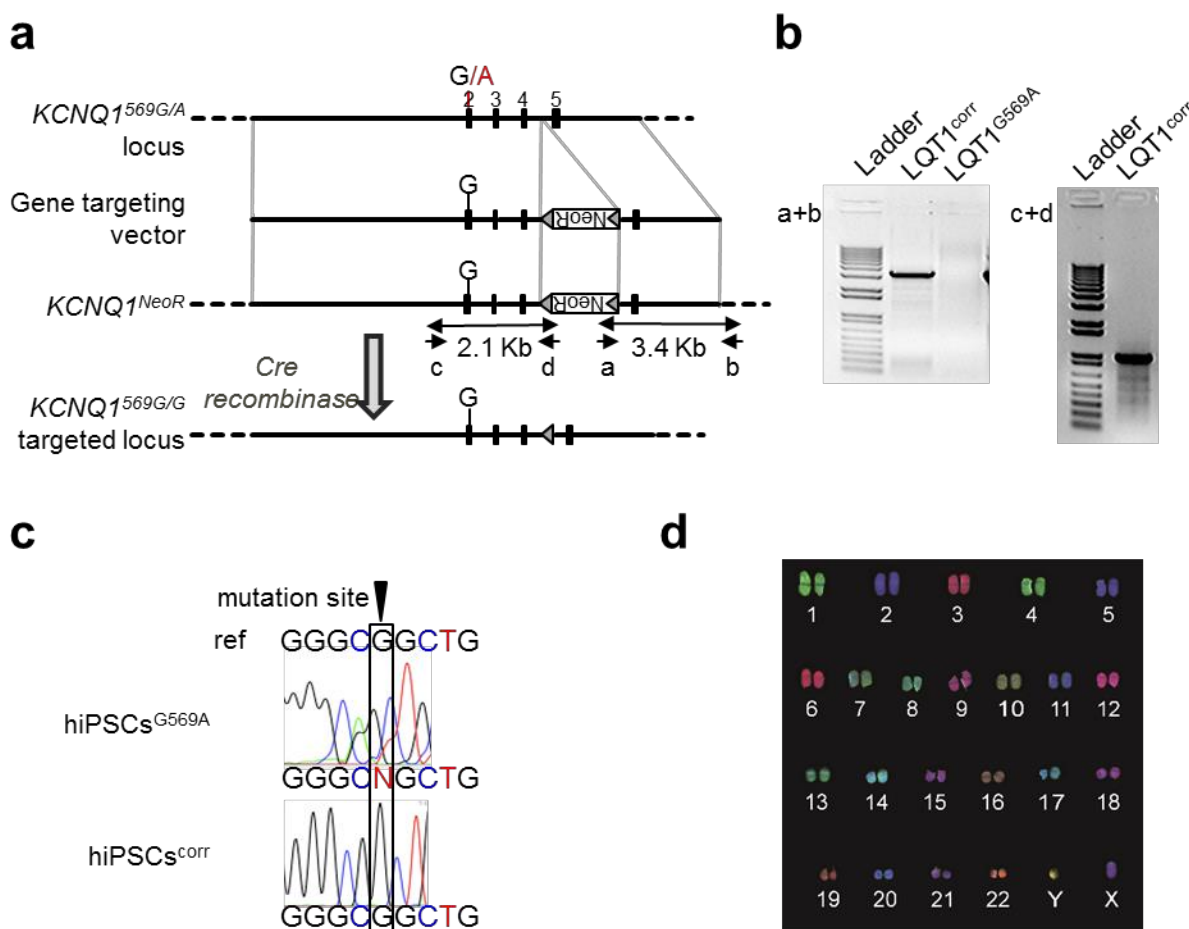


Figure 30: Generation of isogenic hiPSC line by correcting c.569G>A (p.R190Q) KCNQ1 mutation in LQT1 hiPSCs. (a) Schematic of the gene targeting strategy applied to correct the disease-causing c.569G>A (p.R190Q) KCNQ1 mutation in hiPSCs obtained from a patient affected by LQT1. **(b)** PCR using primers a+b (3.4 kb) was performed to identify targeted clones while PCR using primers c+d (2.1 kb) followed by sequencing allowed identification of corrected clones. **(c)** Results of Sanger sequencing showing correction of the disease-causing mutation in the clonally isolated LQT1^{corr} line. **(d)** The karyotype of the LQT1^{corr} hiPSC line is normal²¹⁹.

AP recordings using the atrial-specific SLN-VSFP sensor construct showed the same phenotype of APD prolongation and EAD prevalence in LQT1 CMs as compared to LQT1^{corr} and CTR2 lineages. By contrast, when the nodal-specific SHOX2-VSFP sensor was used, AP durations were fairly similar among the three lines (Fig. 31c). These differences of LQT1 disease phenotypes between cells marked by the myocardium-specific voltage sensors (MLC2v- and SLN-VSFP) and the nodal-specific SHOX2-VSFP sensor can be explained by the fact that nodal myocytes do not express the *KCNQ1* gene³³. Altogether, upon CM subtype

specific AP recordings, disease phenotypes could be precisely characterized in distinct subset of myocytes, which was additionally assisted by the generation of isogenic cell line to designated specific phenotype to the disease causing mutation in the particular myocyte subtypes.

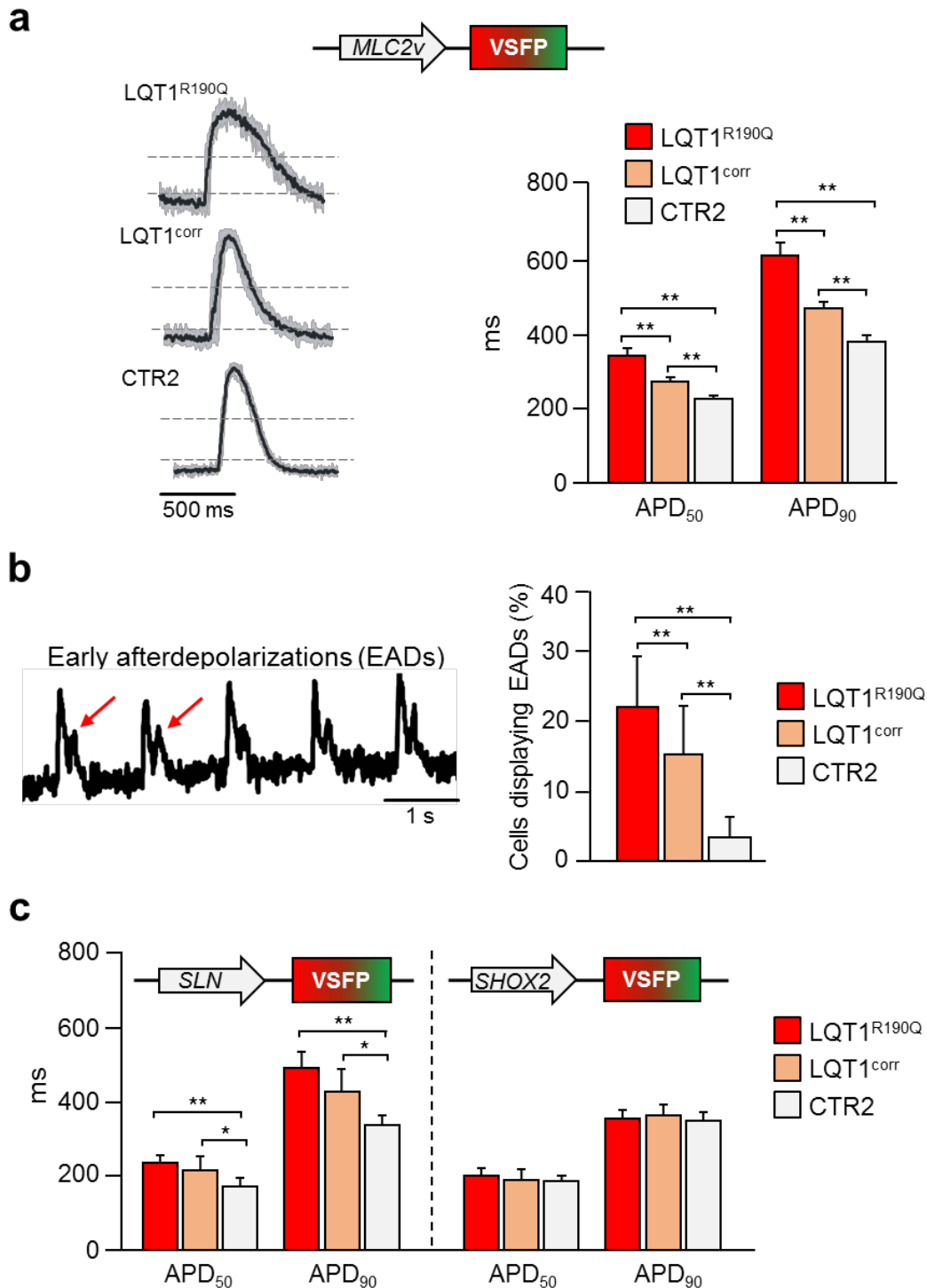


Figure 31: Modeling long-QT syndrome using subtype-specific optical action potential recordings. Optical AP recordings were performed in CMs generated from the patient-derived LQT1 hiPSC (LQT1^{R190Q}), the isogenic control (LQT1^{corr}), and a hiPSC line derived from an unrelated healthy individual (CTR2) infected with MLC2v-VSFP (**a, b**), SLN-VSFP, or SHOX2-VSFP (**c**) as indicated. The cells were field-stimulated at 1 Hz. (**a**) Typical optical AP traces are shown. The grey lines show single APs, the superimposed black lines show the average, which was used to calculate AP duration (APD₅₀ and APD₉₀). The dashed lines at 50% and 10% of AP amplitude indicate where APD₅₀ and APD₉₀ were shown. The bar graph shows APD₅₀ and APD₉₀ values in the three lines (n=57-72 cells per group). (**b**) An example of a membrane potential tracing showing early afterdepolarizations (EADs). The bar graph shows the percentage of cells exhibiting EADs in the different lines (n=57-72 cells per group). (**c**) The bar graph shows APD₅₀ and APD₉₀ values in the three lines investigated using SLN-VSFP and SHOX2-VSFP as indicated (n=20-65 cells per group). Error bars represent 95% confidence intervals. * p<0.05; ** p<0.01²¹⁹.

3.2.4 Long-term monitoring of AP dynamics in hiPSC-CMs with MLC2v-VSFP sensor

3.2.4.1 Probing the genetic rescue of the LQT1 disease phenotype in single patient iPSC-CMs by serial AP recordings

In contrast to the invasive patch clamp method, the nondestructive nature of optical AP recording allows repeated membrane voltage imaging in the same cells over time. We highlighted this advantage by analyzing the reversion of the APD-prolonging effect of the LQT1-KCNQ1 mutation through AAV6-mediated overexpression of wild type (wt) KCNQ1. Because KCNQ1 proteins function as tetramers, the defective repolarization in LQT1 is often caused by a dominant-negative effect of the KCNQ1 mutants. Specifically, the mutated R190Q-KCNQ1 gene encodes a trafficking-deficient ion channel subunit that interacts with wild type subunits and interferes with their integration into the plasma membrane³³. Therefore, we hypothesized that upon wt *KCNQ1* overexpression, the defect would be attenuated or even corrected by allowing sufficient wt *KCNQ1* subunits to target the plasma membrane. We generated AAV constructs in which the wt *KCNQ1* was tagged with the HA epitope at its N terminus (*wt KCNQ1*-HA) to facilitate subsequent transgene identification. As a negative control, AAV encoding transgenic *LacZ* was used (Fig 32a). Optical AP imaging was first performed at day 7 after MLC2v-VSFP lentiviral transduction. Immediately after the recordings, the cells were infected with wt KCNQ1-HA or control AAV. Three days later (day 10), the same cells again underwent optical AP imaging to detect the effect of wt-KCNQ1 overexpression (Fig 32b, c). Comparison of APDs of LQT1 CMs imaged at days 7 and 10 showed shortened APD₅₀ and APD₉₀ in cells infected with the wt KCNQ1-HA AAV, but no alterations were found in the control experiment. APD₅₀ and APD₉₀ of the LQT1 CMs were reversed to similar durations as in LQT^{corr} CMs (Fig 32d, e).

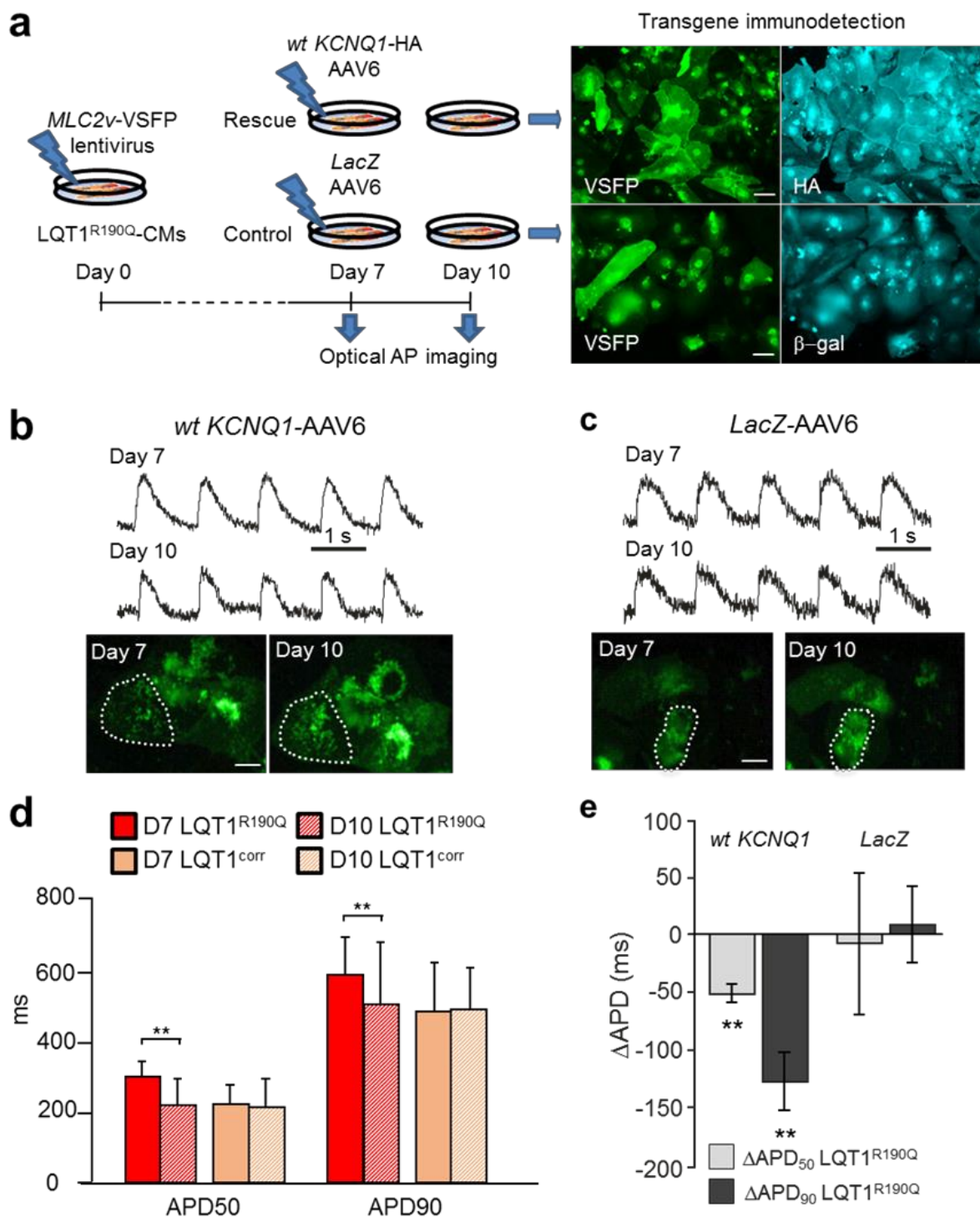


Figure 32: Long-term measurements of dynamic AP changes: genetic rescue of LQT1 phenotype. (a) A scheme of the rescue experiment is shown. LQT1^{R190Q} CMs were infected with the MLC2V-VSFP lentivirus at day 0. At day 7, APs were optically recorded. Then, the cells were infected with an adeno-associated virus (AAV6) encoding either HA-tagged wild-type *KCNQ1* (rescue group) or *LacZ* (control group). At day 10, APs were again optically recorded from the same cells. After completion of the membrane potential recordings, the cells were

stained for the presence of the HA tag or the b-gal transgene. **(b-c)** Typical optical AP tracings obtained from cells from the wild-type KCNQ1 **(b)** and control group **(c)** at day 7 and at day 10 are shown. The images show VSFP green fluorescence from the same group of cells at the two indicated time points. The dotted line shows the region of interest from which the fluorescence signal over one cell was quantified. **(d)** Average AP duration (APD₅₀ and APD₉₀) of LQT1 and LQT1^{corr} CMs in the rescuing experiment at day 7 and 10 are compared. Error bars represent 95% confidence intervals, n=103-126 cells per group; **p<0.01. **(e)** The difference in AP duration (Delta APD₅₀ and Delta APD₉₀) at day 10 compared to day 7 is shown. Error bars show SEM, n=103-126 cells²¹⁹.

To confirm expression of the transgenes introduced by AAV infection, immunodetection of HA epitope and beta-gal was performed immediately after the second AP monitoring at day 10. The results of immunocytochemistry assay of the imaged plates showed highly-efficient membrane localization of HA epitope and cytosolic accumulation of beta-gal. Importantly, nearly all the VSFP positive CMs were positive for wt KCNQ1-HA or LacZ, indicating high transduction efficiency (Fig 32a). These results show that sequential AP imaging in the same cells using the MLC2v-VSFP sensor is possible, allowing detection of a successful rescue of the LQT1 phenotype in patient specific hiPSC-CMs.

3.2.5 Investigation of drug effects by CM subtype-specific sensors

To evaluate whether VSFP-based optical AP recordings may be used as tools for toxicity testing and cardiac candidate drug screening in hiPSC-CMs, we investigated the effects of two drugs, namely cisapride and ivabradine, which are functionally well defined. Each drug was applied on hiPSC-CMs for 10 min and optical AP imaging was performed before and after drug treatment. Solvent only was administered in the parallel control experiments (Fig 33a).

3.2.5.1 Evaluation of cisapride drug effects using the PGK-VSFP sensor

Cisapride (Fig 33b), an antiemetic drug, was commercially available over a decade, but withdrawn from the market due to its potential to prolong the QT interval in patients, increasing the risk of arrhythmias and sudden cardiac death. Its mechanism was afterwards identified as inhibition of the hERG channel, which is one important potassium channel responsible for the repolarization phase of the cardiac AP in human heart. In an attempt to investigate this side effect of cisapride in hiPSC-CMs, we applied 100 nM drug to LQT1, LQT1^{corr} and CTR2 iPSC-CMs expressing PGK-VSFP and imaged APs before and 10 min after treatment. PGK-VSFP based optical AP recording was sufficient to detect cisapride-induced prolongation of APD₅₀ and APD₉₀ as well as elicitation of EADs in all the three tested cell lines (Fig 33c, d). Importantly, the

most dramatic pro-arrhythmic effects were observed in the mutated LQT1 CMs: many cells stopped beating upon cisapride treatment while few survivors developed extremely long APD₅₀ and APD₉₀ (369 and 652ms, respectively) and high occurrences of EAD as 44% (Fig 33c, d). These findings explain the overlooked cardiotoxicity of cisapride on patients with pre-existing heart disease and highlight the value of a more accurate toxicity evaluation in human target cells during preclinical pharmacological development.

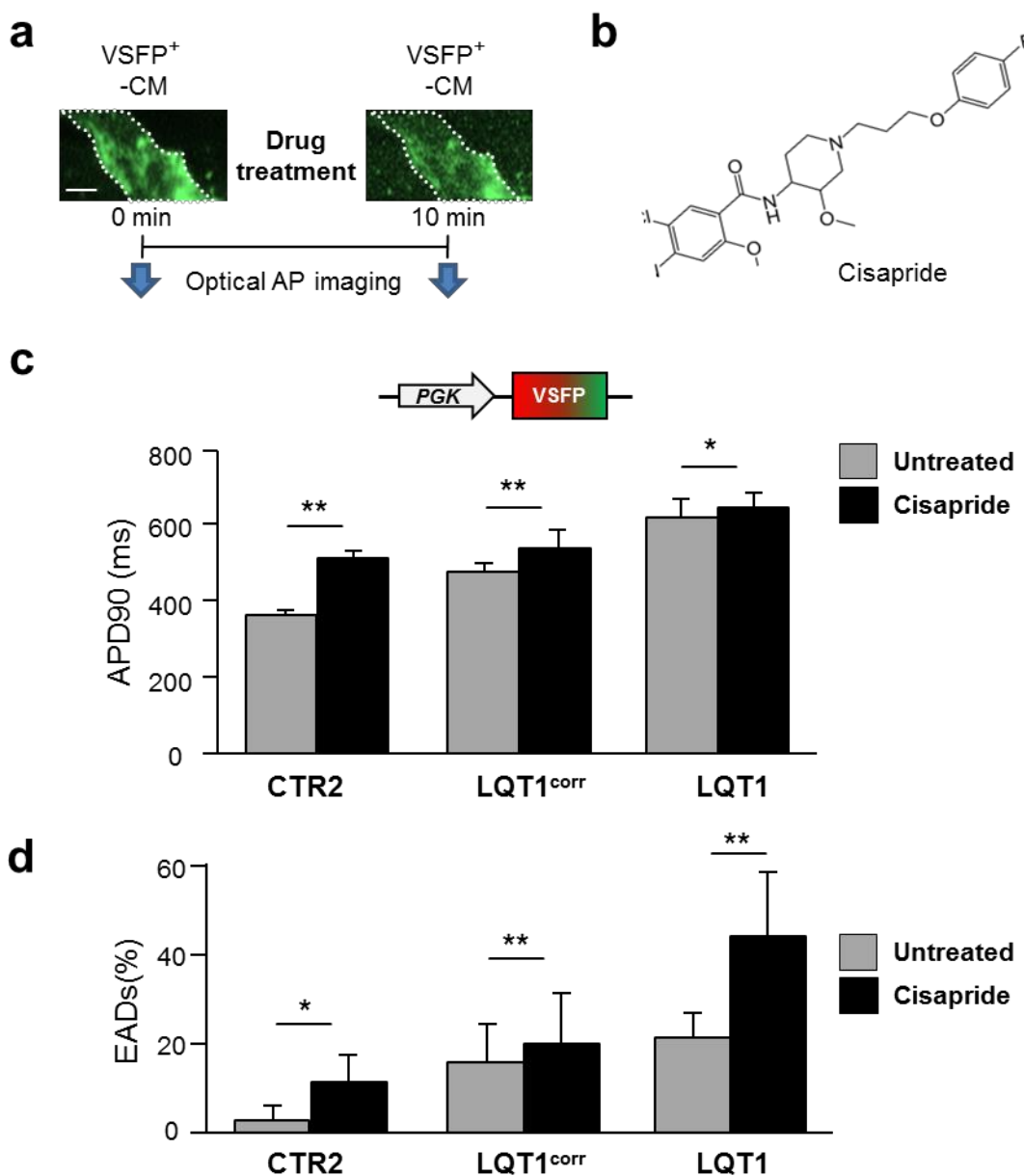


Figure 33: Optical investigation of drug-induced effects in healthy and LQT1 hiPSC-CMs. (a) A scheme of the drug treatment. Control CMs infected with PGK-VSFP were imaged before and after 10 minutes of drug application. (b) Chemical structure of Cisapride. APD₅₀ and APD₉₀

To test this hypothesis, we repeated the measurements using the three subtype-specific sensors to probe the effect of the drug on the different subtypes of hiPSC-CMs. Indeed, a significant reduction of the spontaneous beating rate was seen in CMs imaged by SHOX2-VSFP (Fig 34c). By contrast, the beating rate of CMs imaged by MLC2v-VSFP and SLN-VSFP was not altered (Fig 34c). These experiments highlight the superiority of applying a subtype-specific voltages sensor on investigation of drug effects that affect distinct CM subtypes, especially when reliable differentiation protocols for cardiac lineage specification are still under development.

Part 4 Discussion

To date, cardiomyocytes derived from healthy and diseased hiPSCs are increasingly used to model cardiac diseases, and hold promise for cardiac drug development, toxicological investigation and regenerative medicine. The focuses of this work were to model cardiac diseases, investigate therapeutic approaches and establish a type of high throughput tools for probing cardiac electrophysiological phenotypes, utilizing patient-specific iPSC-CMs. Two monogenic diseases were approached by an iPSC-based modeling strategy: familial dilated cardiomyopathy (DCM) caused by truncating mutations in the *TTN* gene and long-QT syndrome type 1 (LQT1), an early-onset channelopathy due to mutations in the *KCNQ1* gene. Patient specific hiPSC-CMs were used to investigate molecular mechanisms and potential therapeutic strategies of *TTN*-based DCM and to analyze the arrhythmogenic phenotypes of a R190Q-*KCNQ1* mutation associated with LQT1. In the DCM hiPSC model, we tested an RNA-based antisense approach to partially reverse the cellular DCM phenotype by skipping the mutated exon; the positive obtained results suggest the potential of this strategy as effective therapy for this particular and other similar genetic diseases. In the LQT1 hiPSC model, an isogenic hiPSC line (LQT1^{corr}) was generated to discern the net contribution of the R190Q-*KCNQ1* mutation to the disease phenotype; correction of the mutation did not completely rescue LQT1 in patient cells, indicating a role of the genetic background in the disease manifestation and the superiority of isogenic controls in hiPSC-based modelling. Furthermore, this work addressed the question of phenotyping the heterogeneous population of hiPSC-CMs by using a combination of a genetically-encoded optical membrane potential sensor with a promoter-driven genetic marking for recording APs in a subtype-specific manner. The efficacy of the CM-subtype specific phenotyping strategy was tested in the same LQT1 iPSC model and its consistency was evaluated in hiPSC-CMs obtained with both EB and monolayer differentiation protocols. The optical AP recording method not only increased the throughput far beyond that of single-cell patch clamp electrophysiology, it also allowed sequential investigation of the same cells over extended time periods during genetic and drug-induced manipulation of AP dynamics.

4.1 Recapitulation and rescue of DCM and LQT1 phenotypes in hiPSC-CMs

4.1.1 RNA-based therapy reversed defects of TTN-based DCM in patient hiPSC-CMs

4.1.1.1 hiPSC-derived cardiomyocytes as a human model for hereditary DCMs

Dilated cardiomyopathy is a disease characterized by dilation of the cardiac cavities and a reduced systolic function. Approximately 30% of all DCM cases can be linked to a genetic cause, with *TTN* mutations responsible for most cases⁵⁵. The DCM-causing *TTN* mutations are enriched in the A-band region of the protein (Fig 6) and most of them result in the translation of a truncated product lacking both part of the A band, which is connected to the myosin filament, and the M-band, which encompasses a tyrosine kinase (TK) domain as well as docking sites for interacting proteins including cytoskeleton components, signaling molecules and protein turnover regulators^{55,83,212}.

Current knowledge on the precise biological abnormalities that results from specific *TTN* mutations and on the pathophysiological processes that ultimately result in the DCM disease phenotypes is limited. This is partially related to the fact that, due to its huge size (over 35,000 aminoacids), any biochemical and physiological investigation of titin has been challenging; moreover, access to patient myocardium is rare. Cardiomyocytes generated from patient-specific hiPSCs are a promising new tool to overcome some of these limitations.

In the DCM patient-specific iPSC-CMs carrying a Ser14450fsX4 *TTN* mutation, we confirmed the expression of truncated A-band TTN and observed defects in building and maintaining a stable sarcomeric structure (Fig 13); these structural abnormalities correlated with perturbations in the interaction between the Nbr1/p62/SQSTM1/MURF2 signalsome and the TK domain, resulting in a reduction of cardiac muscle gene expression by SRF and MURF2 (Fig 14). Since the Nbr1/p62/SQSTM1/MURF2 complex is known to regulate both SRF transcription activity and protein turnover pathways (ubiquitin-proteasome and autophagy-lysosomal pathways)^{61,212}, both mechanisms are likely to play a role in the myofibril phenotype of DCM iPSC-CMs.

Moreover, given that the Ser14450fsX4 mutation leads to the loss of more than half of the A-band and the entire M-band, mutated titin may be impaired in its capacity of acting as a

sarcomeric scaffold mediating binding to the thick filaments and to other sarcomere interacting proteins, which will also result in myofibril defects.

4.1.1.2 AONs mediated exon skipping as a therapy for familiar DCM

In this study, we used a RNA-based strategy to mend the phenotypic effects of the A-band truncating Ser14450fsX4 mutation in *TTN* exon 326. Antisense oligonucleotides (AONs) were designed to interfere with the RNA splicing machinery in such a way that the mutation-carrying exon 326 is omitted from the mRNA. The idea was that a *TTN* transcript lacking the symmetric exon 326 will not contain any frameshift and would result in a titin protein that, although internally deleted, will include the native C-terminal region with the M-band and the TK domain, thus being likely more functional than the A-band-truncated product.

Indeed, we could show that the exon skipping strategy ameliorated the DCM disease phenotype at both structural and functional levels in patient-specific DCM iPSC-CMs. Specifically, our results indicate that, while exclusion of exon 326 from *TTN* mRNA had a negligible effect on myofilament structure in control hiPSC-CMs, it enhanced assembly and stability of myofibrils and normalized muscle gene expression in patient DCM cells. Of note, in a parallel study conducted by our collaborators, the exon skipping approach was able to rescue the DCM phenotype in homozygous and heterozygous knock-in mice of the same *TTN* truncating mutation carried by the patient iPSCs²¹⁶.

Although exon 326 is the largest exon of *TTN*, it mainly consists of repetitive Ig and FN III motifs also present in other exons of this protein, which may explain the observation that its excision is well tolerated in the in vitro (hiPSC-CM) and in vivo (mouse) models. Out of the 69 reported DCM-correlated *TTN* mutations, 14 are located in exon 326⁸³. Therefore, skipping of exon 326 could be a therapeutic approach for approximately 20% of DCM-causing *TTN* mutations. It is noteworthy that exon skipping in *TTN* also occurs as part of normal physiology, modulating the fractional incorporation of tandem-Ig and PEVK (a region rich in proline, glutamate, valine and lysine) motifs, and thereby influencing myofibril elasticity²³¹.

It is possible that not all DCM-associated genetic or pre-mRNA splicing alterations are amenable to exon skipping in a similar way. Thus, the patient-specific iPSCs might offer an effective screening platform for effects of exon skipping in mending the DCM phenotype caused by various genetic variants or mutations located at distinct exons of the *TTN* gene or associated regulatory genes¹⁵. In the corresponding mouse study²¹⁶, *in vivo* exon skipping was

accomplished by systemic delivery of vPMO-AONs. The vPMO modification and alternative chemistry approaches are extensively investigated and becoming safer and more efficient, opening possibilities for future therapeutic applications in human patients²³².

RNA antisense drugs against other diseases (myotonic dystrophy, Fukuyama congenital muscular dystrophy and Huntington's disease) are in the preclinical development process and showed promising therapeutic effects in animal models. Some *in vitro* studies have indicated that dysferlinopathy is also a potential target for antisense therapy²³³. Recently, Ionis Pharmaceuticals has launched clinical trials using an antisense oligonucleotide treatment for spinal muscular atrophy and amyotrophic lateral sclerosis. Moreover, the use of AON-mediated exon skipping as a promising therapeutic approach is further encouraged by the positive results of recent phase 2/3 clinical trials for treatment of Duchenne muscular dystrophy, a disorder of skeletal muscles caused by mutations in the giant scaffold protein dystrophin^{234,111,108}. These examples show that a clinical application of RNA-based therapies for genetically-caused myopathies is indeed feasible.

Current therapies for DCM are mainly symptomatic and aimed at correcting secondary pathophysiological effects of reduced cardiac function such as neurohumoral activation and adverse remodeling of myocardial structure and electrical propagation. Here, we provided first experimental evidence that a new RNA-based strategy aiming at correcting the underlying pathophysiological mechanism of a familiar DCM may be effective. If successfully translated to patient care, such a strategy might effectively cure and, if applied early enough, prevent the DCM-induced heart failure. However, further preclinical studies in large animal models will be necessary to optimize chemistry, pharmacokinetics, and the administration regime of AONs *in vivo*, and for preclinical safety assessment.

4.1.2 Genetic modification reversed LQT1 phenotypes

4.1.2.1 Successful modeling of LQT1 with patient-derived and isogenic hiPSC-CMs

Genetic cardiac channelopathies, occurring in approximately one of 7,000 people, are heart diseases caused by mutations in genes encoding ion channel subunits or their regulatory proteins. At the cellular level, these diseases are often characterized by abnormal cardiac APs, and affected patients are typically predisposed to cardiac arrhythmias, with varying degrees of severity. Animal models often poorly represent human cardiac electrical characteristics. Thus, patient-specific hiPSC-CMs offer an interesting human model for studying cardiac

electrophysiology of genetic channelopathies. Since their introduction in 2007^{8, 235}, hiPSCs have been extensively used to model cardiac diseases, with a strong focus on channelopathies^{222, 236}, e.g. long-QT syndromes such as LQT1 and LQT2, catecholaminergic polymorphic ventricular tachycardia (CPVT), and Timothy syndrome.

In this study, electrophysiology of LQT1 was studied in patient-specific and corresponding isogenic genetically-corrected hiPSC-CMs using subtype-specific optical AP recordings. Specifically, we used patient hiPSCs carrying the LQT1-associated heterozygous R190Q mutation in the *KCNQ1* gene, which encodes a subunit of the delayed rectifier potassium channel conducting the I_{Ks} current. Previous patch clamp studies from our lab could demonstrate a dominant negative trafficking defect as pathomechanism of this mutation, resulting in a 70 to 80% reduction in I_{Ks} current in LQT1 CMs³³. Here, using FRET-based voltage membrane recording, we observed disease-specific abnormalities such as a prolonged duration of the action potential, increased prevalence of EADs, and vulnerability to cisapride-induced arrhythmias in the LQT1 CMs.

Moreover, using lineage-specific promoters, we could show that the disease phenotypes were only observed in the ventricular and atrial lineages, but not in nodal cardiomyocytes, in which *KCNQ1* is not expressed. These results underscore a precise genotype-phenotype correlation in patient-specific iPSC-CMs, providing the opportunity to test potential gene therapy targeting the mutated gene.

To date, insights into the pathogenesis of LQT1 have come predominantly from genetic animal models and heterologous expression systems. Depending on the cell type used, both dominant-negative effects and haploinsufficiency have been postulated as the disease mechanism associated with the *KCNQ1* (R190Q) mutation²³⁷. Due to differences among species in the ion currents that contribute to the cardiac repolarization phase, none of the available LQT1 mouse models fully emulate the human disease phenotype. Recently, transgenic rabbit models of LQT1 and LQT2 have been engineered by overexpression of dominant-negative channel mutants of human *KCNQ1* and *KCNH2*²³⁸. In these animals, however, both transgenes resulted in a down-regulation of the complementary I_{Kr} and I_{Ks} currents. By contrast, in the previous work from our lab³³, no alterations in repolarizing currents other than in I_{Ks} were observed in the LQT1 patient-specific iPSC-CMs. This discrepancy, which may be model-dependent or mutation-dependent, highlights the importance of alternative systems in which human genetic disorders can be investigated in their native physiologic and genetic background. Both our data and

previous results provide clear evidence that the pathogenesis of the R190Q mutation can be modeled in cardiac lineages derived from LQT1 patient-specific iPSCs, independent of the experimental methods used to assess the phenotype.

In spite of the successes in modeling genetic diseases with hiPSCs, one crucial limitation for disease modelling using hiPSCs is that humans are genetically heterogeneous^{239,240}, and, therefore, genetically-matched controls are necessary to discriminate disease-relevant phenotypes from effects of genetic background variability due to polymorphisms in other genes. Here, we used an isogenic control hiPSC line in which the LQT1-causing mutation had been corrected at the genomic level by homologous recombination (LQT1^{corr} iPSCs). We investigated the disease phenotype in parallel in both LQT1 patient-specific iPSCs and in the LQT1^{corr} isogenic control. The LQT1 disease phenotypes were absent in both ventricular and atrial LQT1^{corr} CMs and efficiently rescued by wild type *KCNQ1* overexpression, suggesting that the specific mutation is the major cause of the LQT1 phenotype. However, the fact that the AP duration in the unrelated control was even shorter than in the LQT1^{corr} CMs indicates that the LQT1 patient might carry, in addition to the *KCNQ1* mutation, additional genetic variants that are associated with prolonged cardiac APs. These putative additional genetic disease modifiers deserve further investigation.

In addition, it is widely recognized that hiPSC-derived CMs are immature, with gene expression patterns, electrical properties and contraction forces only equivalent to those of neonatal or fetal human cardiomyocytes^{241,242}. However, our results indicate that these cells are capable of capturing specific traits of LQT1, corroborating earlier findings^{34,148}. Since our study compared genetically-matched lines differing only in the *KCNQ1* (R190Q) point mutation, a clear genotype–phenotype association could be ascertained. This is of particular importance given the potential of over- or under-estimating the impact of a disease-causing mutation in the presence of bias due to choosing an unrelated control. Therefore, this isogenic approach is a powerful means to identify links between specific genotypes and disease predisposition, as also demonstrated for neurodegenerative disease²⁴³.

Furthermore, this approach can investigate whether the specific genetic lesion is pathogenic or whether there are modifier loci involved. Considering the increasing awareness of variations in individual genetic context²⁴⁴ and the biological differences between hiPSC lines²⁴⁵, the use of isogenic hiPSC pairs may overcome some of the shortcomings of conventional approaches in identifying disease-associated phenotypes. As more and more channelopathy-related hiPSC

lines are studied by using gene-editing approaches, the genetic causes and molecular mechanisms of other channelopathies may be elucidated.

4.1.2.2 *KCNQ1*^{R190Q} mutation correction and WT *KCNQ1* overexpression rescued LQT1 phenotypes

Gene correction of *KCNQ1* mutation in hiPSCs attenuated abnormalities in AP values in hiPSC-CMs, suggesting therapeutic function of gene editing-based approaches. Although precise gene editing of human CMs in situ is not an immediate option for treating LQTS or for regenerative medicine, gene targeting as it was carried out here offers essential tools for studying genetic–phenotypic interaction, deciphering molecular mechanisms, and perhaps, in the near future, assessing disease-related SNPs identified by GWAS in humans. Other rescue strategies, such as exon skipping and RNA interference, may only result in partial modification on the mRNA level⁴⁶, while genetic correction could restore the normal genotype in monogenic and even multigenic diseases. Recently, gene correction has been increasingly considered as a promising therapeutic strategy for genetic disease. Especially mutation correction in autologous hematopoietic stem cells seems to be a feasible goal, while its applications in germ cells is still subject to important ethical and legal restrictions. At the meantime, methods for gene correction-based therapy have advanced in versatility, including traditional homologous recombination, zinc finger nucleases, TALENs and Crispr/Cas9. The last two, especially Crispr/Cas9, have tremendously simplified the procedure of gene correction by increasing the efficiency of gene targeting³².

In addition, the disease phenotype could also be rescued in the patient cells by AAV6-mediated overexpression of wild-type *KCNQ1* subunits, indicating an alternative approach to gene therapy for diseases associated with low expression levels of functional proteins. In fact, some AAV serotypes, especially 6, 9 and 1, are accepted to have a strong heart tissue tropism and high transduction efficiency in cardiomyocytes as well as coronary smooth muscle cells. An AAV1 construct was also licensed as the first clinical gene therapy product, alipogene tiparvovec (marketed under the name Glybera), to treat lipoprotein lipase deficiency. Alipogene tiparvovec consists of an engineered copy of the human LPL gene packaged with a tissue-specific promoter in a non-replicating AAV1 vector particularly targeting muscle to restore the defects in LPL enzyme activity required to enable the processing or clearance of fat-carrying chylomicron particles formed in the intestine after a fat-containing meal. Moreover, the first clinical trial of gene therapy on patients with heart failure (CUPID) was launched in 2007 to 2008

^{246,247}. The CUPID trial was a multicenter trial designed to evaluate the efficacy of AAV1-mediated gene transfer of the SERCA2a cDNA delivered by a single intracoronary infusion. Twelve-month follow-up suggested improved symptoms, biomarkers as well as LV function, and reduced cardiovascular events in several patients (ClinicalTrials.gov NCT00454818).

4.1.3 hiPSC as a testing system for gene therapies in treating hereditary heart diseases

In our study, the AON-mediated skipping of the mutated *TTN* exon 326 reframed the titin mRNA, thus partially restoring titin function in the DCM CMs. The point mutation correction of *KCNQ1* (R190Q) by homologous recombination greatly attenuated the AP defects in LQT1 CMs. AAV6-mediated episomal expression of wt *KCNQ1* cDNA rescued the AP abnormalities in the same LQT1 CMs.

Taken together, these results can be considered as a proof of concept showing that the hiPSC system is not only suitable for studying pathomechanisms of genetic diseases, but also an excellent setting for testing possible gene therapies. Specifically, hiPSC could serve the evaluation of gene therapies in several aspects. First, hiPSCs allow investigating efficacy and possible off-target effects of mutation correction in the patient genome and also provide a theoretically unlimited cell source for potential therapeutic transplantations. Secondly, the advance in Crispr/Cas9 technology makes it possible to modulate the epigenetics as therapeutic strategy in hiPSCs and their derived cells. Thirdly, patient hiPSCs offer an ideal background to test the RNA based therapies acting at the post-transcriptional level, such as AON-mediated exon skipping and shRNA-mediated gene silencing. Moreover, the effects of episomal overexpression of non-mutated protein can also be evaluated in the target cells of the disease, which are derived from hiPSC. These cells can be also used to test the specificity of promoters and the efficiency of delivery tools. Finally, hiPSCs theoretically offer the possibility to investigate toxicity and off-target effects in any cell type of the human body.

4.2 Subtype-specific AP recordings facilitate cardiac disease modelling and pharmacological investigation in healthy and diseased hiPSC-CMs

4.2.1 Optical AP recordings as a promising tool for large-scale cardiac drug discover and toxicity screening in healthy and diseased hiPSC-CMs

Toxicity evaluations are one of the leading cost factors in drug development, and cardiotoxicity is of top concern in pharmaceutical toxicology. The establishments of hiPSC reprogramming and hiPSC-CM differentiation protocols provide an unlimited source of human cells as *in vitro* test systems for preclinical cardiac toxicity. Despite the embryonic characteristics of hiPSC-CM, the typical properties of human CMs are recapitulated by hiPSC-CM, including full expression profiles of membrane ion channels, the ability of generating APs and Ca²⁺ transients, sarcomere assembly and contractile development. In this study, we reprogrammed human somatic cells into hiPSCs by overexpression of classic Yamanaka transcriptional factors (c-MYC, SOX2, KLF4 and OCT4), and subsequently differentiated them into CMs using both spontaneous and chemically defined direct differentiation protocols. We showed that these hiPSC-CMs indeed present major characteristics of human heart cells such as characteristic AP phenotypes in the three myocytes lineages, striated sarcomeric structure, and rhythmical beating. We conducted optical action potential recordings in 3-month-old CMs derived from four unrelated healthy control hiPSC lines, which were generated by either retrovirus- or sendai virus-mediated reprogramming of dermal fibroblasts or keratinocytes (Fig 28). With respect to action potential characteristics, the results were similar among the four lines, indicating the consistency of hiPSC-CMs in recapitulating physiological characteristics independent from reprogramming methods or genetic background-related variations. Taken together, hiPSC-CMs provide reliable read-out assays for studying potential cardiotoxicity, such as sarcomere organization and contraction force, Ca²⁺ transients, EC coupling, AP durations and arrhythmias.

In addition, patient iPSCs represent an unprecedented source of diseased CMs, whose incorporation in the “modern” cardiotoxicity screenings is becoming more and more appealing, considering the recognized importance of genetic variations in determining the individual susceptibility to cardiotoxicity (not accounted for in “traditional” safety pharmacology).

In our DCM study, the DCM hiPSC-CMs displayed increased vulnerability to catecholamine-induced stress as compared to their healthy counterparts, indicated by a higher percentage of

CMs with disorganized sarcomeres and reduced expression levels of sarcomeric genes. In the work on LQT1 disease modelling, we showed that the KCNQ1 mutation predisposed LQT1 hiPSC-CMs to prolonged AP durations and occurrence of EADs when treated by QT-interval-prolonging drugs such as cisapride. These results emphasize that it might be important to include diseased hiPSC-CMs derived from toxicity-susceptible individuals into *in vitro* cardiotoxicity tests.

For patients suffering from LQT syndromes, CPVT or DCM, who are predisposed to arrhythmogenicity, even common drugs or nutrition supplements could be cardiotoxic. In these specific cases, personalized medication might greatly help to reduce the risk of cardiotoxicity and drug screening on patient iPSC-CMs would facilitate such individualized therapy.

As hiPSCs and their derived cells are increasingly used in pharmaceutical screening, tools for their molecular and physiological evaluation have been extensively developed, allowing investigation of cell responses to candidate pharmaceuticals at distinct structure and metabolism levels. Visualization of biological events by light has been intensively investigated due to its ability of probing nanoscale dynamics and being high throughput.

AP morphology and arrhythmias are direct and crucial readouts for cardiomyocyte function, which were not only successfully monitored by our optical AP recording methods but also measured in a high throughput manner relying on the adjustable field of vision of the recording microscope. By using 40-fold magnifications for optical AP measurement, APs of 100 cells can be easily recorded within two hours, which also can be improved by automatic imaging systems and packed analysis. Therefore, the throughput of the optical AP recording is far beyond that of classic patch clamp electrophysiology. Throughput is a major concern for a primary and secondary screening dealing with thousands of drug candidates in a library. A high throughput method for primary or secondary cardiac toxicity screen could be achieved by combining a panel of hiPSC-CMs and optical AP imaging.

MLC2v-VSFP based optical imaging detected disease-causing abnormalities in both LQT1-CMs (APD prolongation and EAD occurrence) and CPVT-CMs (DAD and TA activities, data not shown), whose genetic causes are associated with distinct cellular mechanisms: LQT phenotypes relate to defects in AP while CPVT disorders assign to misstep in Ca^{2+} handling. This highlights the feasibility of optical membrane potential imaging for detecting a broad spectrum of arrhythmogenic phenomena, all ultimately influencing the function of plasma membrane ion channels.

4.2.2 Subtype specific AP recordings enabled accurate phenotyping in LQT1 hiPSC-CM subtypes.

Promoter-driven VSFP expression empowers selective AP recording in particular cell types, depending on the chosen promoter elements. Based on results of a cardiac subtype specific transcript screening (Fig 22), we chose the *MLC2v* enhancer and *SLN* and *SHOX2* promoter fragments to direct VSFP expression to ventricular, atrial, and nodal cardiomyocytes, respectively. This subtype-specific strategy precisely probed the phenotypic properties of the LQT1 iPSC-CMs, namely prolonged AP durations and prominent EAD occurrences in the *MLC2v*- and *SLN*-positive cells (representing working myocytes), but not in *SHOX2* pacemaker cells that lack expression of the disease causing *KCNQ1* gene (Fig. 31). Similarly, the specific AP recording method has the advantage of enabling the investigation of drug effects selectively in distinct CM subtypes. We confirmed this application by investigating the effects of two drugs: cisapride, which targets the hERG channels, and ivabradine, a selective blocker of the pacemaker current I_f . We observed that the non-selective PGK-VSFP-guided membrane potential recording was sufficient to detect the AP-prolonging and EAD-promoting effect of cisapride. By contrast, the non-specific approach failed to reveal an effect of ivabradine on the beating rate. The lack of observable effect on the beating rate may be attributed to the low percentage of nodal-like cells (the only ones that respond to ivabradine) in the hiPSC-CM preparations. Consistently, using the subtype-specific AP imaging approach, we observed an ivabradine-mediated reduction of the beating rate only in nodal, but not in atrial or ventricular hiPSC-CMs (Fig 34). These discrepant outcomes in testing ivabradine's effects with different sensors highlight the superiority of using subtype specific AP recordings for the investigation of drugs or disease phenotypes that are confined to specific CM subtypes.

4.2.3 Subtype-specific AP recordings allowed sequential investigation of the same cells over extended time periods

Unlike electrical AP recordings using patch clamp or sharp microelectrodes, VSFP-based optical AP detection relies on light excitation and emission, enabling nondestructive electrical monitoring of excitable cells. This preserves the integrity of the CMs, allowing sequential probing of the cells over days to weeks.

We performed the LQT1 phenotype rescuing experiment in LQT1 CMs in which WT *KCNQ1* cDNA was overexpressed by AAV6-mediated gene transfer, and utilized the ventricular voltage sensor to monitor the rescuing dynamics. The same single LQT1 CMs were investigated before

and 3 days after KCNQ1 transgene expression, showing phenotypic rescue to APD values similar to those of LQT^{corr} CMs (Fig 32). This highlights the feasibility and reliability of sequential VSFP-based electrical signal monitoring.

The imaging approach established here could serve as a tool for investigating questions regarding cardiac lineage-specific differentiation of hiPSC and maturation of hiPSC-CM, allowing non-destructive imaging of AP dynamics in different hiPSC subtypes during the course of cardiac differentiation and in response to interventions (e.g. microRNA interference or drug treatment) aimed at augmenting cardiac lineage specification or maturation. Although MEA systems also allow long-term detection, they have the drawback of providing only extracellular recordings rather than transmembrane potentials. Moreover, using MEAs, subtype-specific AP recordings are not possible. A combination of MEA and optical recordings could be easily achieved by culturing CMs on MEA plates, possibly combining the advantages of both recording methods. Such a system would allow simultaneous monitoring of extracellular potentials and cell-clusters' syncytial characteristics (by MEA) as well as membrane potential properties with additional functional information, higher spatial resolution, and subtype-specificity.

4.2.4 Comparison of optical and electrode-based methods in action potential measurement

While measuring electrophysiology using the patch clamp is still the gold standard to investigate electrical characteristics ranging from single ion channel currents to APs, it suffers from the major limitation of the very low throughput. The amount of recording that can be obtained in a given time frame is further limited by the common practice of first assessing a larger number of cells and then limiting the analysis to those cells identified as the subtype of interest (e.g. ventricular-like cells) based on AP morphology^{33,248, 249}. Optical AP recordings using either small-molecule voltage-sensitive dyes or genetically-encoded membrane voltage sensors²⁵⁰ are an emerging tool to overcome the throughput limitation of patch clamp.

Optical electrical monitoring and patch clamp have overlapping applications in detecting AP durations, spontaneous and drug-induced arrhythmias, and characterizing cell type-specific APs. Both methods can be applied when these parameters are of the main interest. However, when throughput is highly considered, optical recording is superior to the patch clamp method. For example, in preclinical cardiac toxicity tests or candidate cardiac drug development, a library of over tens of thousands of drugs needs to go through 3 to 4 steps of experimental screening to reduce the candidates and select most promising ones for the further examination; in this case,

the optical AP recording will be more economic and time-saving in comparison to patch clamp. AP characteristics is one of the most important readouts used to indicate the potential of a drug. During the first step of massive screening, Ca^{2+} transients are often recorded to monitor the AP indirectly²⁵¹. However, since Ca^{2+} influx mainly contributes to two phases of the AP - the late depolarization and the early repolarization phases - this indirect method might not precisely indicate the whole picture of AP characteristics. Thus, newly-developed methods of optical AP recording would be a better choice in the first steps of preclinical drug screening assays. Once the drug number has been reduced and more accurate assessment of AP characteristics is needed, patch clamp takes over this mission in the third or fourth step of the screening process.

However, there are also applications that could be achieved exclusively by either of the tools. Patch clamp is well known for its ability to record currents from single ion channels and its accuracy in measuring absolute transmembrane voltages and detailed characteristics of all the 4 phase of a the AP, which currently cannot be achieved by optical voltage sensor, while optical recordings have the unique potential of allowing cell type-specific measurements and intracellular organelle targeting. Since, therefore, both means have their pros and cons, the preference in application depends on the experimental intention. Moreover, a better readout can be obtained by combining the two methods, namely patching the same cells after optical AP recording performed.

Of course, the evolution of both means is ongoing. Patch clamp is stepping toward discovering ion channels on intracellular organelles, e.g. lysosomes, mitochondria, or the inner cellular membrane system (ER/SR, Golgi and nuclear membrane). Besides the goal of boosting brightness, dynamic range and fast kinetics of fluorescent-based optical recording, the field is also attempting to indicate the absolute voltage parameters based on standardizing the overshoot of fluorescent intensity. Moreover, by tagging the fluorescence protein to ions channels of interest, visualization of specific channel currents might be achieved. Optical recording based on FP with far-red emission spectra would well facilitate the noninvasive AP recording in vivo and in 3D cell culture systems.

By using genetically-encoded voltage sensors, it was possible to image APs in rat primary CMs²⁵², whole mouse hearts¹⁵¹, and human embryonic stem cell-derived CMs¹⁵². Optical membrane potential imaging was also recently used successfully for hiPSC-CMs using the genetically-encoded voltage indicator ArcLight, which is a monochromatic sensor²⁵³. Both monochromatic and FRET based voltage indicator were well engineered. There are two main

advantages of monochromatic voltage indicators. First, being variable in fluorescent hues, it is easier to combine single FP based voltage sensors with other ion optical indicators (Ca^{2+} , K^+ and Na^+) and optical actuators (Channel rhodopsins) to realize two FPs-based dual imaging and combining optical actuation and sensing. Second, single FPs take up smaller encoding volumes in virial plasmids which might result in a high package efficiency of virus and reduce the potential mistargeting or intracellular aggregates of FPs. On the other hand, FRET-based voltage sensors not only were reported to have brighter FP intensity, faster dynamic switch and better photo- and pH-stability as compare to single FP indicators, but also were discovered to be more accurate in recoding the AP while the samples are moving (e. g. cardiomyocytes) by eliminating motion artifacts radiometrically.

4.2.5 Potential applications of subtype AP recording in vitro and in vivo

Fluorescence-based AP imaging can be combined with other types of genetically-encoded or chemical indicators (e.g. Ca^{2+} indicators) with non-overlapping fluorescence spectra to accomplish dual- or multi-color imaging of cellular activities. Multi-indicator imaging could be designed to function either at a shared intracellular locus or at separate cellular compartments (cytosol, nuclear, mitochondria, ER or SR) by linking the indicators with specific targeting signals. Multi-indicator or/and compartment-specific imaging then could be translated to any cell type of interest using specific promoter-driven strategies. To avoid repeating infections of the cells with sensor encoding virus, standardized sensor knock-in hiPSC lines might be generated which could also facilitate the imaging of the cells in culture and differentiated in 3D systems (e.g. engineered heart tissue, bioprinted tissue or organoids). Precise imaging of such three-dimensional tissue constructs could be performed by two-photon microscopy.

4.3 Future scenarios of personalized medicine

Reprogramming somatic cells from any individual into hiPSCs creates unprecedented opportunities to obtain differentiated somatic cell types. Protocols for differentiating hiPSCs are increasingly improved by mimicking the chemistry of human development, using a screening method varying the sequence, dosage, and timing of molecules acting in the crucial signaling pathways (e.g. Wnt, BMP, TGF β and Notch signaling) of embryonic development. Currently, hiPSC can be differentiated into cardiomyocytes, neurons, hepatocytes, pancreatic beta cells, adipocytes, endothelial cells and smooth muscle cells, among others, using corresponding protocols. The differentiated cells from a patient with a genetic disease can be used as models

to study her/his disease mechanisms and find the optimal treatment for her/him. Such models could also be used as a screening platform to eliminate potential side effects of possible medications. HiPSC-derived cells also lend themselves as an ideal autologous source for replacement of damaged cells. The possibility of cell replacement extends to patients with genetic mutations that can be corrected in hiPSCs by homologous recombination, TALEN or Crispr/Cas9, enabling the generation of healthy differentiated cells.

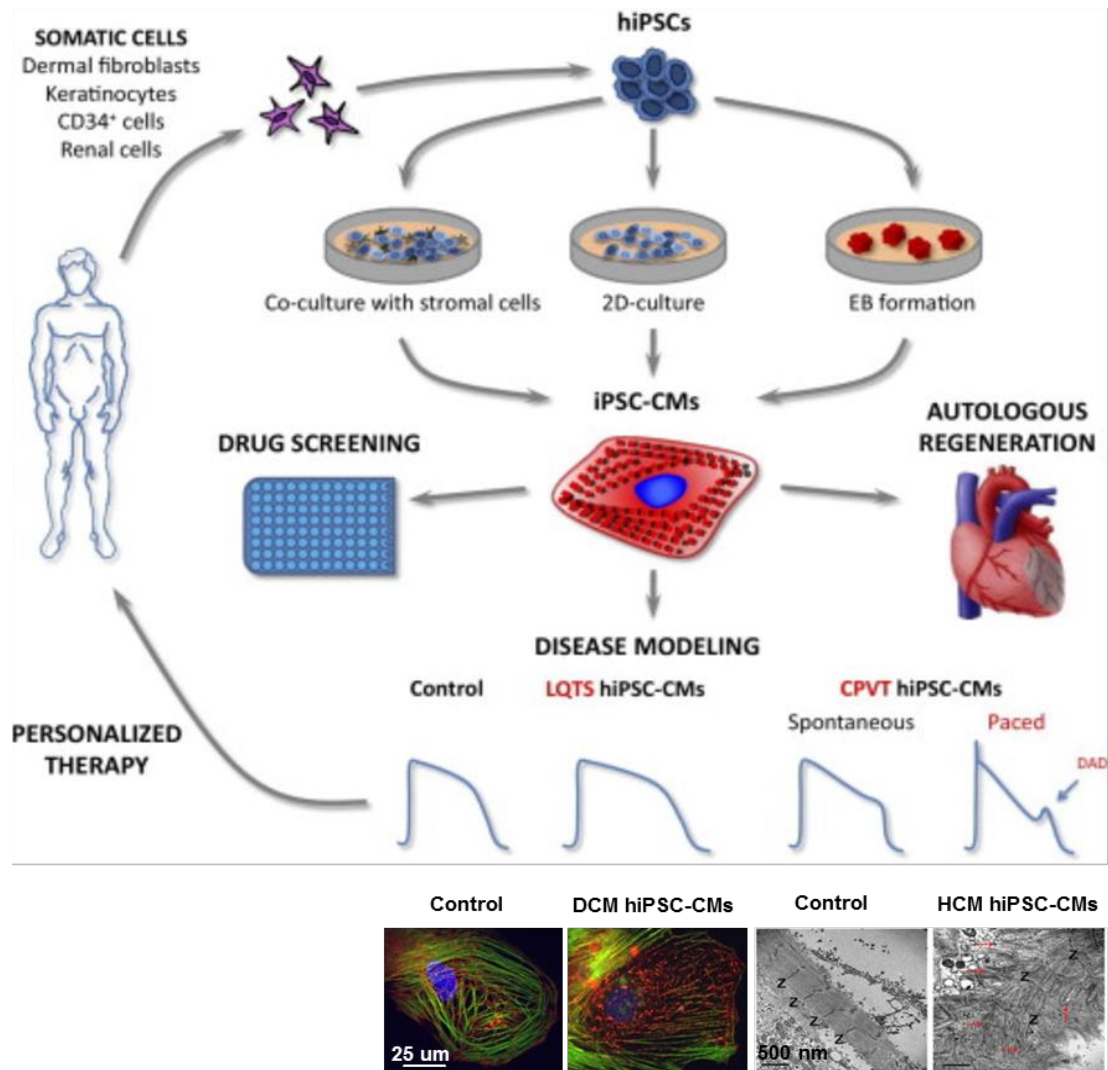


Figure 35: Possible applications of patient-specific iPSC-CMs. Several types of somatic cells can be reprogrammed iPSCs. Hipsocs can be used to generate patient-specific cardiomyocytes (iPSC-CMs) or other differentiated cell types using ad hoc differentiation protocols. HiPSC-CMs then can be used for drug discovery and cardiotoxicity, regenerative therapies, and disease modeling. Inherited different types of arrhythmogenic channelopathies (e.g. LQTs and CPVT) and cardiomyopathy (e.g. DCM and HCM) were well investigated by using patient specific iPSC-CMs. 2D: 2-dimensional; CPVT: catecholaminergic polymorphic ventricular tachycardia; DAD: delayed afterdepolarization ²⁵⁴.

Advanced heart failure is a progressive disease and a main cause of mortality and morbidity worldwide. Since its typical pathology is a definite decrease in the number of functional CMs, supplementation of functional CMs into the damaged heart would theoretically be an ideal therapeutic option (Fig 35). Several animal studies have shown that transplantation of hiPSC-CMs into diseased hearts leads to recovery of cardiac function, therefore establishing "proof-of-concept" of the hiPSC-transplantation therapy (Fig 35).

Conclusion

In the study of modeling titin-based DCM with patient-specific hiPSC-CMs carrying the TTN Ser14450fsX4 mutation, we observed defects in sarcomere assembly and maintenance of a stable sarcomere structure (Fig 13), which were associated with perturbations of the titin-TK-interacting Nbr1/p62/SQSTM1/MURF2 signalosome and decreases of SRF-dependent muscle gene expression caused by the nuclear translocation of MURF, inhibiting its activity on transcriptional factor SRF (Fig 14). In an attempt to rescue the DCM disease phenotype, we employed the exon skipping strategy mediated by AON-based targeting of the mutated exon. We first used both HL-1 cells and hiPSC-CMs to evaluate the optimal sequence, chemistry, and combination of AONs to prevent the integration of TTN exon 326 into the mRNA transcript. We found a combination of AONs (AON1 and 3) that resulted in an efficient excision of the mutated exon, which only had a negligible effect on both HL-1 cells and human healthy iPSC-derived cardiomyocytes. Excision of the mutated exon in patient-specific CMs not only improved myofibril assembly and stability but also normalized the sarcomeric gene expression regulated by the titin TK. Consistently, in Ttn mutation knock in mouse models, the AON-based antisense strategy rescued the cardiac defects in both homozygous embryos and heterozygous adult mice. Our proof of concept study suggests that exon skipping is a potential therapeutic approach for familial DCM. In spite of the success of this preclinical evaluation and the urgent need of a therapy for familial DCM causing severe heart failure in middle-aged patients, further studies of systematic toxicology and long-term therapeutic efficacy of this antisense therapy are still required. In addition, our work demonstrates that patient-specific iPSCs can provide a new human cellular platform for investigating therapies for genetically-mediated disease, although maturation and heterogeneity of hiPSC-derived cells continues to be a considerable issue for the field.

To allow subtype-specific electrophysiological phenotyping in the heterogeneous population of hiPSC-CMs using optical measurements, we constructed four lentivirus vectors encoding a FRET-based voltage sensor to be expressed ubiquitously (PGK-VSFP) or specifically in the three major subtypes of cardiomyocytes (MLC2v-, SLN and SHOX2-VSFP for expression in ventricular-, atrial- and nodal-like cardiomyocytes, respectively). By applying this method to hiPSC-CMs derived from a patient with congenital long-QT syndrome type 1, we demonstrated its ability to investigate key features of the disease such as AP prolongation and occurrence of EADs. Moreover, employing an isogenic control line generated by correcting the disease-causing mutation at the genomic level, we showed that the method is sensitive enough to detect

the functional consequences of a single *KCNQ1*-R190Q mutation. The disease phenotype could also be rescued in the patient cells by overexpressing wild-type *KCNQ1* subunits. This experiment highlighted the feasibility of repeated AP measurements in the same cells – in this case with an interval of 72 h between measurements. Finally, we demonstrated that our method allows assessment of the effects of QT interval-prolonging drugs such as cisapride on AP duration and the occurrence of EADs. In addition, we demonstrated that LQT1 hiPSC-CMs showed particular vulnerability to cisapride-induced arrhythmias, emphasizing the consideration of potential side effects or toxicity in subjects with pre-existing cardiac diseases. Furthermore, the CM subtype-specificity of the method supports investigation of the response to pharmacological agents that have selective effects on atrial-, ventricular- and pacemaker-like cells. This was notably illustrated by the nodal-selective I_f current blocker Ivabradine. The optical method not only increased the throughput far beyond that of single-cell patch clamp electrophysiology, it also allowed sequential investigation of the same cells over extended time periods during genetic manipulation of AP dynamics. The subtype specificity substantially reduced the variability of AP properties caused by the heterogeneity in hiPSC-CMs differentiation and allowed investigation of phenotypes in a CM subtype-specific way. These tools are suitable to be incorporated into not only academic research using hiPSC-CMs but also to be further developed into a high-throughput screening platform for cardiac drug discovery and toxicological screening.

In summary, our proof-of-concept experiments suggest that patient-specific hiPSC-CMs can precisely model cardiac diseases, allow to test the efficacy of drugs for particular diseases and evaluate cardiotoxicology.

Supplemental Tables

Supplemental Table 1: AON sequences.

Name	Sequence
2OMePS- hAON1	UUG AUG CUC CAC GAC AUA G
2OMePS- hAON3	CCA UGC CAA AGA AGC AGA UU

Supplemental Table 2: List of primers for nested PCR.

Name	Species	Sequence
ex324f	Mouse	ATACCTCTTCCGTGTGTCAGCAG
ex325f	Mouse	ACCAGTTTCCGATCTCAGGTGC
ex326r	Mouse	TTCAACATTTGGAATCACAGC
ex327r	Mouse	TTGATGAGGACAGGAAGCAG
ex328r	Mouse	ACTTTAATCATGGTTCTTGCTACTG
hex324f	Human	GTACATCTTCCGGGTCTCAGCTG
hex325f	Human	ACCAGTTTCCGATCTCAGGTGC
hex326r	Human	TTCAACATCTGGAATCACCGC
hex327r	Human	TTAATAAGAACAGGAAGCAG
hex328r	Human	ACTTTCATCATGGTTCTTGCAACTG

Supplemental Table 3: Primers for RT-PCR, mutagenesis PCR, and sequencing.

Name	Use	Sequence	
hTTNe326AT	Sequencing	For	CCTCTGAAGCACCATCTCCAC
		Rev	CCTCCAAGTGATGGCAGTG
Sendai Virus	qRT-PCR	For	GGATCACTAGGTGATATCGAGC
		Rev	ACCAGACAAGAGTTTAAGAGATATGTA TC
hGAPDH	qRT-PCR	For	TCCTCTGACTTCAACAGCGA
		Rev	GGGTCTTACTCCTTGAGGC
hc-MYC endo	qRT-PCR	For	AGAAATGTCCTGAGCAATCACC
		Rev	AAGGTTGTGAGGTTGCATTTGA
hKLF4 endo	qRT-PCR	For	ATAGCCTAAATGATGGTGCTTGG
		Rev	AACTTTGGCTTCCTTGTTTGG
hOCT3/4 endo	qRT-PCR	For	GACAGGGGGAGGGGAGGAGCTAGG
		Rev	CTTCCCTCCAACCAGTTGCCCAAAC
hSOX2 endo	qRT-PCR	For	GGGAAATGGGAGGGGTGCAAAAGAGG
		Rev	TTGCGTGAGTGTGGATGGGATTGGTG

Supplemental Tables

hNANOG	qRT-PCR	For	TGCAAGAACTCTCCAACATCCT
		Rev	ATTGCTATTCTTCGGCCAGTT
hREX1	qRT-PCR	For	ACCAGCACACTAGGCAAACC
		Rev	TTCTGTTACACAGGCTCCA
hTDGF1	qRT-PCR	For	CCCAAGAAGTGTTCCCTGTG
		Rev	ACGTGCAGACGGTGGTAGTT
hPDX1	qRT-PCR	For	AAGCTCACGCGTGGAAG
		Rev	GGCCGTGAGATGTA CT TGTG
hSOX7	qRT-PCR	For	TGAACGCCTTCATGGTTTG
		Rev	AGCGCCTTCCACGACTTT
hAFP	qRT-PCR	For	GTGCCAAGCTCAGGGTGTAG
		Rev	CAGCCTCAAGTTGTTCTCTG
hCD31	qRT-PCR	For	ATGCCGTGGAAGCAGATAC
		Rev	CTGTTCTTCTCGGAACATGGA
hDES	qRT-PCR	For	GTGAAGATGGCCCTGGATGT
		Rev	TGGTTTCTCGGAAGTTGAGG
hACTA2	qRT-PCR	For	GTGATCACCATCGGAAATGAA
		Rev	TCATGATGCTGTTGTAGGTGGT
hSCL	qRT-PCR	For	CCAACAATCGAGTGAAGAGGA
		Rev	CCGGCTGTTGGTGAAGATAC
hMYL2	qRT-PCR	For	TACGTTCCGGAAATGCTGAC
		Rev	TTCTCCGTGGGTGATGATG
hCDH5	qRT-PCR	For	GAGCATCCAGGCAGTGGTAG
		Rev	CAGGAAGATGAGCAGGGTGA
hKRT14	qRT-PCR	For	CACCTCTCCTCCTCCAGTT
		Rev	ATGACCTTGGTGCGGATTT
hNCAM1	qRT-PCR	For	CAGATGGGAGAGGATGGAAA
		Rev	CAGACGGGAGCCTGATCTCT
hTH	qRT-PCR	For	TGTA CTGGTTCACGGTGGAGT
		Rev	TCTCAGGCTCCTCAGACAGG
hGABRR2	qRT-PCR	For	CTGTGCCTGCCAGAGTTTCA
		Rev	ACGGCCTTGACGTAGGAGA
hMYH6	qRT-PCR	For	TCAGCTGGAGGCCAAAGTAAAGGA
		Rev	TTCTTGAGCTCTGAGCACTCGTCT
hMYH7	qRT-PCR	For	TCGTGCCTGATGACAAACAGGAGT
		Rev	ATACTCGGTCTCGGCAGTGACTTT

Supplemental Tables

hACTC1	qRT-PCR	For	CCAAGATGTGTGACGACGAG
		Rev	ACGATGGACGGGAAGACA
U7- <i>TTN326</i>	Mutagenesis PCR	For	ACATAGCCATGCCAAAGAAGCAGATTAATTTTTGG AGCAGGTTTTCT
		Rev	TTGGCATGGCTATGTCGTGGAGCATCAATTGCGGA AGTGCGTCTGTA
U7- <i>TTNScr326</i>	Mutagenesis PCR	For	TTCTTAGATAACAATCAACCGGCATGAAATTTTTGGA GCAGGTTTTCT
		Rev	GATTGTATCTAAGAAGTTCGTGCTGCTACGCTTGCG GAAGTGCGTCTGTA
U7-m <i>Ttn326</i>	Mutagenesis PCR	For	CTCCTACTGCATTTGAAGGTGGTCCTAATTTTTGGA GCAGGTTTTCT
		Rev	CAAATGCAGTAGGAGATGATGCCTGGATTGCGGA AGTGCGTCTGTA
U7-m <i>TtnScr326</i>	Mutagenesis PCR	For	ACTACCAATGTGGCTCGTCGTAATTGAATTTTTGGA GCAGGTTTTCT
		Rev	AGCCACATTGGTAGTCGAGATATGGAGCTTGC AGTGCGTCTGTA
U7-Titin326ext	Mutagenesis PCR	For	GGGATCGATTAACAACATAGGAGCTGTG
		Rev	AAAGATATCCACATACGCGTTTCTAGGA
<i>SLN</i> promoter	PCR from genomic DNA	For	CACTGAGGCCAGAAAGGATAGATG
		Rev	TGGACTCCTGGACTCTGGGCAG
<i>SHOX2</i> promoter	PCR from genomic DNA	For	GTGTGTCTGTATAGAGTCGTGTGTG
		Rev	CTGCCGAGGGAAATGGGAACTG
<i>MLC2v</i> enhancer	PCR from genomic DNA	For	GCCACAGTGCCAGCCTTCATGG
		Rev	GTGGAAAGGACCCAGCACTGCC
<i>HA-KCNQ1</i>	PCR for tagging of HA fragment	For	GCATACCGGTATGTACCCATACGATGTTCCAGATT ACGCTGCCGCGGCCTCCTCCCCGCC
		Rev	TCAGGACCCCTCATCGGGGCCCTC
<i>SLN</i>	qRT-PCR	For	AGAGTCCAGGAGTCCAGACA
		Rev	CTTGGTGAGAACTGCAGGCA
<i>SHOX2</i>	qRT-PCR	For	CCTACATGATGTTCCAGCA
		Rev	GGAGTTCTTGCTGGTGGTCT
<i>MYL2 (MLC2v)</i>	qRT-PCR	For	TACGTTCCGGAAATGCTGAC
		Rev	TTCTCCGTGGGTGATGATG
<i>MYL7 (MLC2a)</i>	qRT-PCR	For	CCGTCTTCCTCAGCTCTT

Supplemental Tables

		Rev	TGAACTCATCCTTGTTACCAC
<i>HCN4</i>	qRT-PCR	For	CAATGAGGTGCTGGAGGAGT
		Rev	GGTCGTGCTGGACTTTGTG
<i>GAPDH</i>	qRT-PCR	For	TCCTCTGACTTCAACAGCGA
		Rev	GGGTCTTACTCCTTGGAGGC
VSFP transgene	qRT-PCR	For	GAAGTTCGAGGGCGACACCC
		Rev	CCTCCCTCGATGACTTTGATCC

References

1. Health, N. I. of. Stem Cell Basics. *Stem Cells*. 19, 1–26 (2009).
2. Pittenger, M. F. *et al.* Multilineage potential of adult human mesenchymal stem cells. *Science*. 284, 143–147 (1999).
3. Winkler, I. G. *et al.* Bone marrow macrophages maintain hematopoietic stem cell (HSC) niches and their depletion mobilizes HSCs. *Blood*. 116, 4815–4828 (2010).
4. Gage, F. H. Mammalian Neural Stem Cells. *Science*. 80. 287, 1433–1438 (2000).
5. Rahmani, W. *et al.* Hair Follicle Dermal Stem Cells Regenerate the Dermal Sheath, Repopulate the Dermal Papilla, and Modulate Hair Type. *Dev. Cell*. 31, 543–558 (2014).
6. Fukada, S., Ma, Y. & Uezumi, A. Adult stem cell and mesenchymal progenitor theories of aging. *Front. Cell Dev. Biol.* 2, 1–9 (2014).
7. Thomson, J. A. Embryonic Stem Cell Lines Derived from Human Blastocysts. *Science*. 80. 282, 1145–1147 (1998).
8. Takahashi, K. *et al.* Induction of pluripotent stem cells from adult human fibroblasts by defined factors. *Cell*. 131, 861–872 (2007).
9. Zhou, T. *et al.* Generation of induced pluripotent stem cells from urine. *J Am Soc Nephrol*. 22, 1221–1228 (2011).
10. Loh, Y.-H. *et al.* Generation of induced pluripotent stem cells from human blood. *Blood*. 113, 5476–5479 (2009).
11. Lowry, W. E. & Plath, K. The many ways to make an iPS cell. *Nat. Biotechnol.* 26, 1246–1248 (2008).
12. Warren, L. *et al.* Highly efficient reprogramming to pluripotency and directed differentiation of human cells with synthetic modified mRNA. *Cell Stem Cell*. 7, 618–630 (2010).
13. Soares, F. A. C., Sheldon, M., Rao, M., Mummery, C. & Vallier, L. International coordination of large-scale human induced pluripotent stem cell initiatives: Wellcome trust and ISSCR workshops white paper. in *Stem Cell Reports*. 3, 931–939 (2014).
14. Roth, G. A. *et al.* Demographic and epidemiologic drivers of global cardiovascular mortality. *N. Engl. J. Med.* 372, 1333–41 (2015).
15. Grskovic, M., Javaherian, A., Strulovici, B. & Daley, G. Q. Induced pluripotent stem cells--opportunities for disease modelling and drug discovery. *Nat. Rev. Drug Discov.* 10, 915–29 (2011).
16. Fermini, B. *et al.* A New Perspective in the Field of Cardiac Safety Testing through the Comprehensive In Vitro Proarrhythmia Assay Paradigm. *J. Biomol. Screen.* pii: 1087057115594589 (2015).
17. Itskovitz-Eldor, J. *et al.* Differentiation of human embryonic stem cells into embryoid bodies compromising the three embryonic germ layers. *Mol. Med.* 6, 88–95 (2000).
18. Lian, X. *et al.* Directed cardiomyocyte differentiation from human pluripotent stem cells by modulating Wnt/ β -catenin signaling under fully defined conditions. *Nat. Protoc.* 8, 162–75 (2013).
19. Veerman, C. C. *et al.* Immaturity of human stem-cell-derived cardiomyocytes in culture: fatal flaw or soluble problem? *Stem Cells Dev.* 24, 1035–52 (2015).
20. Braam, S. R., Passier, R. & Mummery, C. L. Cardiomyocytes from human pluripotent stem cells in regenerative medicine and drug discovery. *Trends in Pharmacological Science*. 30, 536–545 (2009).
21. Bruneau, B. G. The developmental genetics of congenital heart disease. *Nature*. 451, 943–948 (2008).
22. Mateizel, I. *et al.* Derivation of human embryonic stem cell lines from embryos obtained after IVF and after PGD for monogenic disorders. *Hum. Reprod.* 21, 503–511 (2006).
23. Urbach, A., Schuldiner, M. & Benvenisty, N. Modeling for Lesch-Nyhan disease by gene targeting in human embryonic stem cells. *Stem Cells*. 22, 635–41 (2004).
24. Elliott, D. A. *et al.* NKX2-5(eGFP/w) hESCs for isolation of human cardiac progenitors and cardiomyocytes. *Nat. Methods*. 8, 1037–40 (2011).
25. Bellin, M. *et al.* Isogenic human pluripotent stem cell pairs reveal the role of a KCNH2 mutation in long-QT syndrome. *EMBO J.* 32, 3161–3175 (2013).
26. Reyon, D. *et al.* FLASH assembly of TALENs for high-throughput genome editing. *Nat. Biotechnol.* 30, 460–465 (2012).

References

27. Cermak, T., Doyle, E. & Christian, M. Efficient design and assembly of custom TALEN and other TAL effector-based constructs for DNA targeting. *Nucleic acids*. 39, e82 (2011).
28. Mussolino, C. *et al.* A novel TALE nuclease scaffold enables high genome editing activity in combination with low toxicity. *Nucleic Acids Res.* 39, 9283–9293 (2011).
29. Hsu, P. D., Lander, E. S. & Zhang, F. Development and applications of CRISPR-Cas9 for genome engineering. *Cell*. 157, 1262–1278 (2014).
30. Mali, P. *et al.* RNA-guided human genome engineering via Cas9. *Science*. 80. 339, 823–826 (2013).
31. Li, H. L. *et al.* Precise correction of the dystrophin gene in duchenne muscular dystrophy patient induced pluripotent stem cells by TALEN and CRISPR-Cas9. *Stem Cell Reports*. 4, 143–154 (2015).
32. Charpentier, E. & Doudna, J. a. Rewriting a genome. *Nature*. 495, 50–51 (2013).
33. Moretti, A. *et al.* Patient-specific induced pluripotent stem-cell models for long-QT syndrome. *N. Engl. J. Med.* 363, 1397–409 (2010).
34. Itzhaki, I. *et al.* Modelling the long QT syndrome with induced pluripotent stem cells. *Nature*. 471, 225–229 (2011).
35. Ma, D. *et al.* Modeling type 3 long QT syndrome with cardiomyocytes derived from patient-specific induced pluripotent stem cells. *Int. J. Cardiol.* 168, 5277–5286 (2013).
36. Horie, M. Using induced pluripotent stem cells to investigate cardiac phenotypes in Timothy syndrome. *Respir. Circ.* 60, 483–488 (2012).
37. Davis, R. P. *et al.* Cardiomyocytes derived from pluripotent stem cells recapitulate electrophysiological characteristics of an overlap syndrome of cardiac sodium channel disease. *Circulation*. 125, 3079–3091 (2012).
38. Jung, C. B. *et al.* Dantrolene rescues arrhythmogenic RYR2 defect in a patient-specific stem cell model of catecholaminergic polymorphic ventricular tachycardia. *EMBO Mol. Med.* 4, 180–191 (2012).
39. Lin, B. *et al.* Modeling and study of the mechanism of dilated cardiomyopathy using induced pluripotent stem cells derived from individuals with Duchenne muscular dystrophy. *Dis. Model. Mech.* 8, 457–66 (2015).
40. Wu, H. *et al.* Epigenetic Regulation of Phosphodiesterases 2A and 3A Underlies Compromised ??-Adrenergic Signaling in an iPSC Model of Dilated Cardiomyopathy. *Cell Stem Cell*. 17, 89–100 (2015).
41. Dudek, J. *et al.* Cardiolipin deficiency affects respiratory chain function and organization in an induced pluripotent stem cell model of Barth syndrome. *Stem Cell Res.* 11, 806–819 (2013).
42. Sun, N. *et al.* Patient-specific induced pluripotent stem cells as a model for familial dilated cardiomyopathy. *Sci. Transl. Med.* 4, 130ra47 (2012).
43. Carvajal-Vergara, X. *et al.* Patient-specific induced pluripotent stem-cell-derived models of LEOPARD syndrome. *Nature*. 465, 808–812 (2010).
44. Ma, D. *et al.* Generation of patient-specific induced pluripotent stem cell-derived cardiomyocytes as a cellular model of arrhythmogenic right ventricular cardiomyopathy. *Eur. Heart J.* 1–12 (2012).
45. Kim, C. *et al.* Studying arrhythmogenic right ventricular dysplasia with patient-specific iPSCs. *Nature*. 494, 105–10 (2013).
46. Matsa, E. *et al.* Allele-specific RNA interference rescues the long-QT syndrome phenotype in human-induced pluripotency stem cell cardiomyocytes. *Eur. Heart J.* 35, 1078–1087 (2014).
47. Tedesco, F. S., Dellavalle, A., Diaz-Manera, J., Messina, G. & Cossu, G. Repairing skeletal muscle: Regenerative potential of skeletal muscle stem cells. *Journal of Clinical Investigation*. 120, 11–19 (2010).
48. Cecchi, F., Tomberli, B. & Olivotto, I. Clinical and molecular classification of cardiomyopathies. *Glob. Cardiol. Sci. Pract.* 2012, 4 (2012).
49. Yacoub, M. H. Decade in review—cardiomyopathies: Cardiomyopathy on the move. *Nat. Rev. Cardiol.* 11, 628–629 (2014).
50. Jefferies, J. L. & Towbin, J. A. Dilated cardiomyopathy. *Lancet* . 375, 752–62 (2010).
51. Somsen, G. A., Hovingh, G. K., Tulevski, I. I., Seidman, J. & Seidman, C. E. in *Clinical Cardiogenetics* 63–77 (2011).
52. Lyon, A. R., Samara, M. A. & Feldman, D. S. Cardiac contractility modulation therapy in advanced systolic heart failure.[Erratum appears in Nat Rev Cardiol. *Nat. Rev. Cardiol.* 10, 584–598 (2013).

References

53. Golbus, J. R. *et al.* Population-based variation in cardiomyopathy genes. *Circ. Cardiovasc. Genet.* 5, 391–399 (2012).
54. Pan, S., Caleshu, C. A., Dunn, K. E. & Ashley, E. A. Cardiac structural and sarcomere genes associated with cardiomyopathy exhibit marked intolerance of genetic variation. *Circ. Cardiovasc. Genet.* 5, 602–610 (2012).
55. Herman, D. S. *et al.* Truncations of Titin Causing Dilated Cardiomyopathy. *New England Journal of Medicine.* 366, 619–628 (2012).
56. Itoh-Satoh, M. *et al.* Titin mutations as the molecular basis for dilated cardiomyopathy. *Biochem. Biophys. Res. Commun.* 291, 385–393 (2002).
57. Bang, M. L. *et al.* The complete gene sequence of titin, expression of an unusual approximately 700-kDa titin isoform, and its interaction with obscurin identify a novel Z-line to I-band linking system. *Circ. Res.* 89, 1065–72 (2001).
58. Vikhlyantsev, I. M. & Podlubnaya, Z. a. New titin (connectin) isoforms and their functional role in striated muscles of mammals: facts and suppositions. *Biochem. Biokhimiia.* 77, 1515–35 (2012).
59. Obermann, W. M. J., Gautel, M., Weber, K. & Fürst, D. O. Molecular structure of the sarcomeric M band: Mapping of titin and myosin binding domains in myomesin and the identification of a potential regulatory phosphorylation site in myomesin. *EMBO J.* 16, 211–220 (1997).
60. Labeit, S. & Kolmerer, B. Titins: giant proteins in charge of muscle ultrastructure and elasticity. *Science.* 270, 293–296 (1995).
61. Lange, S. *et al.* The kinase domain of titin controls muscle gene expression and protein turnover. *Science.* 308, 1599–1603 (2005).
62. Trinick, J. Titin as a scaffold and spring. *Curr. Biol.* 6, 258–260 (1996).
63. Houmeida, A., Holt, J., Tskhovrebova, L. & Trinick, J. Studies of the interaction between titin and myosin. *J. Cell Biol.* 131, 1471–1481 (1995).
64. Labeit, S., Gautel, M., Lakey, A. & Trinick, J. Towards a molecular understanding of titin. *EMBO J.* 11, 1711–6 (1992).
65. Freiburg, a & Gautel, M. A molecular map of the interactions between titin and myosin-binding protein C. Implications for sarcomeric assembly in familial hypertrophic cardiomyopathy. *Eur. J. Biochem.* 235, 317–323 (1996).
66. Gutierrez-Cruz, G., Van Heerden, A. H. & Wang, K. Modular Motif, Structural Folds and Affinity Profiles of the PEVK Segment of Human Fetal Skeletal Muscle Titin. *J. Biol. Chem.* 276, 7442–7449 (2001).
67. Trinick, J. & Tskhovrebova, L. Titin: A molecular control freak. *Trends in Cell Biology.* 9, 377–380 (1999).
68. Miller, G., Musa, H., Gautel, M. & Peckham, M. A targeted deletion of the C-terminal end of titin, including the titin kinase domain, impairs myofibrillogenesis. *J Cell Sci.* 116, 4811–4819 (2003).
69. Gregorio, C. C., Perry, C. N. & Mcelhinny, A. S. Functional properties of the titin/connectin-associated proteins, the muscle-specific RING finger proteins (MURFs), in striated muscle. in *Journal of Muscle Research and Cell Motility.* 26, 389–400 (2005).
70. Centner, T. *et al.* Identification of muscle specific ring finger proteins as potential regulators of the titin kinase domain. *J. Mol. Biol.* 306, 717–726 (2001).
71. Mrosek, M. *et al.* Molecular determinants for the recruitment of the ubiquitin-ligase MuRF-1 onto M-line titin. *FASEB J.* 21, 1383–1392 (2007).
72. Amodeo, P., Fraternali, F., Lesk, A. M. & Pastore, A. Modularity and homology: modelling of the titin type I modules and their interfaces. *J. Mol. Biol.* 311, 283–296 (2001).
73. Peled, Y. *et al.* Titin mutation in familial restrictive cardiomyopathy. *Int. J. Cardiol.* 171, 24–30 (2014).
74. Pénisson-Besnier, I. *et al.* Myopathies caused by homozygous titin mutations: limb-girdle muscular dystrophy 2J and variations of phenotype. *J. Neurol. Neurosurg. Psychiatry.* 81, 1200–2 (2010).
75. Hackman, P. *et al.* Tibial muscular dystrophy is a titinopathy caused by mutations in TTN, the gene encoding the giant skeletal-muscle protein titin. *Am. J. Hum. Genet.* 71, 492–500 (2002).
76. Ceyhan-Birsoy, O. *et al.* Recessive truncating titin gene, TTN, mutations presenting as centronuclear myopathy. *Neurology.* 81, 1205–1214 (2013).
77. Ohlsson, M. *et al.* Hereditary myopathy with early respiratory failure associated with a mutation in A-band titin. *Brain.* 135, 1682–1694 (2012).
78. Gerull, B. *et al.* Mutations of TTN, encoding the giant muscle filament titin, cause familial dilated

- cardiomyopathy. *Nat. Genet.* 30, 201–4 (2002).
79. Gerull, B. *et al.* Identification of a novel frameshift mutation in the giant muscle filament titin in a large Australian family with dilated cardiomyopathy. *J. Mol. Med.* 84, 478–483 (2006).
 80. Herman, J. CPTSD is a distinct entity: Comment on Resick *et al.* (2012). *Journal of Traumatic Stress.* 25, 256–257 (2012).
 81. Yoskovitz, G. *et al.* A novel titin mutation in adult-onset familial dilated cardiomyopathy. *Am. J. Cardiol.* 109, 1644–1650 (2012).
 82. Hidalgo, C. & Granzier, H. Tuning the molecular giant titin through phosphorylation: Role in health and disease. *Trends in Cardiovascular Medicine.* 23, 165–171 (2013).
 83. Chauveau, C., Rowell, J. & Ferreiro, A. A rising titan: TTN review and mutation update. *Hum. Mutat.* 35, 1046–1059 (2014).
 84. Lee, J. & Yokota, T. Antisense Therapy in Neurology. *J. Pers. Med.* 3, 144–176 (2013).
 85. Yokota, T., Pistilli, E., Duddy, W. & Nagaraju, K. Potential of oligonucleotide-mediated exon-skipping therapy for Duchenne muscular dystrophy. *Expert Opin. Biol. Ther.* 7, 831–842 (2007).
 86. Yokota, T., Duddy, W., Echigoya, Y. & Kolski, H. Exon skipping for nonsense mutations in Duchenne muscular dystrophy: too many mutations, too few patients? *Expert Opin. Biol. Ther.* 12, 1141–1152 (2012).
 87. Malerba, A. *et al.* Chronic systemic therapy with low-dose morpholino oligomers ameliorates the pathology and normalizes locomotor behavior in mdx mice. *Mol. Ther.* 19, 345–354 (2011).
 88. Taniguchi-Ikeda, M. *et al.* Pathogenic exon-trapping by SVA retrotransposon and rescue in Fukuyama muscular dystrophy. *Nature.* 478, 127–131 (2011).
 89. Lee, J. E., Bennett, C. F. & Cooper, T. a. RNase H-mediated degradation of toxic RNA in myotonic dystrophy type 1. *Proc. Natl. Acad. Sci.* 109, 4221–4226 (2012).
 90. Hua, Y., Vickers, T. A., Baker, B. F., Bennett, C. F. & Krainer, A. R. Enhancement of SMN2 exon 7 inclusion by antisense oligonucleotides targeting the exon. *PLoS Biol.* 5, 729–744 (2007).
 91. Porensky, P. N. *et al.* A single administration of morpholino antisense oligomer rescues spinal muscular atrophy in mouse. *Hum. Mol. Genet.* 21, 1625–1638 (2012).
 92. Hoffman, E. P., Brown, R. H. & Kunkel, L. M. Dystrophin: The protein product of the duchenne muscular dystrophy locus. *Cell.* 51, 919–928 (1987).
 93. Lu, Q.-L. *et al.* The status of exon skipping as a therapeutic approach to duchenne muscular dystrophy. *Mol. Ther.* 19, 9–15 (2011).
 94. Aartsma-Rus, A. Antisense-mediated modulation of splicing: therapeutic implications for Duchenne muscular dystrophy. *RNA Biol.* 7, 453–461 (2010).
 95. Yokota, T., Duddy, W. & Partridge, T. Optimizing exon skipping therapies for DMD. in *Acta Myologica.* 26, 179–184 (2007).
 96. Yokota, T. *et al.* Expansion of revertant fibers in dystrophic mdx muscles reflects activity of muscle precursor cells and serves as an index of muscle regeneration. *J. Cell Sci.* 119, 2679–2687 (2006).
 97. Echigoya, Y. *et al.* Mutation Types and Aging Differently Affect Revertant Fiber Expansion in Dystrophic Mdx and Mdx52 Mice. *PLoS One.* 8, (2013).
 98. Saito, T. *et al.* Antisense PMO found in Dystrophic Dog model was effective in cells from exon 7-deleted DMD patient. *PLoS One.* 5, (2010).
 99. Aartsma-Rus, A. *et al.* Functional analysis of 114 exon-internal AONs for targeted DMD exon skipping: indication for steric hindrance of SR protein binding sites. *Oligonucleotides.* 15, 284–297 (2005).
 100. Aartsma-Rus, A. *et al.* Therapeutic antisense-induced exon skipping in cultured muscle cells from six different DMD patients. *Hum. Mol. Genet.* 12, 907–914 (2003).
 101. Bertoni, C., Lau, C. & Rando, T. A. Restoration of dystrophin expression in mdx muscle cells by chimeraplast-mediated exon skipping. *Hum. Mol. Genet.* 12, 1087–1099 (2003).
 102. Bremmer-Bout, M. *et al.* Targeted exon skipping in transgenic hDMD mice: A model for direct preclinical screening of human-specific antisense oligonucleotides. *Mol. Ther.* 10, 232–240 (2004).
 103. Fletcher, S. *et al.* Morpholino oligomer-mediated exon skipping averts the onset of dystrophic pathology in the mdx mouse. *Mol. Ther.* 15, 1587–1592 (2007).
 104. Mann, C. J. *et al.* Antisense-induced exon skipping and synthesis of dystrophin in the mdx mouse. *Proc. Natl. Acad. Sci. U. S. A.* 98, 42–7 (2001).
 105. McClorey, G. *et al.* Induced dystrophin exon skipping in human muscle explants. *Neuromuscul. Disord.* 16, 583–590 (2006).

References

106. McClorey, G., Moulton, H. M., Iversen, P. L., Fletcher, S. & Wilton, S. D. Antisense oligonucleotide-induced exon skipping restores dystrophin expression in vitro in a canine model of DMD. *Gene Ther.* 13, 1373–1381 (2006).
107. Wilton, S. D. *et al.* Antisense oligonucleotide-induced exon skipping across the human dystrophin gene transcript. *Mol. Ther.* 15, 1288–96 (2007).
108. Goemans, N. M. *et al.* Systemic administration of PRO051 in Duchenne's muscular dystrophy. *N. Engl. J. Med.* 364, 1513–1522 (2011).
109. Cirak, S. *et al.* Restoration of the dystrophin-associated glycoprotein complex after exon skipping therapy in Duchenne muscular dystrophy. *Mol. Ther.* 20, 462–7 (2012).
110. Kinali, M. *et al.* Local restoration of dystrophin expression with the morpholino oligomer AVI-4658 in Duchenne muscular dystrophy: a single-blind, placebo-controlled, dose-escalation, proof-of-concept study. *Lancet Neurol.* 8, 918–928 (2009).
111. Cirak, S. *et al.* Exon skipping and dystrophin restoration in patients with Duchenne muscular dystrophy after systemic phosphorodiamidate morpholino oligomer treatment: An open-label, phase 2, dose-escalation study. *Lancet* 378, 595–605 (2011).
112. Fermini, B. & Fossa, A. a. The impact of drug-induced QT interval prolongation on drug discovery and development. *Nat. Rev. Drug Discov.* 2, 439–447 (2003).
113. McNeish, J. Embryonic stem cells in drug discovery. *Nat. Rev. Drug Discov.* 3, 70–80 (2004).
114. Redfern, W. S. *et al.* Relationships between preclinical cardiac electrophysiology, clinical QT interval prolongation and torsade de pointes for a broad range of drugs: Evidence for a provisional safety margin in drug development. *Cardiovascular Research.* 58, 32–45 (2003).
115. Hoffmann, P. & Warner, B. Are hERG channel inhibition and QT interval prolongation all there is in drug-induced torsadogenesis? A review of emerging trends. *Journal of Pharmacological and Toxicological Methods.* 53, 87–105 (2006).
116. Lacerda, A. E. *et al.* Alfuzosin delays cardiac repolarization by a novel mechanism. *J. Pharmacol. Exp. Ther.* 324, 427–433 (2008).
117. Rodríguez-Menchaca, A. a *et al.* The molecular basis of chloroquine block of the inward rectifier Kir2.1 channel. *Proc. Natl. Acad. Sci. U. S. A.* 105, 1364–1368 (2008).
118. Zwi, L. *et al.* Cardiomyocyte differentiation of human induced pluripotent stem cells. *Circulation.* 120, 1513–1523 (2009).
119. Otsuji, T. G. *et al.* Progressive maturation in contracting cardiomyocytes derived from human embryonic stem cells: Qualitative effects on electrophysiological responses to drugs. *Stem Cell Res.* 4, 201–213 (2010).
120. Smalley, W. *et al.* Contraindicated use of cisapride: impact of food and drug administration regulatory action. *JAMA.* 284, 3036–3039 (2000).
121. Moretti, A. *et al.* Patient-Specific Induced Pluripotent Stem-Cell Models for Long-QT Syndrome. *N. Engl. J. Med.* 363, 1397–1409 (2010).
122. Lan, F. *et al.* Abnormal calcium handling properties underlie familial hypertrophic cardiomyopathy pathology in patient-specific induced pluripotent stem cells. *Cell Stem Cell* 12, 101–113 (2013).
123. Bers, D. M. Cardiac excitation-contraction coupling. *Nature.* 415, 198–205 (2002).
124. Berecki, G., Zegers, J. G., Wilders, R. & Van Ginneken, A. C. G. Cardiac channelopathies studied with the dynamic action potential-clamp technique. *Methods Mol. Biol.* 403, 233–250 (2007).
125. DiFrancesco, D. Pacemaker mechanisms in cardiac tissue. *Annu. Rev. Physiol.* 55, 455–472 (1993).
126. Shih, H. T. Anatomy of the action potential in the heart. *Tex. Heart Inst. J.* 21, 30–41 (1994).
127. Mummery, C. *et al.* Differentiation of human embryonic stem cells to cardiomyocytes: role of coculture with visceral endoderm-like cells. *Circulation.* 107, 2733–40 (2003).
128. Magyar, J. *et al.* Effects of endothelin-1 on calcium and potassium currents in undiseased human ventricular myocytes. *Pflugers Arch. Eur. J. Physiol.* 441, 144–149 (2000).
129. Ma, J. *et al.* High purity human-induced pluripotent stem cell-derived cardiomyocytes: electrophysiological properties of action potentials and ionic currents. *Am. J. Physiol. Heart Circ. Physiol.* 301, H2006–17 (2011).
130. Zhang, J. *et al.* Functional cardiomyocytes derived from human induced pluripotent stem cells. *Circ. Res.* 104, (2009).
131. Drouin, E., Lande, G. & Charpentier, F. Amiodarone reduces transmural heterogeneity of repolarization in the human heart. *J. Am. Coll. Cardiol.* 32, 1063–1067 (1998).

References

132. Amin, A. S., Tan, H. L. & Wilde, A. A. M. Cardiac ion channels in health and disease. *Hear. Rhythm* 7, 117–126 (2010).
133. Synnergren, J., Améen, C., Jansson, A. & Sartipy, P. Global transcriptional profiling reveals similarities and differences between human stem cell-derived cardiomyocyte clusters and heart tissue. *Physiol. Genomics*. 44, 245–58 (2012).
134. Cordeiro, J. M. *et al.* Identification and characterization of a transient outward K⁺ current in human induced pluripotent stem cell-derived cardiomyocytes. *J. Mol. Cell. Cardiol.* 60, 36–46 (2013).
135. Bkaily, G. *et al.* Angiotensin II-induced increase of T-type Ca²⁺ current and decrease of L-type Ca²⁺ current in heart cells. *Peptides*. 26, 1410–1417 (2005).
136. Ono, K. & Iijima, T. Cardiac T-type Ca²⁺ channels in the heart. *Journal of Molecular and Cellular Cardiology*. 48, 65–70 (2010).
137. Ivashchenko, C. Y. *et al.* Human-induced pluripotent stem cell-derived cardiomyocytes exhibit temporal changes in phenotype. *Am. J. Physiol. Heart Circ. Physiol.* 305, H913–22 (2013).
138. Sartiani, L. *et al.* Developmental changes in cardiomyocytes differentiated from human embryonic stem cells: a molecular and electrophysiological approach. *Stem Cells*. 25, 1136–44 (2007).
139. Honda, M., Kiyokawa, J., Tabo, M. & Inoue, T. Electrophysiological Characterization of Cardiomyocytes Derived From Human Induced Pluripotent Stem Cells. *J. Pharmacol. Sci.* 117, 149–159 (2011).
140. Barov, M. Advances in patch clamp technique: Towards higher quality and quantity. *General Physiology and Biophysics*. 31, 131–140 (2012).
141. Kodandaramaiah, S. B., Franzesi, G. T., Chow, B. Y., Boyden, E. S. & Forest, C. R. Automated whole-cell patch-clamp electrophysiology of neurons in vivo. *Nat. Methods*. 9, 585–7 (2012).
142. Dale, T. J., Townsend, C., Hollands, E. C. & Trezise, D. J. Population patch clamp electrophysiology: a breakthrough technology for ion channel screening. *Mol. Biosyst.* 3, 714–22 (2007).
143. Mathes, C. QPatch: the past, present and future of automated patch clamp. *Expert Opin. Ther. Targets*. 10, 319–327 (2006).
144. Zeng, H. *et al.* Improved throughput of PatchXpress hERG assay using intracellular potassium fluoride. *Assay Drug Dev. Technol.* 6, 235–41 (2008).
145. Stoelzle-Feix, S. State-of-the-art automated patch clamp: heat activation, action potentials, and high throughput in ion channel screening. *Methods Mol. Biol.* 1183, 65–80 (2014).
146. Polonchuk, L. Industrializing electrophysiology: HT automated patch clamp on SyncroPatch 96 using instant frozen cells. *Methods Mol. Biol.* 1183, 81–92 (2014).
147. Becker, N. *et al.* Minimized cell usage for stem cell-derived and primary cells on an automated patch clamp system. *J. Pharmacol. Toxicol. Methods*. 68, 82–87 (2013).
148. Matsa, E. *et al.* Drug evaluation in cardiomyocytes derived from human induced pluripotent stem cells carrying a long QT syndrome type 2 mutation. *Eur. Heart J.* 32, 952–962 (2011).
149. Burridge, P. W. *et al.* Chemically defined generation of human cardiomyocytes. *Nat. Methods*. 11, 855–60 (2014).
150. Salzberg, B. M., Grinvald, a, Cohen, L. B., Davila, H. V & Ross, W. N. Optical recording of neuronal activity in an invertebrate central nervous system: simultaneous monitoring of several neurons. *J. Neurophysiol.* 40, 1281–91 (1977).
151. Chang Liao, M.-L. *et al.* Sensing Cardiac Electrical Activity With a Cardiac Myocyte Targeted Optogenetic Voltage Indicator. *Circ. Res.* 117.306143– (2015).
152. Leyton-Mange, J. S. *et al.* Rapid cellular phenotyping of human pluripotent stem cell-derived cardiomyocytes using a genetically encoded fluorescent voltage sensor. *Stem Cell Reports*. 2, 163–170 (2014).
153. Vinkenborg, J. L., Koay, M. S. & Merx, M. Fluorescent imaging of transition metal homeostasis using genetically encoded sensors. *Current Opinion in Chemical Biology* .14, 231–237 (2010).
154. Lindenbarg, L. & Merx, M. Engineering Genetically Encoded FRET Sensors. *Sensors*. 14, 11691–11713 (2014).
155. Kim, H. N., Ren, W. X., Kim, J. S. & Yoon, J. Fluorescent and colorimetric sensors for detection of lead, cadmium, and mercury ions. *Chem. Soc. Rev.* 41, 3210 (2012).
156. Miesenböck, G., De Angelis, D. a & Rothman, J. E. Visualizing secretion and synaptic transmission with pH-sensitive green fluorescent proteins. *Nature*. 394, 192–5 (1998).
157. Østergaard, H., Henriksen, A., Hansen, F. G. & Winther, J. R. Shedding light on disulfide bond

- formation: Engineering a redox switch in green fluorescent protein. *EMBO J.* 20, 5853–5862 (2001).
158. Carlson, H. J. & Campbell, R. E. Circularly permuted red fluorescent proteins and calcium ion indicators based on mCherry. *Protein Eng. Des. Sel.* 26, 763–772 (2013).
 159. Tian, L. *et al.* Imaging neural activity in worms, flies and mice with improved GCaMP calcium indicators. *Nat. Methods.* 6, 875–881 (2009).
 160. Jin, L. *et al.* Single Action Potentials and Subthreshold Electrical Events Imaged in Neurons with a Fluorescent Protein Voltage Probe. *Neuron.* 75, 779–785 (2012).
 161. Cao, G. *et al.* Genetically targeted optical electrophysiology in intact neural circuits. *Cell.* 154, 904–913 (2013).
 162. Raimondo, J. V. *et al.* A genetically-encoded chloride and pH sensor for dissociating ion dynamics in the nervous system. *Front. Cell. Neurosci.* 7, 202 (2013).
 163. Bilan, D. S. *et al.* HyPer-3: A genetically encoded H₂O₂ probe with improved performance for ratiometric and fluorescence lifetime imaging. *ACS Chem. Biol.* 8, 535–542 (2013).
 164. Marvin, J. S. *et al.* An optimized fluorescent probe for visualizing glutamate neurotransmission. *Nat. Methods.* 10, 162–170 (2013).
 165. Berg, J., Hung, Y. P. & Yellen, G. A genetically encoded fluorescent reporter of ATP : ADP ratio. *Nat. Methods.* 6, 161–166 (2009).
 166. Tantama, M., Martínez-François, J. R., Mongeon, R. & Yellen, G. Imaging energy status in live cells with a fluorescent biosensor of the intracellular ATP-to-ADP ratio. *Nat. Commun.* 4, 2550 (2013).
 167. Hanson, G. T. *et al.* Investigating Mitochondrial Redox Potential with Redox-sensitive Green Fluorescent Protein Indicators. *J. Biol. Chem.* 279, 13044–13053 (2004).
 168. Zhao, Y. *et al.* An expanded palette of genetically encoded Ca²⁺(+) indicators. *Science.* 333, 1888–1891 (2011).
 169. Chen, T.-W. *et al.* Ultrasensitive fluorescent proteins for imaging neuronal activity. *Nature.* 499, 295–300 (2013).
 170. Lakowicz, J. R. *Principles of fluorescence spectroscopy. Principles of Fluorescence Spectroscopy* (2006).
 171. Haseloff, J. GFP variants for multispectral imaging of living cells. *Methods Cell Biol.* 58, 139–51. (1999).
 172. Lam, A. J. *et al.* Improving FRET dynamic range with bright green and red fluorescent proteins. *Nat. Methods.* 9, 1005–12 (2012).
 173. Miyawaki, a *et al.* Fluorescent indicators for Ca²⁺ based on green fluorescent proteins and calmodulin. *Nature.* 388, 882–887 (1997).
 174. Piljić, A., De Diego, I., Wilmanns, M. & Schultz, C. Rapid development of genetically encoded FRET reporters. *ACS Chem. Biol.* 6, 685–691 (2011).
 175. Juillerat, A. *et al.* Directed evolution of O⁶-alkylguanine-DNA alkyltransferase for efficient labeling of fusion proteins with small molecules in vivo. *Chem. Biol.* 10, 313–317 (2003).
 176. Griffin, B. a, Adams, S. R. & Tsien, R. Y. Specific covalent labeling of recombinant protein molecules inside live cells. *Science.* 281, 269–272 (1998).
 177. Brun, M. A., Tan, K. T., Nakata, E., Hinner, M. J. & Johnsson, K. Semisynthetic fluorescent sensor proteins based on self-labeling protein tags. *J. Am. Chem. Soc.* 131, 5873–5884 (2009).
 178. Griss, R. *et al.* Bioluminescent sensor proteins for point-of-care therapeutic drug monitoring. *Nat. Chem. Biol.* 10, 598–603 (2014).
 179. Hoffmann, C. *et al.* A FIAsh-based FRET approach to determine G protein-coupled receptor activation in living cells. *Nat. Methods.* 2, 171–176 (2005).
 180. Knöpfel, T., D’Ez-García, J. & Akemann, W. Optical probing of neuronal circuit dynamics: Genetically encoded versus classical fluorescent sensors. *Trends in Neurosciences.* 29, 160–166 (2006).
 181. Mutoh, H., Perron, A., Akemann, W., Iwamoto, Y. & Knöpfel, T. Optogenetic monitoring of membrane potentials. *Exp. Physiol.* 96, 13–8 (2011).
 182. Perron, A. *et al.* Second and third generation voltage-sensitive fluorescent proteins for monitoring membrane potential. *Front. Mol. Neurosci.* 2, 5 (2009).
 183. Siegel, M. S. & Isacoff, E. Y. A genetically encoded optical probe of membrane voltage. *Neuron.* 19, 735–741 (1997).

References

184. Ataka, K. & Pieribone, V. a. A genetically targetable fluorescent probe of channel gating with rapid kinetics. *Biophys. J.* 82, 509–16 (2002).
185. Sakai, R., Repunte-Canonigo, V., Raj, C. D. & Knöpfel, T. Design and characterization of a DNA-encoded, voltage-sensitive fluorescent protein. *Eur. J. Neurosci.* 13, 2314–2318 (2001).
186. Akemann, W., Mutoh, H., Perron, A., Rossier, J. & Knöpfel, T. Imaging brain electric signals with genetically targeted voltage-sensitive fluorescent proteins. *Nat. Methods.* 7, 643–649 (2010).
187. Tsutsui, H., Karasawa, S., Okamura, Y. & Miyawaki, A. Improving membrane voltage measurements using FRET with new fluorescent proteins. *Nat. Methods.* 5, 683–5 (2008).
188. Lundby, A., Mutoh, H., Dimitrov, D., Akemann, W. & Knöpfel, T. Engineering of a genetically encodable fluorescent voltage sensor exploiting fast Ci-VSP voltage-sensing movements. *PLoS One.* 3, (2008).
189. Perron, A., Mutoh, H., Launey, T. & Knöpfel, T. Red-Shifted Voltage-Sensitive Fluorescent Proteins. *Chem. Biol.* 16, 1268–1277 (2009).
190. Gautam, S. G., Perron, A., Mutoh, H. & Knöpfel, T. Exploration of fluorescent protein voltage probes based on circularly permuted fluorescent proteins. *Front. Neuroeng.* 2, 14 (2009).
191. Akemann, W. *et al.* Imaging neural circuit dynamics with a voltage-sensitive fluorescent protein. *J. Neurophysiol.* 108, 2323–37 (2012).
192. Perron, A., Akemann, W., Mutoh, H. & Knöpfel, T. Genetically encoded probes for optical imaging of brain electrical activity. *Prog. Brain Res.* 196, 63–77 (2012).
193. Braun, T. & Gautel, M. Transcriptional mechanisms regulating skeletal muscle differentiation, growth and homeostasis. *Nat. Rev. Mol. Cell Biol.* 12, 349–361 (2011).
194. Gramlich, M. *et al.* Stress-induced dilated cardiomyopathy in a knock-in mouse mimicking human titin-based disease. *J. Mol. Cell. Cardiol.* 47, 352–358 (2009).
195. Goyenvalle, A., Babbs, A., van Ommen, G.-J. B., Garcia, L. & Davies, K. E. Enhanced exon-skipping induced by U7 snRNA carrying a splicing silencer sequence: Promising tool for DMD therapy. *Mol. Ther.* 17, 1234–40 (2009).
196. Huber, I. *et al.* Identification and selection of cardiomyocytes during human embryonic stem cell differentiation. *Faseb J.* 21, 2551–2563 (2007).
197. Kulak, N. A., Pichler, G., Paron, I., Nagaraj, N. & Mann, M. Minimal, encapsulated proteomic-sample processing applied to copy-number estimation in eukaryotic cells. *Nat. Methods.* 11, 319–24 (2014).
198. Michalski, a. *et al.* Ultra High Resolution Linear Ion Trap Orbitrap Mass Spectrometer (Orbitrap Elite) Facilitates Top Down LC MS/MS and Versatile Peptide Fragmentation Modes. *Mol. Cell. Proteomics.* 11, O111.013698–O111.013698 (2012).
199. Cox, J. & Mann, M. MaxQuant enables high peptide identification rates, individualized p.p.b.-range mass accuracies and proteome-wide protein quantification. *Nat. Biotechnol.* 26, 1367–72 (2008).
200. Cox, J. *et al.* Andromeda: A peptide search engine integrated into the MaxQuant environment. *J. Proteome Res.* 10, 1794–1805 (2011).
201. Schaab, C., Geiger, T., Stoehr, G., Cox, J. & Mann, M. Analysis of High Accuracy, Quantitative Proteomics Data in the MaxQB Database. *Mol. Cell. Proteomics* 11, M111.014068–M111.014068 (2012).
202. Nishino, K. *et al.* DNA methylation dynamics in human induced pluripotent stem cells over time. *PLoS Genet.* 7, (2011).
203. Chamberlain, S. J. *et al.* Induced pluripotent stem cell models of the genomic imprinting disorders Angelman and Prader – Willi syndromes. *Pnas.* 107, 17668–17673 (2010).
204. Calvanese, V. *et al.* Cancer genes hypermethylated in human embryonic stem cells. *PLoS One.* 3, e3294 (2008).
205. Gramlich, M. *et al.* Antisense-mediated exon skipping: a therapeutic strategy for titin-based dilated cardiomyopathy. *EMBO Mol. Med.* 7, 562–576 (2015).
206. Atherton, B. T., Meyer, D. M. & Simpson, D. G. Assembly and remodelling of myofibrils and intercalated discs in cultured neonatal rat heart cells. *J. Cell Sci.* 86, 233–48 (1986).
207. Sung, L.-Y. *et al.* Efficient gene delivery into cell lines and stem cells using baculovirus. *Nat. Protoc.* 9, 1882–99 (2014).
208. Sparrow, J. C. & Schöck, F. The initial steps of myofibril assembly: integrins pave the way. *Nat. Rev. Mol. Cell Biol.* 10, 293–298 (2009).
209. Dabiri, G. A., Turnacioglu, K. K., Sanger, J. M. & Sanger, J. W. Myofibrillogenesis visualized in

- living embryonic cardiomyocytes. *Proc. Natl. Acad. Sci. U. S. A.* 94, 9493–8 (1997).
210. Ahuja, P., Perriard, E., Perriard, J.-C. & Ehler, E. Sequential myofibrillar breakdown accompanies mitotic division of mammalian cardiomyocytes. *J. Cell Sci.* 117, 3295–3306 (2004).
 211. Krüger, M. & Linke, W. A. Titin-based mechanical signalling in normal and failing myocardium. *Journal of Molecular and Cellular Cardiology.* 46, 490–498 (2009).
 212. Linke, W. a & Krüger, M. The giant protein titin as an integrator of myocyte signaling pathways. *Physiology (Bethesda).* 25, 186–198 (2010).
 213. Linke, W. A. & Hamdani, N. Gigantic business: Titin properties and function through thick and thin. *Circulation Research.* 114, 1052–1068 (2014).
 214. Miano, J. M. *et al.* Restricted inactivation of serum response factor to the cardiovascular system. *Proc. Natl. Acad. Sci. U. S. A.* 101, 17132–7 (2004).
 215. Miano, J. M., Long, X. & Fujiwara, K. Serum response factor: master regulator of the actin cytoskeleton and contractile apparatus. *Am. J. Physiol. Cell Physiol.* 292, C70–C81 (2007).
 216. Gramlich, M. *et al.* Antisense-mediated exon skipping: a therapeutic strategy for titin-based dilated cardiomyopathy. *EMBO Mol. Med.* e201505047 (2015).
 217. Stefanovic, B., Wittop Koning, T. H. & Schümperli, D. A synthetic histone pre-mRNA-U7 small nuclear RNA chimera undergoing cis cleavage in the cytoplasm of *Xenopus* oocytes. *Nucleic Acids Res.* 23, 3152–60 (1995).
 218. Qin, J. Y. *et al.* Systematic Comparison of Constitutive Promoters and the Doxycycline-Inducible Promoter. *PLoS One* 5, e10611 (2010).
 219. Chen, Z. *et al.* Subtype-specific promoter-driven action potential imaging for precise disease modelling and drug testing in hiPSC-derived cardiomyocytes. *Eur. Heart J.* 13, 713–726 (2016).
 220. Bizy, A. *et al.* Myosin light chain 2-based selection of human iPSC-derived early ventricular cardiac myocytes. *Stem Cell Res.* 11, 1335–1347 (2013).
 221. De Sousa Lopes, S. M. C. *et al.* Patterning the heart, a template for human cardiomyocyte development. *Dev. Dyn.* 235, 1994–2002 (2006).
 222. Moretti, A., Laugwitz, K.-L., Dorn, T., Sinnecker, D. & Mummery, C. Pluripotent stem cell models of human heart disease. *Cold Spring Harb. Perspect. Med.* 3, a014027 (2013).
 223. Bosman, A. *et al.* Molecular and Functional Evidence of Hyperpolarization-Activated Cyclic Nucleotide-Gated Channel 4 (HCN4) and Caveolin-3 Interaction During Cardiomyocyte Differentiation from Human Embryonic Stem Cells. *Stem Cells Dev.* 1717-1727, (2013).
 224. Minamisawa, S. *et al.* Atrial chamber-specific expression of sarcolipin is regulated during development and hypertrophic remodeling. *J. Biol. Chem.* 278, 9570–9575 (2003).
 225. Josowitz, R. *et al.* Identification and purification of human induced pluripotent stem cell-derived atrial-like cardiomyocytes based on sarcolipin expression. *PLoS One.* 9, e101316 (2014).
 226. Blaschke, R. J. *et al.* Targeted mutation reveals essential functions of the homeodomain transcription factor *Shox2* in sinoatrial and pacemaking development. *Circulation.* 115, 1830–1838 (2007).
 227. Espinoza-Lewis, R. A. *et al.* *Shox2* is essential for the differentiation of cardiac pacemaker cells by repressing *Nkx2-5*. *Dev. Biol.* 327, 376–85 (2009).
 228. Hashem, S. I. & Claycomb, W. C. Genetic isolation of stem cell-derived pacemaker-nodal cardiac myocytes. *Mol. Cell. Biochem.* 383, 161–171 (2013).
 229. Gilchrist, K. H., Lewis, G. F., Gay, E. A., Sellgren, K. L. & Grego, S. High-throughput cardiac safety evaluation and multi-parameter arrhythmia profiling of cardiomyocytes using microelectrode arrays. *Toxicol. Appl. Pharmacol.* 288, 249–257 (2015).
 230. Speranza, L., Franceschelli, S. & Riccioni, G. The Biological effects of ivabradine in cardiovascular disease. *Molecules.* 17, 4924–4935 (2012).
 231. Freiburg, a *et al.* Series of exon-skipping events in the elastic spring region of titin as the structural basis for myofibrillar elastic diversity. *Circ. Res.* 86, 1114–1121 (2000).
 232. Betts, C. *et al.* Pip6-PMO, A New Generation of Peptide-oligonucleotide Conjugates With Improved Cardiac Exon Skipping Activity for DMD Treatment. *Mol. Ther. Nucleic Acids.* 1, e38 (2012).
 233. Kobayashi, K., Izawa, T., Kuwamura, M. & Yamate, J. Dysferlin and animal models for dysferlinopathy. *J. Toxicol. Pathol.* 25, 135–47 (2012).
 234. van Deutekom, J. C. *et al.* Local dystrophin restoration with antisense oligonucleotide PRO051. *N.*

- Engl. J. Med.* 357, 2677–2686 (2007).
235. Yu, J. *et al.* Induced pluripotent stem cell lines derived from human somatic cells. *Science*. 318, 1917–20 (2007).
 236. Puri, M. C. & Nagy, A. Concise review: Embryonic stem cells versus induced pluripotent stem cells: The game is on. *Stem Cells*. 30, 10–14 (2012).
 237. Moss, A. J. *et al.* Clinical aspects of type-1 long-QT syndrome by location, coding type, and biophysical function of mutations involving the KCNQ1 gene. *Circulation*. 115, 2481–2489 (2007).
 238. Brunner, M. *et al.* Mechanisms of cardiac arrhythmias and sudden death in transgenic rabbits with long QT syndrome. *J. Clin. Invest.* 118, 2246–59 (2008).
 239. Goldstein, D. B. Common genetic variation and human traits. *N. Engl. J. Med.* 360, 1696–8 (2009).
 240. McKernan, K. J. *et al.* Sequence and structural variation in a human genome uncovered by short-read, massively parallel ligation sequencing using two-base encoding. *Genome Res.* 19, 1527–1541 (2009).
 241. de Boer, T. P. *et al.* Human cardiomyocyte progenitor cell-derived cardiomyocytes display a matured electrical phenotype. *J. Mol. Cell. Cardiol.* 48, 254–260 (2010).
 242. Hoekstra, M., Mummery, C. L., Wilde, A. A. M., Bezzina, C. R. & Verkerk, A. O. Induced pluripotent stem cell derived cardiomyocytes as models for cardiac arrhythmias. *Frontiers in Physiology*. 3 AUG, (2012).
 243. Reinhardt, P. *et al.* Genetic correction of a *lrrk2* mutation in human iPSCs links parkinsonian neurodegeneration to ERK-dependent changes in gene expression. *Cell Stem Cell*. 12, 354–367 (2013).
 244. Montgomery, S. B. *et al.* Transcriptome genetics using second generation sequencing in a Caucasian population. *Nature*. 464, 773–7 (2010).
 245. Boulting, G. L. *et al.* A functionally characterized test set of human induced pluripotent stem cells. *Nat Biotechnol.* 29, 279–286 (2011).
 246. Vinge, L. E., Raake, P. W. & Koch, W. J. Gene therapy in heart failure. *Circulation Research*. 102, 1458–1470 (2008).
 247. Greenberg, B. *et al.* Design of a Phase 2b Trial of Intracoronary Administration of AAV1/SERCA2a in Patients With Advanced Heart Failure. *JACC Hear. Fail.* 2, 84–92 (2014).
 248. Liang, P. *et al.* Drug screening using a library of human induced pluripotent stem cell-derived cardiomyocytes reveals disease-specific patterns of cardiotoxicity. *Circulation*. 127, 1677–91 (2013).
 249. Wang, Y. *et al.* Genome editing of isogenic human induced pluripotent stem cells recapitulates long QT phenotype for drug testing. *J. Am. Coll. Cardiol.* 64, 451–459 (2014).
 250. Kaestner, L. *et al.* Genetically encoded voltage indicators in circulation research. *International Journal of Molecular Sciences*. 16, 21626–21642 (2015).
 251. Dunlop, J., Bowlby, M., Peri, R., Vasilyev, D. & Arias, R. High-throughput electrophysiology: an emerging paradigm for ion-channel screening and physiology. *Nat. Rev. Drug Discov.* 7, 358–368 (2008).
 252. Tian, Q. *et al.* Optical action potential screening on adult ventricular myocytes as an alternative QT-screen. *Cell. Physiol. Biochem.* 27, 281–290 (2011).
 253. Shinnawi, R. *et al.* Monitoring human-induced pluripotent stem cell-derived cardiomyocytes with genetically encoded calcium and voltage fluorescent reporters. *Stem Cell Reports*. 5, 582–596 (2015).
 254. Denning, C. *et al.* Cardiomyocytes from human pluripotent stem cells: From laboratory curiosity to industrial biomedical platform. *Biochimica et Biophysica Acta - Molecular Cell Research*. (2015)

Articles

- 1 **Antisense-mediated exon skipping: a therapeutic strategy for titin-based dilated cardiomyopathy. *EMBO Mol Med.* 2015 Mar 9; 7(5):562-76.**
- 2 **Subtype-specific promoter-driven action potential imaging for precise disease modeling and drug testing in hiPSC-derived cardiomyocytes. *European Heart Journal.* *in press.***

Acknowledgements

I would like to thank three most important groups of people: my dissertation committee, my external collaborators, my wonderful lab-mates, and my family and friends, without whom this dissertation would not have been possible.

Foremost, I would like to thank the members of my dissertation committee including: Prof. Dr. med. Karl-Ludwig Laugwitz, Prof. Dr. med. Adnan Kastrati, Prof. Dr. rer. nat. Alessandra Moretti and Dr. med Daniel Sinnecker, not only for their time and extreme patience, but for their intellectual contributions to my development as a scientist. I want to thank my advisors Prof. Laugwitz and Prof. Moretti for providing the precious opportunity to do my PhD training at the Technical University of Munich as an international student from China. As the group leader, Karl advised me to aim at performing unique experiments addressing urgent and significant questions in the field and to sell my work as a businessman does, which, I think, will benefit all through my career. His interest in biomedical research has been a strong and positive influence on my motivation in persistence in the challenging research work. I am also indebted to Alessandra, who is the most intelligent woman I know well. I was amazed by how fast she can react for troubleshooting and how thoughtful she is to help me to plan those dedicated experiments such as the single cell analysis combining electrophysiological analysis and molecular investigation. Without her input and high requirement for my dissertation work, I would not have finished it so fast and the submitted report would not be so well written. I feel grateful to Prof. Kastrati who is an extraordinary cardiologist. In spite of his tight schedule, he was always patient to listen to my research reports, give suggestions for my experiments and share his knowledge. He also always encouraged me to peruse the academic career persistently. To Prof. Peter Lipp, who provided the fantastic equipment to optimize my VSFP-based optical imaging, I would like to thank his sharing of the lab facilities and expertise in cardiac electrophysiology.

Most of all, I would like to thank my dissertation advisor, Daniel Sinnecker, a talented teacher, an excellent medical doctor and passionate scientist. For a young principal investigator who had never before taken on a graduate student, Daniel seemed to be wise beyond his experience. The majority of work of my dissertation regarding the subtype-specific optical AP recording was initiated based on his insightful ideas and profound knowledge of molecular cardiology and cardiac regenerative medicine as a young medical doctor. He spared his limited time off clinical work on to our research project and efficiently guaranteed it go straightforward without so many

Acknowledgements

detours. Daniel was thoughtful to educate me as a well-qualified junior scientist. He was very supportive to my independence in developing ideas and troubleshooting with inspiring guiding, to training my presenting as well as writing skills, and to my application for a postdoc position. At several points during my dissertation work, Daniel put my interests as a student ahead of his own - as a young faculty member, his ultimate concern for the welfare of his students is noteworthy. I also thank Daniel for appreciating my own ideas and research directions, being confident in my abilities and patiently encouraging me to improve in my weaker areas. Graduate school can be a difficult, draining experience. I am proud to say my experience in the Laugwitz lab was intellectually exciting and fun, and has energized me to continue in academic research. I sincerely hope I continue to have opportunities to interact with Daniel for the rest of my research career.

To Dr. Luna Simona Pane, I thank for being my first supervisor when we worked together on the titin project. She is an excellent teacher in guiding me to learn not only the biological techniques including stem cell culture, immunostaining, quantitative PCR, etc., but also how to plan and perform experiments properly. Aside work, she is also one of my best friends and teachers of my life. To Dr. Tatiana Dorn as my third supervisor, I feel grateful for her help with all the gene cloning strategy and thoughtful suggestions in my experiments. She is also caring for me like an older sister. To Dr. Qinghai Tian from Prof. Lipp's lab, I thank for his help in guiding me analyzing massive data with MetaLab and technical troubleshooting. My experience working with Wenying at Prof. Lipp's lab was extremely positive and fun. She is a very hard working and intelligent junior scientist and one of my best friends. I would like to thank our technical assistant, Christina Scherb who helped to do the lentiviral vector cloning. To my supervised MD student Christine Maria Schneider, I want to thank for her trust in me to be her supervisor and give me the chance to learn how to teach. I am glad to have a friend and excellent student as her.

To my lab-mates, Svenja Laue, Ilaria My, Elvira Parrotta, Lisa Dreizehnter, Jessica Haas and Diana Grewe, thanks for the fun and support. My experience in the lab was greatly enhanced as it filled out by all of them. To Svenja and Ilaria, many thanks for help at the bench and great company. Of all the people I have worked with in the "wet-lab" environment, I will easily miss hanging out with you two the most.

Finally, but not least, I want to thank my family for the constant support through the ups and downs during the PhD study. It has been bumpy at times, but your confidence in me has enhanced my ability to get through it all in the end.

EIGENSTÄNDIGKEITSERKLÄRUNG

Hiermit erkläre ich, Zhifen Chen, dass die vorliegende Dissertation zum Thema: '*human iPSC-derived cardiomyocytes as platforms for cardiac disease modeling, therapeutic discovery and safety pharmacology*' selbstständig verfasst wurde und keine anderen als die angegebenen Quellen und Hilfsmittel verwendet wurden.

München, den 27. 09. 2016

Zhifen Chen